DEVELOPMENT OF CATHODE MATERIALS FOR LI-ION BATTERIES BY SPUTTER DEPOSITION

A THESIS SUBMITTED TO
THE GRADUATE SCHOOL OF NATURAL AND APPLIED SCIENCES
OF
MIDDLE EAST TECHNICAL UNIVERSITY

BY

ERDEM ERKİN ERDOĞAN

IN PARTIAL FULFILLMENT OF THE REQUIREMENTS
FOR
THE DEGREE OF MASTER OF SCIENCE
IN
METALLURGICAL AND MATERIALS ENGINEERING

FEBRUARY 2022

Approval of the thesis:

DEVELOPMENT OF CATHODE MATERIALS FOR LI-ION BATTERIES BY SPUTTER DEPOSITION

submitted by **ERDEM ERKİN ERDOĞAN** in partial fulfillment of the requirements for the degree of **Master of Science** i**n Metallurgical and Materials Engineering, Middle East Technical University** by,

Prof. Dr. Halil Kalıpçılar
Dean, Graduate School of **Natural and Applied Sciences** _____

Prof. Dr. Cemil Hakan Gür
Head of the Department, **Metallurgical and Materials Eng.** _____

Prof. Dr. M. Kadri Aydınol
Supervisor, **Metallurgical and Materials Eng., METU** _____

Examining Committee Members:

Prof. Dr. Tayfur Öztürk
Metallurgical and Materials Eng., METU _____

Prof. Dr. M. Kadri Aydınol
Metallurgical and Materials Eng., METU _____

Prof. Dr. Şaban Patat
Chemical Eng., Erciyes Uni. _____

Assist. Prof. Dr. Çiğdem Toparlı
Metallurgical and Materials Eng., METU _____

Assist. Prof. Dr. Berke Pişkin
Metallurgical and Materials Eng., Muğla Sıtkı Koçman Uni. _____

Date: 10.02.2022

I hereby declare that all information in this document has been obtained and presented in accordance with academic rules and ethical conduct. I also declare that, as required by these rules and conduct, I have fully cited and referenced all material and results that are not original to this work.

Name Last name : Erdem Erkin, Erdoğan

Signature :

ABSTRACT

DEVELOPMENT OF CATHODE MATERIALS FOR LI-ION BATTERIES BY SPUTTER DEPOSITION

Erdoğan, Erdem Erkin
Master of Science, Metallurgical and Materials Engineering
Supervisor : Prof. Dr. M. Kadri Aydınol

February 2022, 118 pages

The electrochemical performance of Li-ion batteries depends mostly on the cathode material. Cobalt has a huge impact on electrochemical properties and is widely used in cathode materials, but due to its toxicity and cost, recent research is focused on reducing the amount of cobalt in cathode materials. In this study, cathode active materials are produced by magnetron sputtering to obtain the optimum amount of cobalt while optimizing the electrochemical properties. Pechini sol-gel method is used to produce powders which are then used to produce sputtering targets by cold pressing and sintering. Both targets' and deposited electrodes' structural and morphological characterization were done by scanning electron microscopy (SEM), X-ray diffraction (XRD), and energy dispersive spectroscopy (EDS). The resultant compounds are used to produce battery cathodes via magnetron sputtering. Electrochemical characterization was done by galvanostatic charge-discharge tests and cyclic voltammetry (CV) to focus on discharge capacity and discharge energy of the cathode materials.

Keywords: Li-ion Battery, Cathode, Magnetron Sputter Deposition, Combinatorial

ÖZ

Lİ-İYON PİLLER İÇİN SIÇRATMA-BİRİKTİRME YÖNTEMİ İLE KATOT MALZEMELERİNİN GELİŞTİRİLMESİ

Erdoğan, Erdem Erkin
Yüksek Lisans, Metalurji ve Malzeme Mühendisliği
Tez Yöneticisi: Prof. Dr. M. Kadri Aydınol

Şubat 2022, 118 sayfa

Li-ion pillerin elektrokimyasal performansı ağırlıklı olarak katot malzemesine bağlıdır. Kobalt elementi, elektrokimyasal özellikler üzerinde büyük bir etkiye sahiptir ve katot malzemelerinde yaygın olarak kullanılmaktadır. Ancak toksisitesi ve maliyeti nedeniyle, son araştırmalar katot malzemelerindeki kobalt miktarını azaltmaya odaklanmıştır. Bu çalışmada, Pechini sol-jel yöntemi ile toz üretimi tamamlanmış, daha sonra soğuk presleme ve sinterleme işlemleri ile sıçratma üreteçleri üretilmiştir. Elektrokimyasal özellikleri optimize edilmiş ve kobalt miktarını azaltılmış katotlar elde etmek için magnetron sıçratma yöntemi ile katot üretimi tamamlanmıştır. Tozların, üreteçlerin ve magnetron sıçratma yöntemi ile üretilen elektrotların yapısal ve morfolojik karakterizasyonu, taramalı elektron mikroskobu (SEM), X-ışını kırınımı difraktografisi (XRD) ve enerji dağılımlı spektroskopi (EDS) ile yapılmıştır. Elektrokimyasal karakterizasyon, katot malzemelerinin deşarj kapasitesi ve deşarj enerjisine odaklanmak için galvanostatik şarj-deşarj testleri ve döngüsel voltametri (CV) ile yapılmıştır.

Anahtar Kelimeler: Li-iyon Pil, Katot, Magnetron Sputter, Kombinatoryal

To My Family

ACKNOWLEDGMENTS

The author wishes to express his gratitude to his supervisor Prof. Dr. M. Kadri Aydınol, for his supervision, advice, criticism, and insight throughout the research.

The author also expresses his gratitude to Prof. Dr. Tayfur Öztürk for his guidance, consultation, and vision throughout the research.

The author would also like to thank his lab mates and friends at the Department of Metallurgical and Materials Engineering, METU Cansu Savaş Uygur and Kadir Özgün Köse, for their support, sharing their knowledge, sharing their experience and for the insightful conversations between the experiments that will be remembered.

Furthermore, the author would like to thank Serkan Yılmaz for SEM user training and Nilüfer Özel for her supports of XRD analysis. Author also expresses his thanks to N. Özgür Darıcıoğlu and Yiğit Akbaş for their support during sputter experiments.

This work is partially funded by the Scientific and Technological Research Council of Turkey under grant number TUBİTAK 118M076.

Finally, the author would like to express his sincere thanks to his parents, Suna and Sekvan, and his brother Erşan for their endless love, patience, support, and guidance throughout his life.

TABLE OF CONTENTS

LIST OF TABLES

TABLES

LIST OF FIGURES

FIGURES

LIST OF ABBREVIATIONS

EDS	Energy Dispersive Spectroscopy
ICP-MS	Inductively Coupled Plasma-Mass Spectrometry
ICP-OES	Inductively Coupled Plasma-Optic Emission Spectrometry
LCO	Lithium Cobalt Oxide
LNO	Lithium Nickel Oxide
LMO	Lithium Manganese Oxide
NMC	Lithium Nickel Manganese Cobalt Oxide
NMP	N-methyl-2-pyrrolidone
PTFE	Polytetrafloroetilen
PVA	Polyvinyl Alcohol
PVD	Physical Vapor Deposition
SEM	Scanning Electron Microscopy
XRD	X-Ray Diffraction

CHAPTER 1

INTRODUCTION

1.1 Li-ion Batteries

Electrochemical conversion devices are standard in our daily lives, according to Winter and Brodd [1]. According to Armand [2], Li-ion batteries are the main components of today's mobile society, which uses portable telecommunication and computing equipment.

Li-ion batteries were first introduced as a rocking chair battery in the 1970s-1980s. This concept was improved by the contributions of researchers in this field. Then, Sony Corporation commercialized the $C/LiCoO_2$ rocking chair-cell in 1991 [3]. Since the commercialization, Li-ion batteries have become a topic that has attracted many scientists to work on them.

According to Winter and Brodd [1], Li-ion batteries are lighter in weight, have a higher energy density, do not have a memory effect, and have a low self-discharge rate lower than any other type of battery. These specifications make Li-ion batteries noticeable among different chemistries.

After the birth of Li-ion batteries, its application field is widened due to the emerging market of mobile applications such as mobile phones, personal computers, tablets, and the automotive industry's ongoing change from internal combustion engines to hybrid and electric vehicles.

The global lithium availability supports these increased application fields of Li-ion batteries. According to Islam and Fisher [4], the upper limit for lithium demand is significantly lower than the estimated lithium resource. Therefore, the availability of lithium is not an issue.

Over the years of the studies, the effects of elements on Li-ion batteries' components were studied to improve their structural and electrochemical performance. Today, cathodes with Mn, Co, and Ni are considered one of the most promising and most used stoichiometries. They are used in applications such as electric vehicles in which many brands use NMC cathodes, according to Li et al. [5].

1.2 Aim of This Study

This study has started to find the alloying groups for the cathode of Li-ion batteries with high Ni content and high stability.

Although some studies had opened the way before this work, the magnetron sputter deposition technique was used in this study. This technique led a path for a combinatorial approach via depositing many different cathodes at the same time to produce various materials in one experiment.

This unique opportunity, which has been made possible by the sputter deposition technique, was enabled to determine the electrochemical characterization differences of the cathode materials due to the stoichiometric differences.

CHAPTER 2

LITERATURE SURVEY

2.1 Li-ion Cathode Materials

Researchers have been working on anode and cathode materials to improve the critical properties, which are life cycle and energy density [6]. The main challenge ahead of the researchers is improving the discharge capacity of the commercial cathode materials [7]. Morphology and the structure of the electrode materials affect these parameters [8].

Nitta et al. [9] defined Li-ion cathode materials in intercalation cathode materials and conversion cathode materials. Intercalation cathodes are described in two types: transition metal oxides and polyanion metal oxides.

According to Islam and Fisher, transition metal oxides may be divided into five groups [4]. These groups are layered spinel, olivine, b_{II}-Li_2FeSiO_4 and tavorite. These structures may be seen in the following figure.

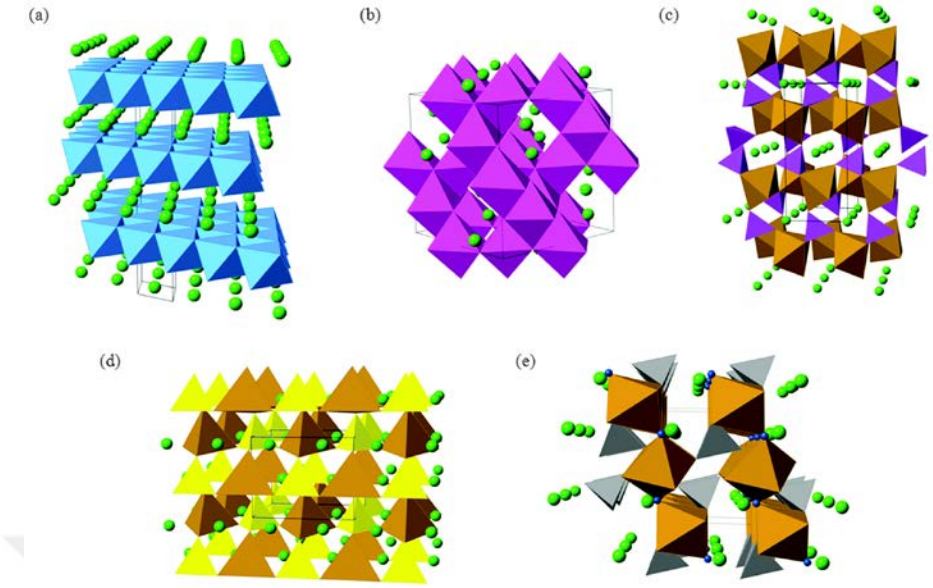

Figure 2.1 Crystal structures of cathode materials. a) layered $LiCoO_2$ b) spinel $LiMnO_4$ c) olivine $LiFePO_4$ d) β_{II}-$LiFeSiO_4$ e) tavorite $LiFeSO_4F$ [4]

According to Manthiram [10], cathode materials may be divided into three groups which are layered as in the study of Mizutshima et al. [11], spinel as in the study of Thackeray et al. [12], and polyanion groups as in the study of Manthiram and Goodenough [13]. These 3 three groups, which are talked about in Manthiram's work [10], are in parallel with the outcome of Islam and Fisher [4].

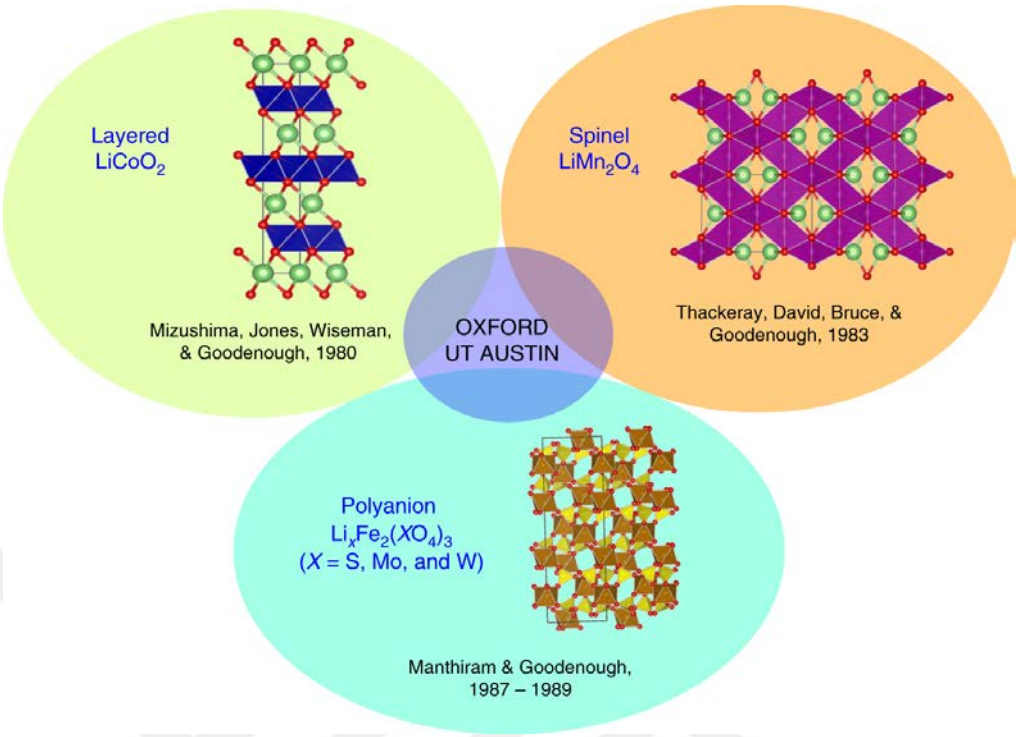

Figure 2.2 Positive-electrode crystal structures according to Manthiram [10]

Typical materials which have layered structures are $LiCoO_2$ (LCO), $LiNiO_2$ (LNO), $Li(Ni_{1/3}Mn_{1/3}Co_{1/3})O_2$ (NMC). The spinel structure's most common example is $LiMnO_2$ (LMO).

Since the materials used in this study are layered oxides and spinel oxides, the focus will be on these two groups.

Layered oxides have a general formula of $LiMO_2$, in which M stands for Mn, Co, or Ni; this is a distorted rock-salt (α-$NaFeO_2$ type) according to Kraytsberg an Ein-Eli [14]. The structure may be seen below.

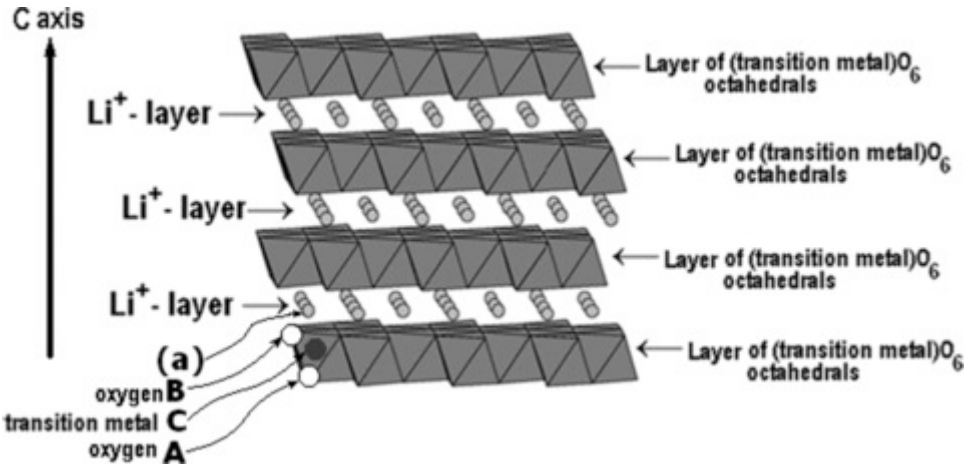

Figure 2.3 Schematic representation of $LiMO_2$ structure (M=Ni, Mn or Co) [14]

The first commercialized, widely used cathode layered cathode material is $LiCoO_2$ (LCO) due to its fair electric conductivity and Li^+ mobility, according to Mizushima et al. [11]. LCO has a high theoretical capacity of ~280 $mAhg^{-1}$, high discharge voltage and good cyclic stability [15], [16]. However, according to Jun et al. [17], capacity fades when LCO is cycled up to 4.2V. Therefore, it is not possible to reach its theoretical capacity. Also, the degradation of LCO due to stacking faults and pitting corrosion, according to Yano et al. [18], causes decreased capacity. LCO also has low thermal stability among commercial cathode materials, which leads to thermal runaway reaction when exothermic oxygen release occurs when a lithium metal oxide cathode is heated [19]. LCO has high structural stability due to the presence of Co^{+2} ions. Aurbach et al. [20] reported the presence of Co^{+2} ions in the LCO at high temperatures.

$LiNiO_2$ (LNO) which Dyer promoted in 1954 [21], has the same crystal structure and a similar theoretical capacity compared to LCO. Valikangas et al. [22] optimized calcination temperature and achieved 231.7 $mAhg^{-1}$ initial discharge capacity and 135 $mAhg^{-1}$ retaining capacity after 400 cycles. Replacing the Co with Ni reduces cost and toxicity. However, it brings challenges resulting from structural instability. Rougier et al. [23] found out that the Ni^{+2} ions have a tendency to substitute Li^+ sites,

which results in blocking Li diffusion pathways. Therefore, pure LNO is not favourable. Chen et al. [24] found that adding a small amount of Al improves both the thermal and electrochemical performance of LNO.

$LiMn_2O_4$ (LMO) is a promising candidate as a cathode material due to its low cost and less toxicity compared to LCO. Dahn et al. [19] stated that to minimize the oxygen generated under abusive conditions, LMO may be used instead of LCO or LNO. Armstrong and Bruce [25] have found out the capacity of LMO 270 $mAhg^{-1}$, which was promising when they have first conducted the electrochemical experiments on the material. Nevertheless, according to Gu et al. [26], the layered structure tends to change into the spinel structure during charge-discharge cycles, which was undesired. Due to the dissolution of manganese, capacity loss during the storage was also reported by Yunjian et al. [27]. Also, Takayuki et al. [28] reported the capacity loss due to changes in particle morphology. Therefore, LMO is not a desirable structure today.

2.2 NMC Cathodes

Because of their excellent electrochemical performance, NMC compounds are particularly appealing. They also offer a wide range of metal compositions, resulting in various attributes such as discharge capacity, rate capability, and safety. It is critical in NMC to achieve a stable structure that can operate at high voltages with high capacity. As a result, the research is focused on overcoming the disadvantages of NMC to be used in commercial applications. NMC has a similar or higher achievable capacity than LCO with a lowered amount of Co, which reduces toxicity and cost of the cathode while maintaining structural stability.

Yabuuchi and Ohzuku [29] have reported an insertion material of $Li(Ni_{1/3}Mn_{1/3}Co_{1/3})O_2$ (NMC) for Li-ion batteries, which shows about 200 $mAhg^{-1}$

capacity. Piskin and Aydinol [30] synthesized $Li(Ni_{1/3}Mn_{1/3}Co_{1/3})O_2$ using the spray pyrolysis method and post heat-treated the particles and found the first discharge capacity of 180.5 $mAhg^{-1}$ and 85.8% capacity retention after 31 cycles. The capacity retention of NMC materials is compromised when 4.7 V vs Li/Li^+ high-voltage cycling, according to Lin et al. [31].

Ni^{+2} has a radius of 0.69 Å, and Li^+ has a radius of 0.76 Å, which causes cation mixing between Ni and Li atoms [32]. Methods of synthesis are also crucial for NMC electrochemical performance because they affect the oxidation states of transition metals in the structure [33]–[35].

Mn content of NMC material affects the electrochemical properties. Liu et al. [36] studied that, as the Mn content increases, the capacity loss becomes more rapid, and the rate capability of NMC (532) decreases. Zheng et al. [37] found out that as the Mn content increases and the Ni content decreases, the cycling stability of Ni-rich NMC materials increases.

Ni content of NMC material also affects the properties. Ni-rich compositions increase the capacity, but the high Ni content resulted in lower structural and thermal stability due to its bias to react with electrolyte [38], [39]. High Ni content increases the risk for safety issues [40], [41]. This instability is one of the significant drawbacks of high Ni content NMC material.

Co content of NMC material also affects the structural stability and electrochemical performance. Ngala et al. [42] reported that the Co element stabilized the layered structure but suppressed the migration of metal ions to Li sites on NMC-444 material. They also said the reversible capacity of 180-155 $mAhg^{-1}$ and good rate capability. Yoshio et al. [43] reported that increased Co content suppresses cation mixing but did not report any effect on discharge capacity.

The electrochemical properties of NMC are also influenced by the morphology, porosity, particle size, and thus the specific surface area of the active materials. In this regard, the synthesis methods that result in different powder properties influence the performance of the cathode materials.

NMC materials may be synthesized by the sol-gel method. Lin et al. [44] studied the Al-doped NMC and synthesized the $LiNi_{1/3}Co_{1/3}Mn_{0.23}Al_{0.1}O_2$ via the sol-gel pyrolysis method. They have reported the initial discharge capacity as 194.6 $mAhg^{-1}$.

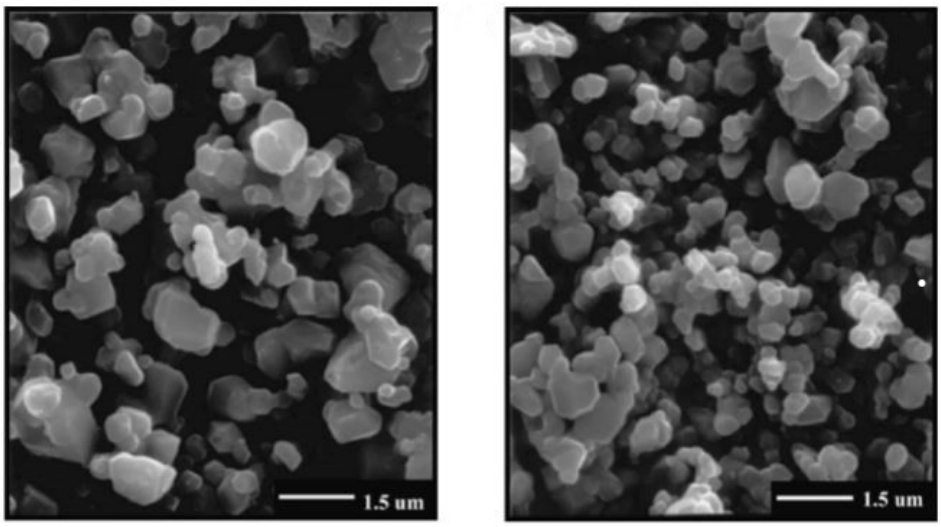

Figure 2.4 Sol-gel synthesized powders of $LiNi_{1/3}Co_{1/3}Mn_{0.23}Al_{0.1}O_2$ calcined at 900°C [44]

Many elements are researched to understand their effects of them on NMC material. Fe, Cu, Al, and W were used as alloying elements in this study. Therefore, the focus will be on these four elements.

The effects of Ti, Al, and Fe on the replacement of cobalt in NMC were investigated by Wilcox et al. [45]. Al-doped NMC could not be synthesized without impurity phases, resulting in lower capacity despite improved capacity retention. According to Wang et al. [46], Al-doped $Li_{1.2}Mn_{0.6-x}Mn_{0.2-x}Al_{2x}O_2$ (x=0.03), prepared by the

sol-gel method, has better capacity retention and average volume compared to the pristine sample. Zhang et al. [47] stated that Al-doped $Li(Li_{0.23}Ni_{0.15}Mn_{0.52}Al_{0.10})O_2$, which was also prepared by sol-gel method, has a better capacity of 180 $mAhg^{-1}$ at 20 mAg^{-1}, better capacity and better crystallinity compared to the $Li(Li_{0.23}Ni_{0.15}Mn_{0.62})O_2$.

Wilcox et al. [45] have found that Fe doped NMC exhibits a lower capacity and poorer rate capability than new NMC-111 material due to the kinetic limitations resulting from the antisite cation defects. According to Rajakumar et al. [48], Fe doped NMC exhibits improved performance.

Kim et al. [49] discovered that doping W (1 mol%) to the nickel rich ($x > 0.9$) $Li(Ni_xCo_yMn_{1-x-y})O_2$ layered cathode materials increases its stability which results in increased energy density. The battery delivered 247 $mAhg^{-1}$ discharge capacity between 2.7 and 4.3 V. This improvement is due to minor phase transformation from the layered to the cubic structure.

Jihad et al. [50] reported that 10% doping of Cu into the NMC material has a low value of the intensity ratio of (003) peak and (104) peak. Therefore, it has a high possibility of cation mixing, which is reported to decay the electrochemical performance due to the block of Li diffusion pathways [35]. Yang et al. [51] said that the sol-gel prepared, Cu doped $Li(Ni_{1/3-x}Co_{1/3}Mn_{1/3}Cu_x)O_2$ ($x=0-0.1$) cathode material exhibit better charge-discharge profile and rate capability compared to raw material. It is suggested that the presence of Cu decreases the cation mixing since the Cu^{+2} has a similar radius (0.73Å) compared to Li^+ (0.76Å), so the occupation of Cu in the Li layer is possible.

2.3 Magnetron Sputtering

Magnetron sputtering is one of the many surface coating methods. These methods divide into three groups based on how the deposition is made. The techniques seen in the figure below are available to deposit thin films onto various substrates.

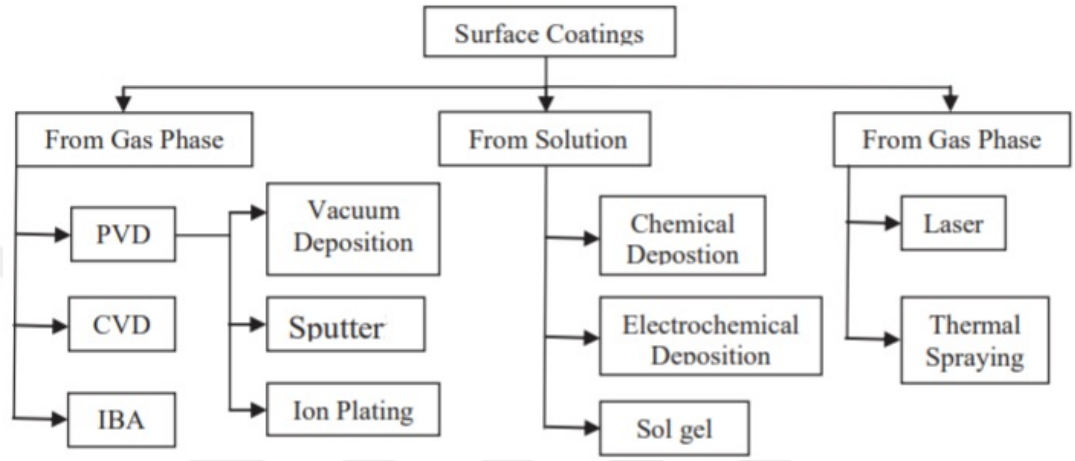

Figure 2.5 Surface coating methods [52]

Vapour deposition is a coating process in which a thin layer is formed by condensing coating material from a vapour phase at the substrate in a vacuum [53]. Magnetron sputter method is a physical vapour deposition (PVD) technique.

Sputtering requires launching a target material from the source to the substrate. It occurs in a plasma environment where ions are created from gasses like argon, nitrogen or oxygen [54].

According to Maurya et al. [55], during the sputtering process, which is the deposition of target atoms onto a substrate, the target material is bombarded by energetic ions, usually inert gas ions, which create the atmosphere. This collision removes (sputters) the target atoms from the target material. The typical sputtering process suffers from low deposition rates, high substrate heating and low ionization efficiencies, which have been overcome by the magnetron sputtering method.

Magnetron sputtered films outperform other films deposited by other PVD techniques and can perform the same way as much thicker films [56].

The schematic representation of the magnetron sputtering method may be seen in the below figure.

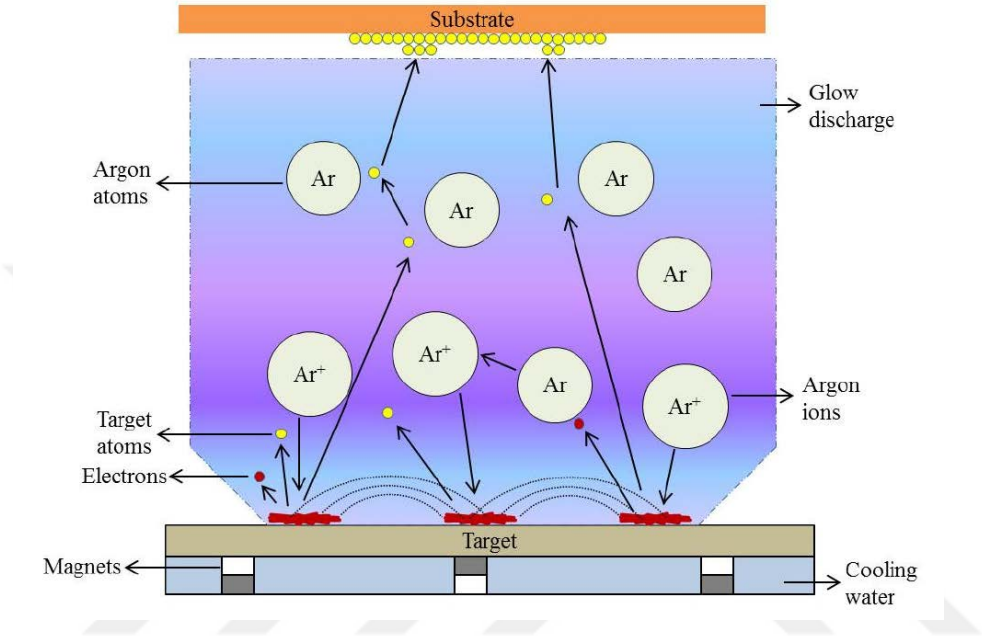

Figure 2.6 Schematic representation of one target rf magnetron sputter [55]

According to Surmenev et al. [57], the bombardment of the growing film with species from the sputtering target and the plasma has a significant impact on the properties of RF magnetron sputter deposited films. Deposition parameters such as working gas pressure and composition, target substrate distance, and substrate bias voltage are used to determine both.

Magnetron sputtering method was used in many different areas such as medical implants [57], fabrics [58], optics [59], semiconductors [60], batteries [61] etc.

The research of magnetron sputtered thin-film batteries was started by the deposition of LiCoO2, the commercially used cathode of Li-ion batteries. Cathode materials

produced by the magnetron sputtering method are binder-free, compared to the classical slurry applications [62]. Binder free cathodes do not use N-methyl-2-pyrrolidone (NMP), a toxic material used during electrode processing.

Wang et al. [63] deposited $LiCoO_2$ thin films by RF magnetron sputter in 3/1 Ar/O_2 atmosphere. Batteries were annealed after deposition at 700°C had a discharge rate of up to 1 $mA.cm^{-2,}$ and they have shown excellent reversibility. The research includes as-deposited (amorphous) cathodes, which had a lower capacity and high capacity loss per cycle than annealed ones.

Fragnaud et al. [64] deposited $LiCoO_2$ by spray pyrolysis and RF magnetron sputtering methods. The research showed that the RF magnetron deposited LCO thin-film micro-batteries were amorphous and showed high resistivity and no cell activity. After annealing, the crystalline formation was observed, but the electrochemical performance of the batteries was no match to the ones produced by the spray pyrolysis method. It is also reported that the Al foil substrate, on which LCO thin films were deposited, that used in liquid electrolyte were slowly attacked during cycling.

According to Qi and Wang [65], thin-film batteries promise high-power Li-ion batteries since the thinner electrodes allow faster lithium diffusion. Traditional 2D planar film geometries, on the other hand, may have limited energy loading due to their small footprint.

Letiche et al. [66] produced $LiMn_{1.5}Ni_{0.5}O_4$ thin films sputtered onto Pt current collector above Al_2O_3 layer above Si wafer. The thin films were deposited at 7mTorr and annealed at 700°C in the air after the deposition. They had a capacity of 65 $\mu Ahcm^{-2}.\mu m^{-1}$. The depositions were made under four different pressure conditions, and the researchers found out that the decreased pressure leads to dense thin films, and the pressure changes the orientation of the films.

Kuwata et al. [67] prepared an all-solid-state lithium-ion battery using $LiCoO_2$ as a cathode. The battery had an area of about 0.23 $cm^{2,}$ and the thickness was 2μm. The battery had a capacity of 9.5 $mAh.cm^{-2}$ in the second cycle.

Trask et al. [68] deposited LCO films thicker than 5μm at four mTorr operating pressure in an Ar and O_2 atmosphere formed by 46 sccm Ar flow and four sccm O_2 flow rate.

Wei et al. [69] applied the RF magnetron sputtering method to a smart window application using an LCO target material. The deposition was made in a gas mixture Ar/O_2 of 6/14 flow rate, and the rf power was 100W.

Priestland and Hersee [70] found that the deposition rate of Cu was increased when the pressure was raised, but the deposition rate of Al remained constant.

The PVD techniques in which magnetron sputtering is one of them have three challenges to be solved, according to Uzakbaiuly et al. [54]. These challenges are low deposition rates, obtaining lithium-deficient electrolyte or electrode, and the harmful effect of plasma during electrolyte deposition on the cathode electrode surface.

CHAPTER 3

EXPERIMENTAL PROCEDURE

Experiments were conducted in four different sections. First, the powders were synthesized then, the powders were used to produce sintered sputter targets. After that, these targets were used in magnetron sputtering experiments to produce cathodes with variable stoichiometries. Moreover, last, the batteries which were made with the cathodes were tested electrochemically.

3.1 Powder Synthesis

The method used to produce active materials in the study was the Pechini Sol-Gel method [71]. In this method, nitrates of the elements were used as precursor chemicals. The other two essential components in the Pechini polymeric gel method were citric acid, which was used as a chelating agent, and ethylene glycol, used as a polymerizer. The desired structure was obtained using these two materials with the help of the esterification reaction.

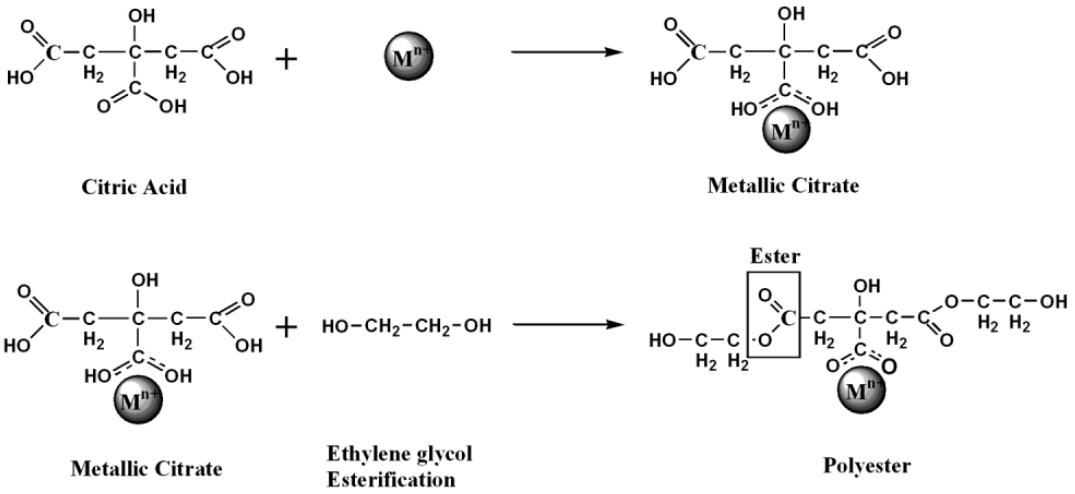

Figure 3.1 Pechini Method Reactions [72]

Production starts by calculating the additive amounts of the precursor materials and weighing them, considering the stoichiometric ratios. Then, citric acid and then nitrates were dissolved in pure water with the help of a magnetic stirrer. After dissolution, ethylene glycol was added at a 1:1 ratio of citric acid to ethylene:glycol. The solution was stirred in a heated magnetic stirrer at 180°C for 4-6 hours, allowing the water to evaporate and then gel formation started. The gel is put in an oven and left to dry completely at 110°C for 12-24 hours, depending on the elemental composition.

The pre-calcination process was carried out in a muffle furnace at 400°C for 4 hours. After the pre-calcination process was completed, the powders were ground in hand, then transferred to the heat treatment furnace for the calcination process by placing them in alumina containers. The calcination process was carried out for 24 hours at 800°C for all materials produced.

3.1.1 Characterization of Powders

The Bruker D8 Advance device obtained XRD of the powders at the end of the process. Diffraction data were collected within the 2-theta range of 10-90° with a scan rate of $2°{\cdot}min^{-1}$. Phase analysis was made out by Maud software to obtain information about the crystal structure of the powders.

In addition, microstructure examinations were conducted by FESEM Nova NanoSEM 430 device and EDS analyzes were also carried out. EDS data were collected from 3-4 different locations, and the average of this data is recorded.

3.2 Sintering of Powders

Sinter studies started by obtaining pellets from the powders produced. This study was first carried out with metal dies to optimize production parameters, and then the deformable dies were used to make sputter targets.

3.2.1 Sintering Using Metal Die

Each pellet is produced by 1.5-2g of powders varying in the elemental composition. Powders were ground in hand with 2% (weight) PVA. Later the powder and binder mixture was filled inside the die. 20 bar pressure was applied to the die for every pellet production.

The pelletized powders were sintered at different temperatures in the heat treatment furnace. The optimum temperature and time values required for sintering were determined with the heat treatments performed after each material's pellet production, completed in metal moulds.

After the sintering of the materials was completed, the density and porosity measurements of the produced pellets were made using the Archimedes method, as Unosson et al. described [73]. In the method, the dry weight of the pellet was measured after it was kept in the drying oven at 110°C for 5 hours (m_1). Then, the pellet was thrown into the water and held under a vacuum for 20 minutes. Then the weight was measured again in the water (m_2). After this process, the pellet removed from the water was weighed again in the wet state but in the air (m_3). After completing these measurements, density (ρ) and porosity (%porosity) were calculated using the following equations.

$$\rho_{pellet} = \left\{\frac{m1}{m_3 - m_2}\right\} \times \rho_{water} \qquad \text{Equation 3.1}$$

$$\%porosity = \left\{\frac{m_3 - m_1}{m_3 - m_2}\right\} \times 100 \qquad \text{Equation 3.2}$$

Phase analyzes of the produced pellets obtained by XRD characterization and microstructure examinations obtained by SEM characterization and EDS measurements were also made. In addition, the elemental ratios of these pellets were determined by the ICP-MS and ICP-OES methods.

3.2.2 Sintering Using Deformable Die

Deformable dies were required to produce actual size sputter targets. Since each target was in different stoichiometry, the change in the diameter after the heat treatment was different. A unique PTFE die was produced for each target. Examples of PTFE deformable dies may be seen in Figure 3.1.

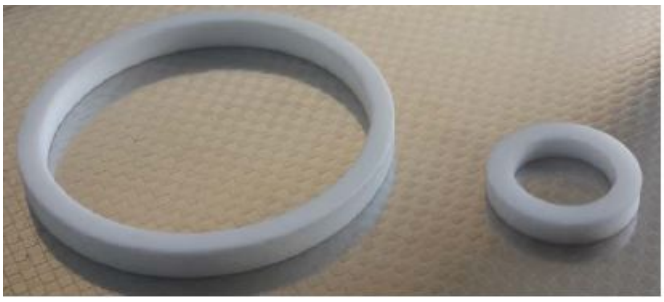

Figure 3.2 PTFE rings used as deformable die [74]

Using PTFE rings, Sari et al. [74] produced 2 inches La0.8Sr0.2CoO3-δ sputter targets with greater than 0.95 sintered density. 20 mm ring on the right in figure 3.2 was used for preliminary experiments, and the ring on the left was used to produce 2-inch targets.

To produce the pellets used in magnetron sputter, whose production was completed in metal moulds, 20mm deformable PTFE dies was used. In this pellet production method, the force applied on each die was updated to 100 MPa. As the diameter increased compared to the metal mould in production, the amount of material used is also increased, but the PVA used as a binder was kept constant at 2% by weight. The amount of material used for each target varies since their density varies.

After the production of pellets by 20mm deformable dies, changes in the pellets' diameter were noted before and after the heat treatment of the pellets to calculate the precise diameter required for each sputtering target.

Deformable dies were produced from a PTFE plate for each target's diameter change. Each target was made by filling the die with the powder-binder mixture, which was ground in hand. 100 MPa pressure is applied to the powders, and then the targets are heat-treated to their final form.

3.2.3 Characterization of Sintered Powders

The Bruker D8 Advance device obtained XRD of the powders at the end of the process. Diffraction data were collected within the 2-theta range of 10-90° with a scan rate of $2°{\cdot}min^{-1}$. Phase analysis was made out by Maud software to obtain information about the crystal structure of the powders.

In addition, microstructure examinations were conducted by FESEM Nova NanoSEM 430 device and EDS analyzes were also carried out. EDS data is collected from 3-4 different locations, and the average of this data is recorded.

Chemical compositions of the synthesized powders were obtained by using ICP-MS and ICP-OES methods.

3.3 Electrode Production by Magnetron Sputtering

The drawing view of the system consisting of a 50x50x50cm prismatic chamber may be seen in Figure 3.2. The chamber had initially four targets, one was three inches in diameter, and the other three were two inches in diameter. The targets used are two inches in diameter, and these targets are located above the central target.

The system includes two RF (300 watts) and one DC (600 V, 2A) power source. RF sputter guns can deposit insulator materials in addition to metallic ones. Each sputtering target has its quartz thickness sensor, which has a sensitivity of 0.1 and measures the related deposition rate. The thermal evaporation sources are located between the sputtering targets and are powered by 1500 W power supplies. As a result, the technology supports simultaneous and layered depositions.

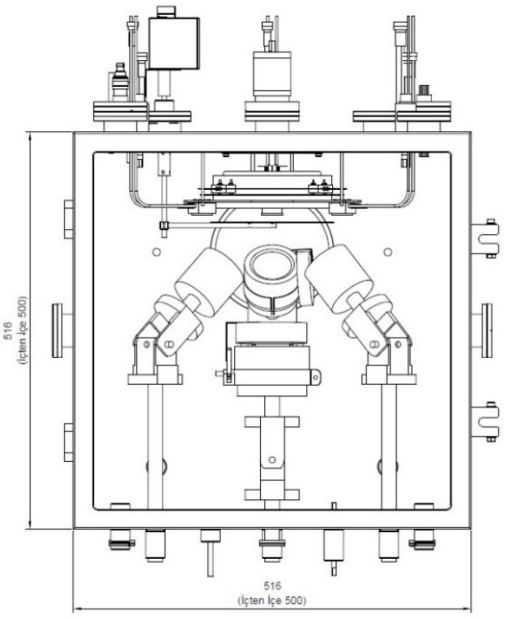

Figure 3.3 Drawing of the chamber of magnetron sputter

The three-target system in the figure shown above was in equilateral triangle geometry, and the generators in this geometry have a centre-to-centre distance of 300mm. Each of the substrates used in this setup was a circle and had a diameter of 18mm. There were 21 substrates in the triangular distribution. For a better understanding, see Figure 3.3.

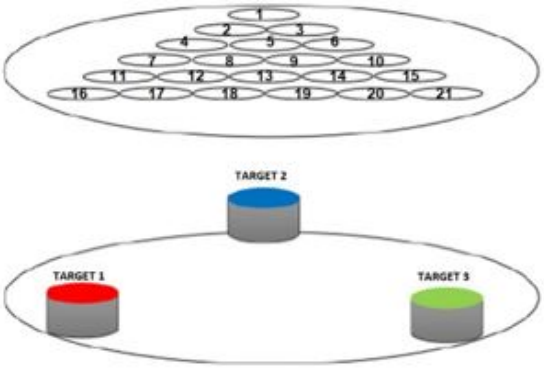

Figure 3.4 Positions of the targets with respect to the substrates

The distances and angles of the targets to the substrate were fixed. The central target holder, which was not used, was 92.5 mm from the substrate plane. Other targets were adjusted by aligning their lower ends with the central target holder.

The thickness measurement sensors were out of use. Therefore, the thickness measurements were made in SEM.

The twenty-one substrates, Ni-foils 18 mm in diameter, are placed in the substrate holder. The substrate holder was triangular in that each corner was directed to a target.

Nickel was selected as substrate material since it was a commonly used current collector for cathodes and had higher heat resistance than aluminium.

Circular weights, 18 mm in diameter and made from Cu plate, were placed on top of each substrate to ensure that they did not move during the vacuum process. These weights also minimize the effect of heat, which causes folding of the nickel substrates that generate uneven deposition on the substrate.

Depositions were made under five mTorr pressure. In the first set of experiments, the flow rate was 20 sscm for Ar gas, and it was 18 sscm for Ar and 6 sscm for O2 gasses for the second set. The deposition time was 10 hours for all the experiments.

Power was 60 Watts for the cobalt-containing targets and 100 Watts for the other two targets.

3.3.1 Characterization of Cathodes

Microstructure examinations were conducted by FESEM Nova NanoSEM 430 device, and EDS analyzes were also carried out. EDS data were collected from 3 - 4 different locations, and the average of this data was recorded.

3.4 Cell Assembly and Electrochemical Testing

The produced materials were used as cathodes, lithium foils with 18mm diameter, and 0.3 mm thickness were used as anode materials. Glass microfiber with 18 mm diameter was used as a separator. Before the cell was sealed, 1M $LiPF_6$ in a 50:50 EC:DEC solution was added.

Produced batteries were charged at 0.2 mA for a maximum of 2 hours as a first stage then, they were charged at 0.1 mA for a maximum of 4 hours as the second stage for charging. The first stage had a cut off voltage at 4.2 V and the second stage had a cut-off voltage at 4.3 V. The charged batteries were then discharged at 20 mA for a maximum of 12 hours. The cut-off voltage was 1.3 V. Later, these batteries were discharged at 40mA for a maximum of 12 hours, and the cut off voltage was 1.3 V. During this charge and discharge cycles, cyclic capacity plots and voltage profiles were recorded.

CHAPTER 4

RESULTS AND DISCUSSION

4.1 Production and Characterization of Powders

Table 4.1 Targeted compounds and chemical and structural summary results. Unspecified structures are layered.

Code	Target Stoichiometry	EDS	XRD
C4	$Li_{1.03}Co_{0.8}Ni_{0.2}O_2$	%78.81 Co %21.11 Ni	$LiCo_x(Ni)O2$ (%100)
C5	$Li_{1.03}Co_{0.7}Ni_{0.2}Cu_{0.1}O_2$	%70.26 Co %21.54 Ni %8.19 Cu	$LiCo_x(NiCu)O2$ (%100)
C6	$Li_{1.03}Co_{0.7}Ni_{0.2}Fe_{0.1}O_2$	%69.1 Co %20.46 Ni %10.44 Fe	$LiCo_x(NiFe)O_2$ (%100)
M3	$Li_{1.03}Mn_{0.8}Ni_{0.2}O_2$	%79.51 Mn %20.49 Ni	$Li_2Mn_xO_3$ %72.32 + spinel $LiMn_x(Ni)O_4$ (%27.68)
M4	$Li_{1.03}Mn_{0.7}Ni_{0.2}Cr_{0.1}O_2$	%68.58 Mn %21.16 Ni %10.25 Cr	$Li_2Mn_xO_3$ (%76.47) + spinel $LiMn_x(NiCr)O_4$ (%23.53)
M5	$Li_{1.03}Mn_{0.7}Ni_{0.2}Mo_{0.1}O_2$	%72.1 Mn %20.04 Ni %7.86 Mo	$Li_2Mn_xO_3$ (%37.71) + spinel $LiMn_x(NiMo)O_4$ (%62.29)
A5	$Li_{1.03}Ni_{0.8}Mn_{0.2}O_2$	%79.41 Ni %20.59 Mn	$LiNi_x(Mn)O_2$ (%100)
A6	$Li_{1.03}Ni_{0.7}Mn_{0.2}Al_{0.1}O_2$	%68.48 Ni %20.75 Mn %10.77 Al	$LiNi_x(MnAl)O_2$ (%100)
A7	$Li_{1.03}Ni_{0.7}Mn_{0.2}W_{0.1}O_2$	%70.99 Ni %20.87 Mn %8.14 W	$LiNi_x(MnW)O_2$ (%94.86) + $Li_2Mn_xO_3$ (%5.14)

Three 2-inch sputter targets were used in this work. It was aimed to produce powders with nine different stoichiometries.

The code numbers, stoichiometry and chemical and structural characterization results obtained after the production studies of the targeted compounds were summarized in Table 4.1. These materials will be mentioned using their codes in the rest of this work.

Success has been achieved in the production of targeted stoichiometry when EDS results were considered. The deviations in the table are within the margin of error of the EDS analysis. The phases of the materials in the C4, C5, C6 group and A5, A6 group were in a layered structure. M3, M4, M5 and A7 material groups have layered and spinel structures, another commercial cathode structure widely used in Li-ion batteries. Determining the phases of the materials is very important in terms of recognizing the material. However, it should be noted that these compounds were more critical to be sintered later and to have a homogeneous chemical structure when used as a sputtering target. Therefore, achieving the targeted stoichiometry was more critical than single-phase material production in this stage of work.

Since Li element cannot be seen in EDS analysis, inductively coupled plasma optical emission spectroscopy (ICP-OES) method should be used to determine the amount of Li element. However, since there may be a loss of Li during the sintering process, it is decided to use this analysis for the pellets that completed the sintering work.

The results of the XRD analyses obtained after the calcination process applied to the materials may be seen in Figure 4.1, and the detailed analysis results may be seen in Table 4.2.

The green colour represents the peaks of the layered structure, and the red represents the spinel structure.

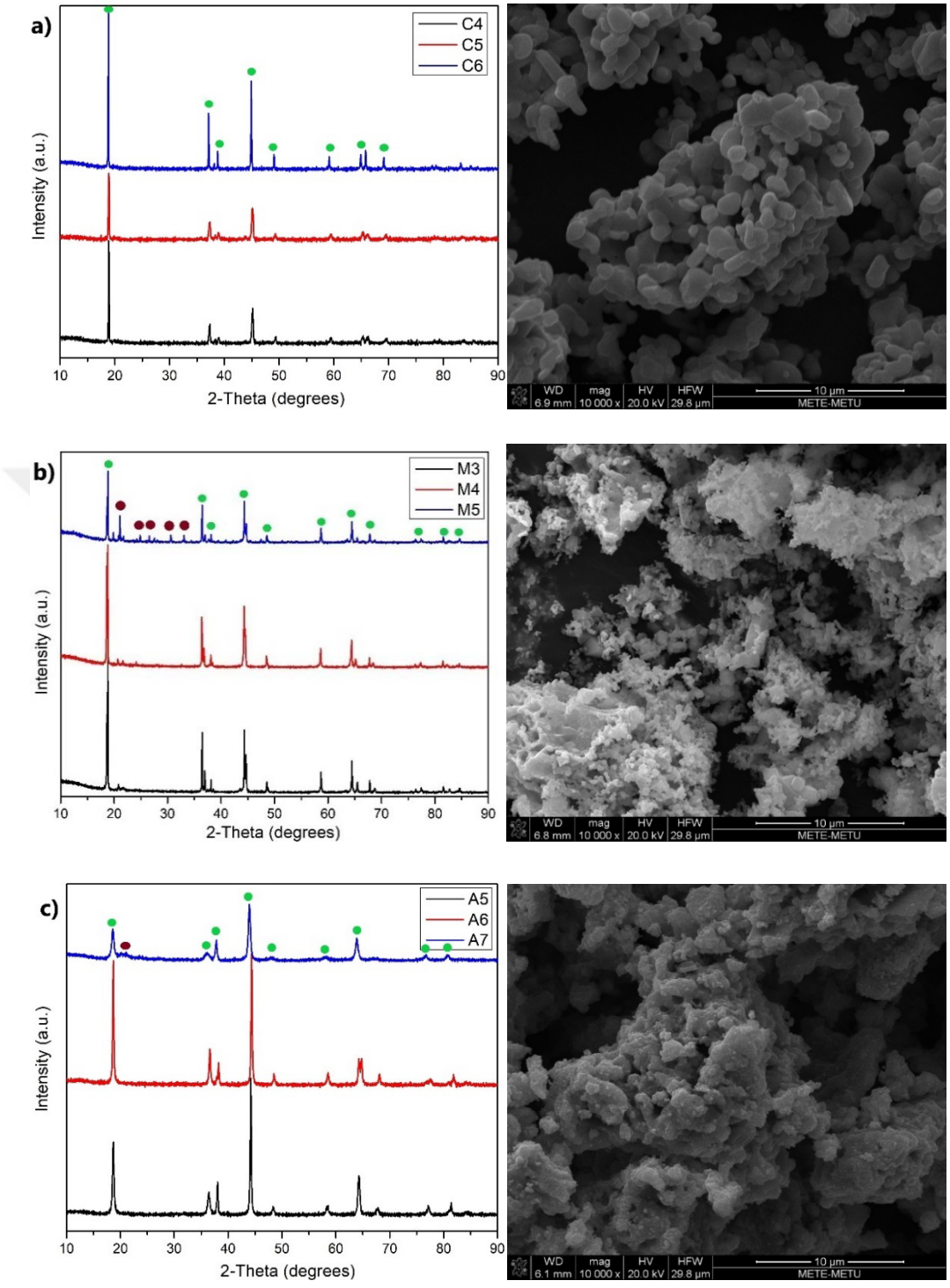

Figure 4.1 XRD results and the SEM images of a) C4 b) M3 c) A5

Table 4.2 Detailed XRD results

Code	Lattice Parameters				O_2	Phase	Symmetry
	a	b	c	beta (degree)			
C4	2.8265		14.0977		0.2414	$LiCo_xO2$	trigonal
C5	2.829		14.1042		0.2418	$LiCo_xO2$	trigonal
C6	2.8371		14.1462		0.2409	$LiCo_xO2$	trigonal
M3	5.0187	8.5628	5.042	109.32	0.2133	Li_2Mn_xO3	monoclinic
	5.891		8.2027		0.2736	$LiMn_xO4$	tetragonal
M4	5.0234	8.6059	5.0388	109.3	0.2225	Li_2Mn_xO3	monoclinic
	5.9415		8.0654		0.3083	$LiMn_xO4$	tetragonal
M5	4.9852	8.5436	8.5436	109.36	0.237	Li_2Mn_xO3	monoclinic
	5.7838		8.1996		0.2519	$LiMn_xO4$	tetragonal
A5	2.8959		14.277		0.2456	$LiNi_xO2$	trigonal
A6	2.8807		14.2581		0.2438	$LiNi_xO2$	trigonal
A7	2.9108		14.317		0.2424	$LiNi_xO2$	trigonal
	5.07	8.9174	4.9967	110.56	0.1924	Li_2Mn_xO3	monoclinic

Looking at Figure 4.1, it may be seen that the peaks of the C4, C5 and C6 materials were in almost the same positions and the same peaks were present in all three materials. These peaks indicated that it was a phase with a layered structure. When the Rietveld analysis results were examined from Table 4.2, it may be seen that all three materials were single-phase and have exact symmetry. The value of x used in the table means that the percentage of Co may be variable. When viewed from Table 4.1, it may be understood that C5 and C6 materials were obtained by subtracting 0.1 from the main element, cobalt, and adding alloying element. When the lattice parameters in Table 4.2 were examined, copper for C5 material and iron for C6 material, which was in the same atomic position as cobalt in the atomic structure, changed the structure. Upon a closer look at the lattice parameters, it may be seen that C5 had higher values than C4, and C6 had higher values than C5. This was because the copper and iron elements filled the position of the cobalt element in the crystal structure. In octahedral coordination, +3 valence cobalt has an ionic radius of

0.61 pm, iron 0.645 pm and copper 0.54 pm. Considering these values, the increase in the lattice parameters of C6 may be explained by the replacement of Co^{+3} by Fe^{+3}. The increase in the lattice parameters of C5 was an indication that the displacement was not with Cu^{+3} but with Cu^{+2} because the Cu^{+2} ion has a diameter of 0.73 pm.

Looking at Figure 4.1, XRD results of M3, M4 and M5 materials were the same except for the range of 20°-35°. In this range, specific peaks were the same, but it was seen that there were much more peaks in the M5 coded material compared to the other two materials. Table 4.1 suggests that M3, M4 and M5 materials were two-phase materials. The number of peaks (between 20°-35°) in M5 material was higher and more intense than other materials was due to the higher percentage of the spinel structure, as shown in Table 4.1. Comparing the lattice parameter changes of the materials in Table 4.1, the primary material was M3. When the manganese ratio in M3 material was reduced by 0.1, the M4 and M5 elements were obtained by adding the alloying elements, chromium, and molybdenum. The crystal structure changed with the effect of these alloying elements.

XRD peaks on Figure 4.1 of the A5, A6 and A7 materials were almost the same, but there were three extra peaks in the 20°-23° range in the A7 coded material. These peaks were found to belong to $Li_2Mn_xO_3$ in the spinel structure. The remaining belong to the layered structure, confirmed by the Rietveld analysis. A5 and A6 materials were single-phase and had exact symmetry. Table 4.1 suggests that A6 and A7 materials were formed by subtracting 0.1 from nickel, the main element in A5 material. When lattice parameters are observed, both the a and c parameters of A6 may decrease when both the a and c parameters of A7 increase. In this case, the ionic radii of aluminium and tungsten elements, which replace nickel in the crystal structure, should be considered. Nickel has an ionic radius of 0.6 pm, aluminium has 0.54 pm, and tungsten has 0.66 pm. In the light of this information, the shrinkage of

the crystal structure due to smaller aluminium and the enlargement of the crystal structure due to the larger tungsten may be explained.

4.2 Production and Characterization of Sputter Targets

4.2.1 Metal Mold Sintering Process

Produced powders were then used in sintering studies. The sintering studies was started with the pressing of pellets from the produced powders in steel moulds with a diameter of 13 mm. 2% by weight polyvinyl alcohol was used as a binder; this ratio varied by 0.5% for each material to reach the required wetting. The reason for this was that the densities of each material were different from each other, and the resulting volume was also different. When the powder and binder mixture was prepared, it was pressed under the mechanical press at 15 bar pressure for 30 seconds. The pellets obtained for each material were then sintered at various temperatures for 12 hours under atmospheric conditions. Being above the calcination temperature is vital for better and faster sintering. However, reaching very high temperatures may also lead to increased lithium loss from the material. Sintering parameters may be seen in Table 4.3.

Table 4.3 Temperatures and times of sintering work

Code	Temperature (°C)	Time (h)
C4	850, 900, 950	12
C5	850, 900, 950	12
C6	850, 900, 950	12
M3	850, 900, 950	12
M4	850, 900, 950	12
M5	850, 900, 950	12
A5	850, 900, 950	12
A6	850, 900, 950	12
A7	850, 900, 950	12

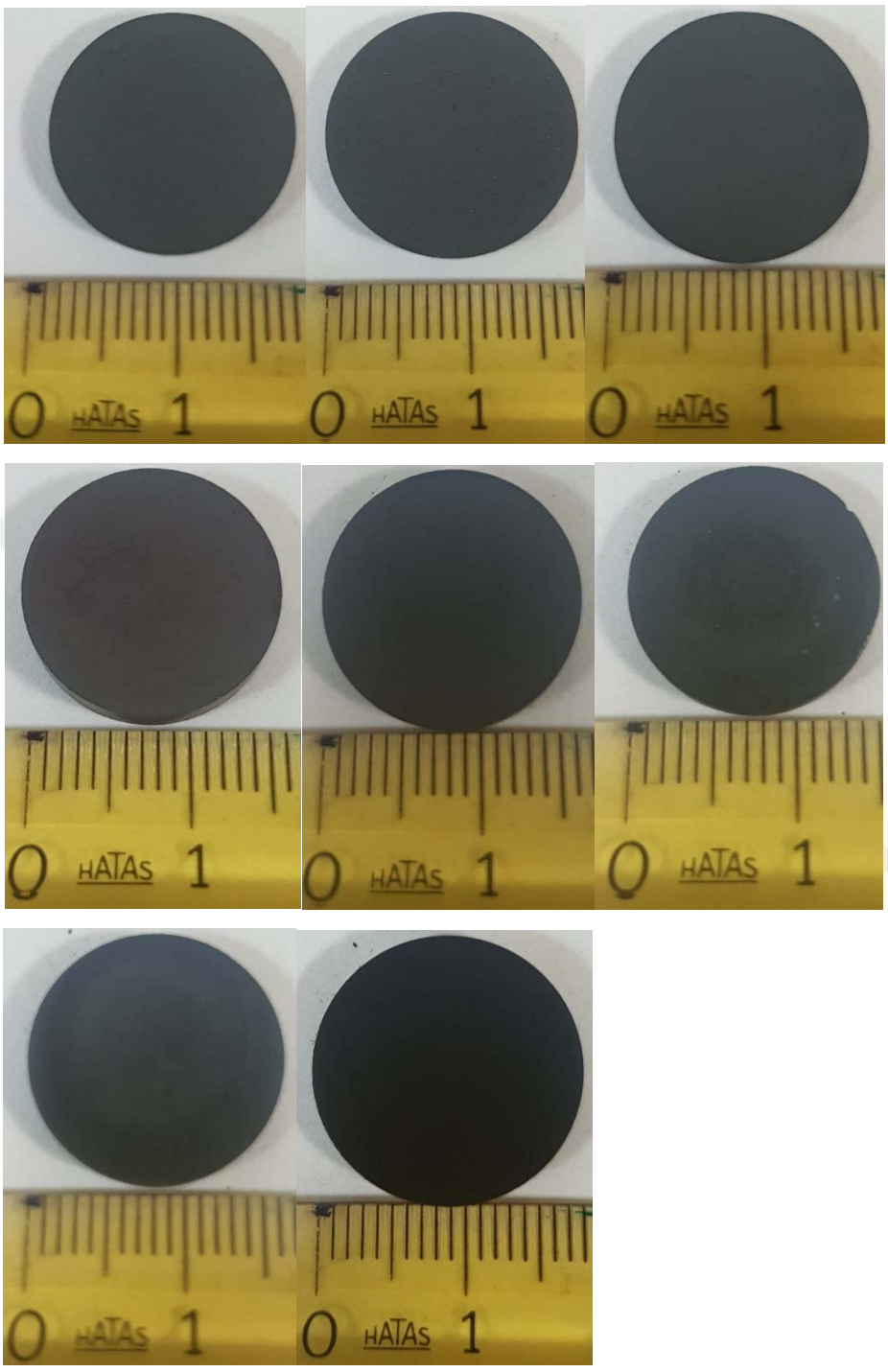

Figure 4.2 Photographs of pellets prepared with metal mould after sintering at 900° 1st row: C4, C5, C6, M3 2nd row: M3, M4, A5, A6, A7 3rd row: A6, A7

When the sintering of the materials was completed, the porosity measurements were made using the Archimedes method. Results of the Archimedes method may be seen below in Table 4.4.

Table 4.4 Diameter change and porosity measurement results obtained after sintering studies

Code	Sintering Temperature (°C), time (h)		
	850, 12	**900, 12**	**950, 12**
	Porosity (%)	**Porosity (%)**	**Porosity (%)**
C4	34.60	32.30	37.87
C5	25.10	18.09	13.18
C6	26.60	13.31	6.94
M3	33.40	25.99	26.89
M4	31.10	23.64	21.64
M5	-78.06	-6.99	-5.43
A5	4.03	0.94	1.01
A6	11.84	2.19	2.34
A7	37.93	28.62	39.77

When the porosity measurements are examined in Table 4.4, it may be easily noticed that there was an incorrect measurement in the M5 coded material. This error was the cracks formed on the pellet, as mentioned before. During the vacuum process in water, which was one of the porosity measurement stages, the integrity of the pellets was broken. The pellet sintered at 850 °C was partially dispersed in the water.

The surface integrity of the pellet produced from M5 coded material was impaired, and crack formation was observed. It was thought that the binder was trapped inside. After the pellet was prepared, it was kept at a low temperature of 400°C for 1.5 hours to solve this problem so, the binder inside of the pellet may evaporate. However, the crack formation was observed at the end of this trial. Then, as a second trial, it was kept at 300°C for 1.5 hours and then sintered. The reason for choosing 300°C here

is that it is just above the evaporation temperature of the PVA in the PVA solution used as the binder. This method also did not yield results; cracks were formed on the surface. Then, the pellet produced by using higher pressure without a binder was tested for sintering and cracks were observed in this pellet. The values for the M5 coded material in Table 4.4 were obtained from the pellets in the best condition produced.

After a series of failed experiments, which are told above, to produce the M5 pellet, the material was decided not to be produced, and the material was removed from the rest of this study.

During sinter studies, porosity measurements have been influential in determining the most suitable temperature for each material. The ability of the targets to retain their mechanical structure during the sputtering process is due to their low porosity. On the other hand, diameter changes helped realize possible material losses and understand the material's sinter characteristics. Since the mould used while preparing the pellet was metal, it was not deformable. In the light of the results obtained in Table 4.4, the selected sinter temperatures and times may be seen below in Table 4.5.

Table 4.5 Selected sintering temperatures

Code	**Temperature (°C)**
C4	900
C5	950
C6	950
M3	900
M4	950
A5	900
A6	900
A7	900

The XRD diffractograms of the sintered pellets, together with the diffractograms of the powders used in their production, may be seen below in Figure 4.3. The green colour represents the layered structure's peaks, and the red colour represents the spinel structure's peaks

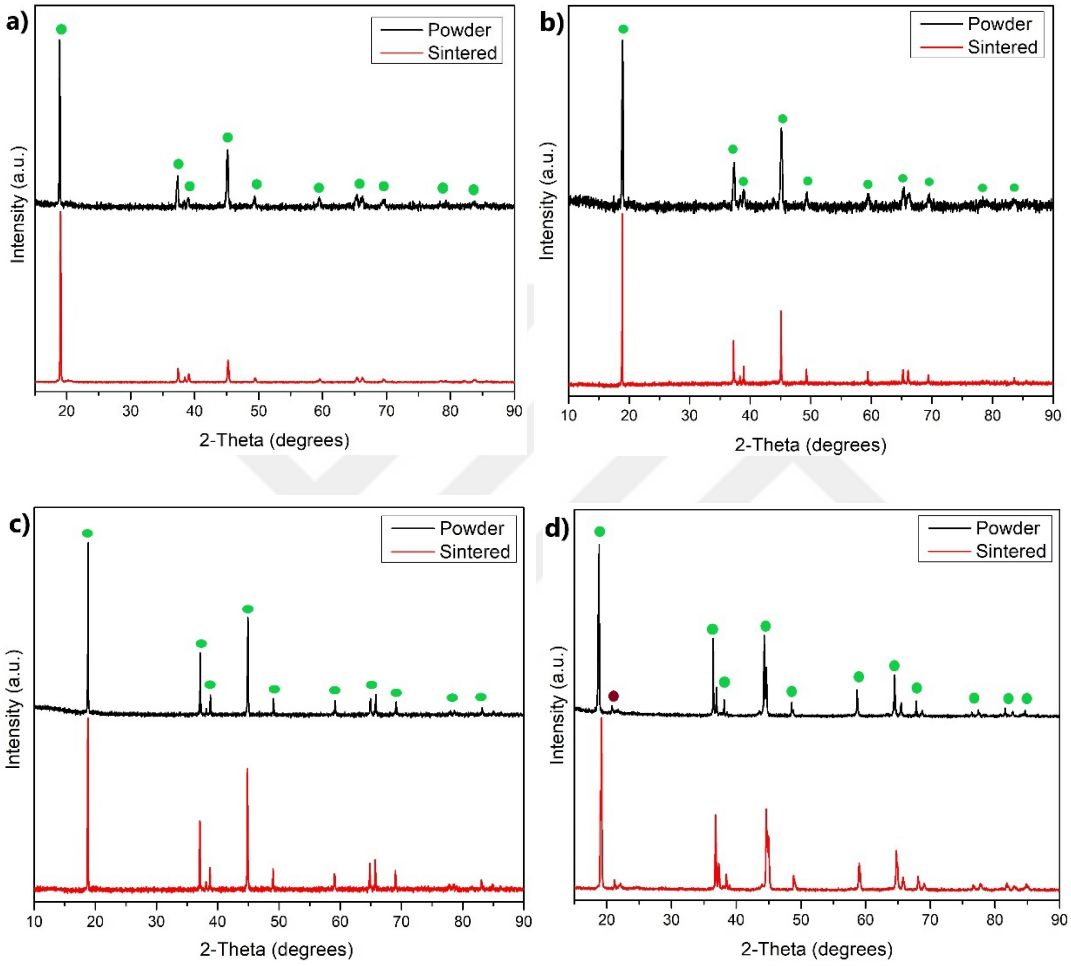

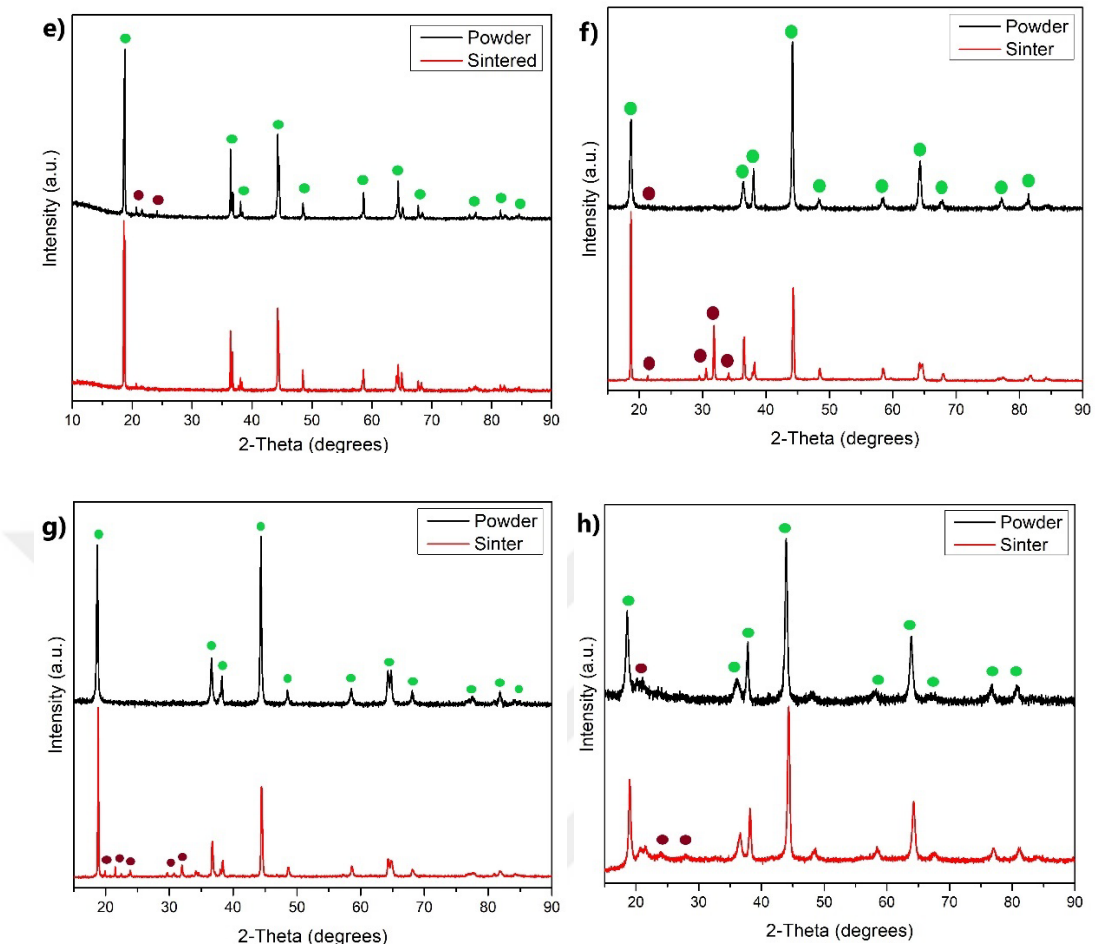

Figure 4.3 XRD analysis results of powder and sintered materials of a) C4 b) C5 c) C6 d) M3 e) M4 f) A5 g) A6 h) A7

It was observed by the results of Figure 4.3 that C4, C5, C6, M3, and M4 coded materials had not undergone any change after sintering; only the intensity values of the peaks changed. The spinel structure peaks of A7, mentioned in the detailed XRD analysis section, became more evident due to the density change and reduced background noise. When the Figure 4.3 graph of the sintered state is examined, the peaks become more prominent and appear as four different peaks instead of three in powder form that belongs to the spinel phase in the $Li_2Ni_xO_3$ structure as mentioned in the detailed XRD analysis. The appearance of the fourth peak at 28° was an

indication that the percentage of spinel structure increased after the sintering process. It had been observed that there were peaks in the A6 material after sintering between 20° and 35°. These peaks belong to the $Li_2Ni_xO_3$ phase in spinel structure and the Li_2CO_3 phase as in the A7 material. The peaks seen after sintering in the A5 coded material were found to belong to Li_2CO_3 and the layered Li_2MnO_3 phases and were confirmed by Rietveld analysis. It was thought that the presence of the Li_2CO_3 phase might be due to PVA being used as a binder in pelleting. However, the percentage of the Li_2CO_3 phase was low and did not pose any problem for the subsequent sputtering process since the critical parameter was the stoichiometry of the target materials.

The EDS analyses obtained from the pellets of the materials after the selected sinter temperatures are given in Table 4.6. According to these results, the slight difference between the sintered materials and the powders of these materials was acceptable since it was within the margin of error of the EDS analysis.

Table 4.6 Comparison of the EDS analysis of the powder states of the materials and the state after sintering

Code	EDS (powder)	EDS (sintered)
C4	%78.81 Co %21.11 Ni	%78.89 Co %20.11 Ni
C5	%70.26 Co %21.54 Ni %8.19 Cu	%65.72 Co %20.19 Ni %14.09 Cu
C6	%69.1 Co %20.46 Ni %10.44 Fe	%64.21 Co %24.81 Ni %10.98 Fe
M3	%79.51 Mn %20.49 Ni	%80.36 Mn %19.64 Ni
M4	%68.58 Mn %21.16 Ni %10.25 Cr	%69.53 Mn %20.63 Ni %9.84 Cr
M5	%72.1 Mn %20.04 Ni %7.86 Mo	%77.63 Mn %18.4 Ni %3.97 Mo
A5	%79.41 Ni %20.59 Mn	%79.51 Ni %20.49 Mn
A6	%68.48 Ni %20.75 Mn %10.77 Al	%68.39 Ni %19.71 Mn %11.9 Al
A7	%70.99 Ni %20.87 Mn %8.14 W	%66.62 Ni %20.68 Mn %12.69 W

4.2.2 Deformable Mold Sintering Process

The production of the targets was continued with the deformable rings, which were made from PTFE. As the first stage, the small-scale production of the targets was continued with the 20mm inside diameter PTFE rings. Sintering parameters are the same as metal mould target production. Deformable rings were used to calculate the shrinkage after the sintering stage so that the 2-inch diameter targets may be produced. A unique PTFE ring was made for each material since the shrinkage amount was unique. The pellets were built with the help of deformable rings, and then they were sintered.

A series of preliminary experiments were conducted to test the pressure applied on the pellets and the time consumed during the pressing. The limits of the press machine were also considered. 100 MPa pressure was determined for large-scale, and small-scale PTFE rings for target production. The force was applied to the ring with an inner diameter of 20 mm was selected as 31.4 kN and was applied using a press machine for 60 seconds.

In Table 4.7, diameter measurement values of the prepared pellets were given to understand the characteristics of the expandable PTFE rings (deformable moulds) in the preparation of small diameter targets.

Table 4.7 Diameter measurements and diameter change percentages in the deformable PTFE molds

Code	Sintering Temperature (°C)	Inner Dia. (mm)	Measurement (mm)
C4	900	20	21.2
C5	950	20	19.02
C6	950	20	18.95
M3	900	20	17.91
M4	950	20	19.68
A5	900	20	17.33
A6	900	20	18.61
A7	900	20	20.72

Upon observing the results in table 4.7, it was clear that C4 and A7 materials were expanded after sintering, whereas the diameter of all remaining materials decreased. These results were parallel to those in Table 4.4. Diameter change depended only on the sintering process when a metal mould was used. Nevertheless, when a deformable PTFE mould was used, the diameter changed due to both the pressing and sintering processes. Within the light of these results, large scale target production was started.

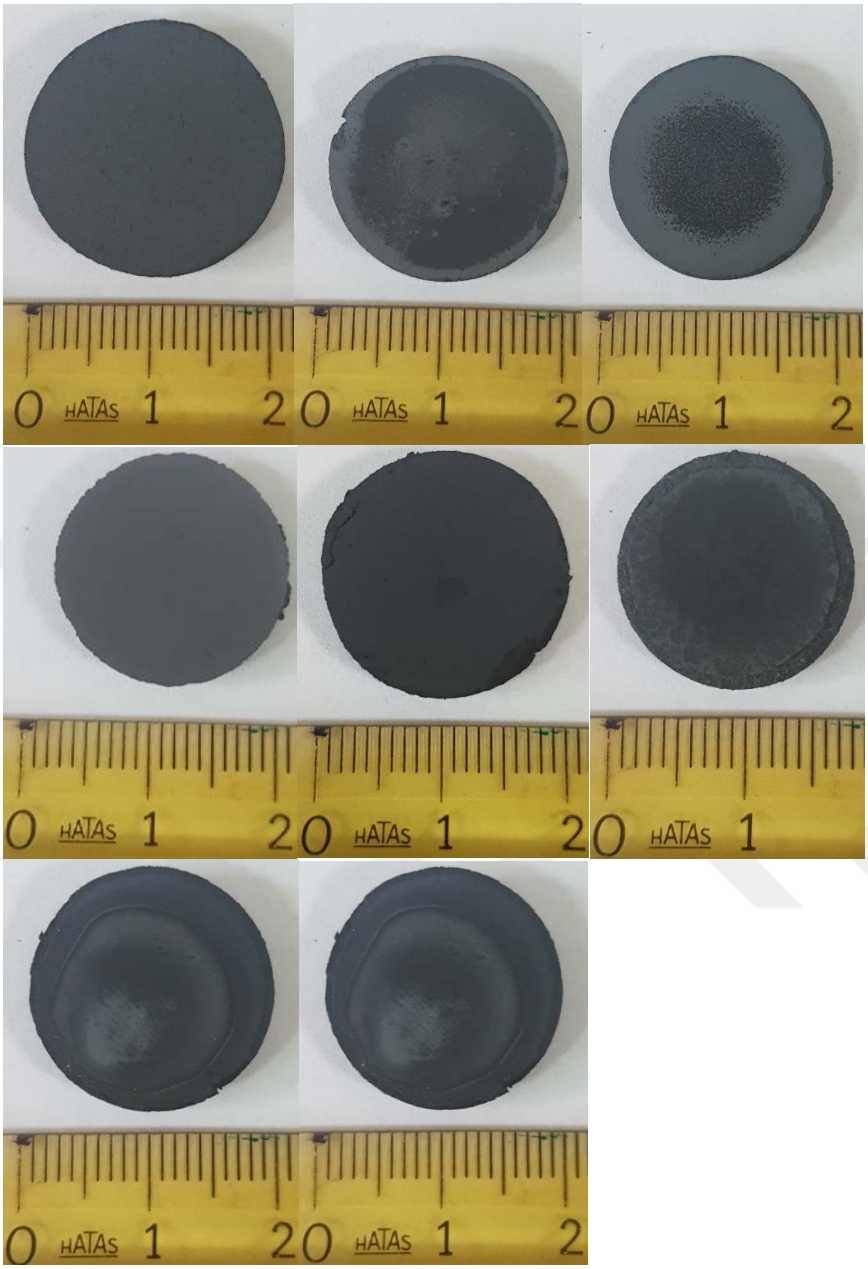

Figure 4.4 Photos of pellets produced by PTFE rings. First row: C4, C5, C6, second row: M3, M4, M5, third row: A6, A7

As it may be seen in Figure 4.4, these experiments using expandable PTFE rings, small targets could be produced without any crack formation on their surfaces. The defects that may be seen, when looked carefully, were that the side surfaces were not

smooth and the upper surfaces of the C5 and M4 pellets had minor roughness at the points where they met the side surfaces. The side and top surface roughness did not cause any problems during the use of the targets in the sputtering process. The roughness of the upper surfaces was the experimental error, which occurs when separating the PTFE ring from the pellet after the pressing process.

After the experiments on small scale deformable PTFE moulds, 2-inch (5.08 cm) targets were started. During the pressing process of these materials, a force of 282.6 kN was applied for 60 seconds to use the same pressure (100MPa) applied to the small-scale deformable PTFE rings.

The final products resulting from the production of 2-inch pellets may be seen in Figure 4.5.

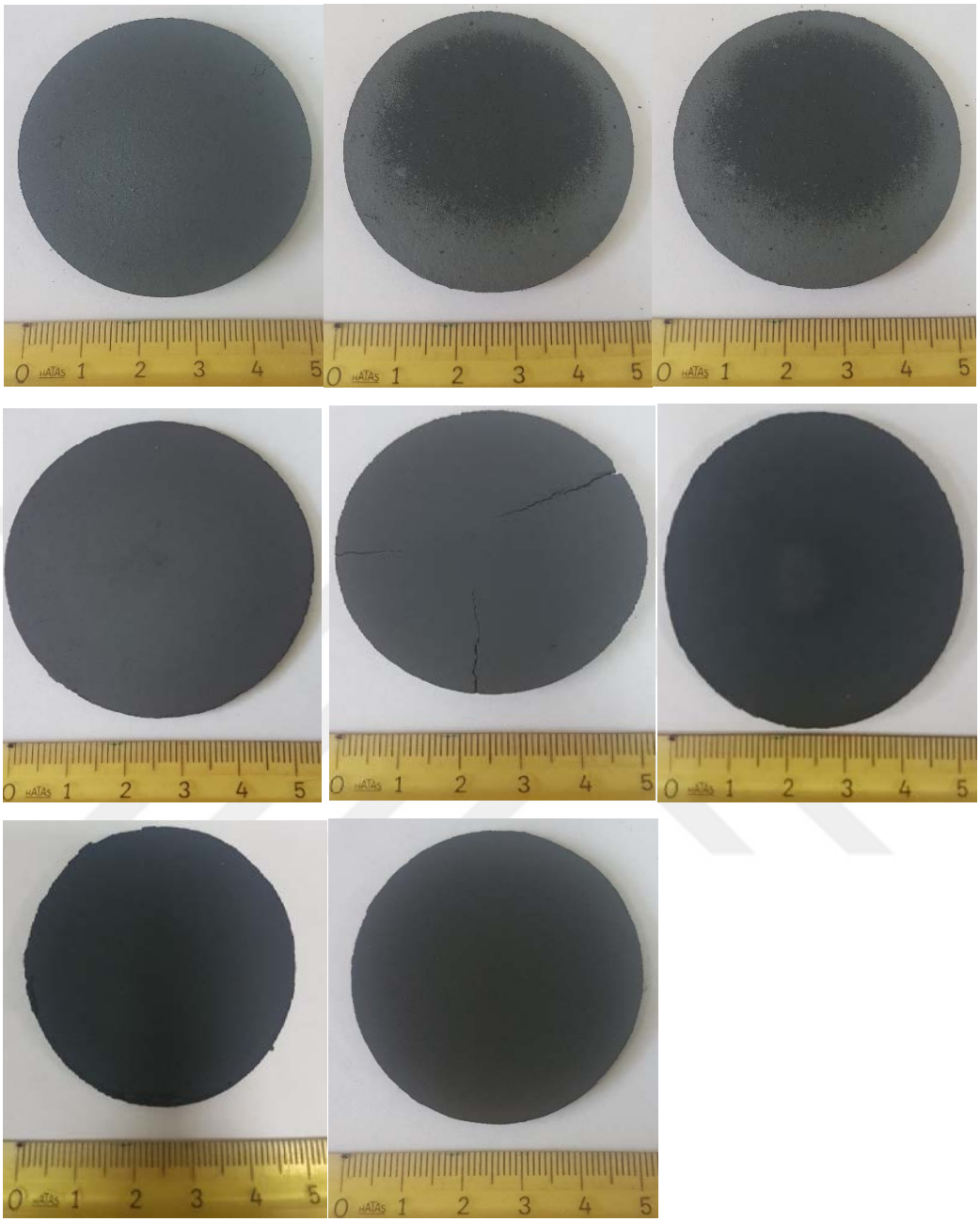

Figure 4.5 Sintered versions of 2-inch diameter targets.

First row: C4, C5, C6, second row: M3, M4, M5, third row: A6, A7

The diameter of each generator was different from the other. This was because the shrinkage of each material was different during the sintering process. Deformable PTFE mould with a diameter close to the ideal shrinkage was used for each material, calculated by the post-sinter shrinking studies carried out before. The roughness on the targets' side surfaces may be seen in Figure 4.5, but this was not a problem since the side surfaces were sanded to reach the 2-inch diameter.

A crack has occurred in the M4 targets. This crack did not happen before, with 20mm diameter deformable PTFE rings during pressing and sintering work. However, when switching to large diameter PTFE rings, cracks occurred after the pressing process on the surface of the M4 target, which was contained chromium as an alloying element. The amount of binder and the pressure applied was reduced, and the time was shortened to eliminate this crack, but the problem could not be solved. Since an uncontrolled and undesirable sputtering experiment would have occurred, the production of the M4 target was abandoned.

In order to understand whether there was a loss of lithium element during the sintering process, inductively coupled plasma optical emission spectroscopy (ICP-OES) analysis were performed. The result of the analysis of the targets of C4, M3 and A5 pellets, which were compounds that did not contain the fourth alloying element, may be seen in table 4.8.

Table 4.8 Stoichiometric values of the elements after ICP-OES characterization

Element	**Code**		
	C4	**M3**	**A5**
Li	1.01	1.04	0.99
Mn		0.8	0.22
Co	0.82		
Ni	0.2	0.19	0.82

When table 4.8 and table 4.1 was compared, it may be seen that values of targeted stoichiometry were obtained. It was understood that the loss of lithium during the procedures was reasonable.

Inductively coupled plasma characterization was used for the other five targets as well. ICP-MS characterization was done for the remaining five targets. The results may be seen below in table 4.9 and table 4.10.

Table 4.9 ICP-MS results of C5, C6, A6 and A7

Code	Li (ppm)	Co (ppm)	Mn (ppm)	Ni (ppm)	Cu (ppm)	Fe (ppm)	Cr (ppm)	Al (ppm)	W (ppm)
C5	60572	401589	17	113173	61310	100	23	120	0
C6	59997	412144	17	116133	78	55109	52	3315	0
A6	60902	99	98291	397699	5	217	39	23695	0
A7	55068	94	93695	378740	9	177	11	104	439

Table 4.10 Calculated moles of C5, C6, A6 and A7

Code	Li (mol)	Co (mol)	Mn (mol)	Ni (mol)	Cu (mol)	Fe (mol)	Cr (mol)	Al (mol)	W (mol)
C5	0.898	70.000	0.003	19.808	9.910	0.018	0.004	0.046	0
C6	0.857	70.000	0.003	19.805	0.012	9.876	0.010	1.230	0
A6	0.929	0.017	18.481	70.000	0.001	0.040	0.008	9.072	0
A7	0.971	0.017	18.499	70.000	0.002	0.034	0.002	0.042	0.026

The results in table 4.10 suggest that the centre performing the test made a mistake in the A7 element. Although it was known that there was tungsten element in the A7 target, the ppm value of the W element of the A7 target was at the pollution level rather than the 0.1mol in the target stoichiometry. Therefore, it was evident that there was an error in the result. The results of the other three targets (C5, C6, A6) parallel the targeted stoichiometry, just like the results of the previous three targets.

4.3 Production and Characterization of Sputtered Materials

4.3.1 Preliminary Experiments

Preliminary experiments were conducted on substrates that were made from Al-foil. During these experiments, the results of the sputtered materials were observed. The first experiment was conducted with C5 (primary Co source), M3 (main Mn source) and A5 (primary Ni source) targets which were the main targets without the fourth alloying elements. The first sputtering experiment's XRD results may be seen in figure 4.6.

The green colour on the graph represents Al peaks, and red represents amorphous bump.

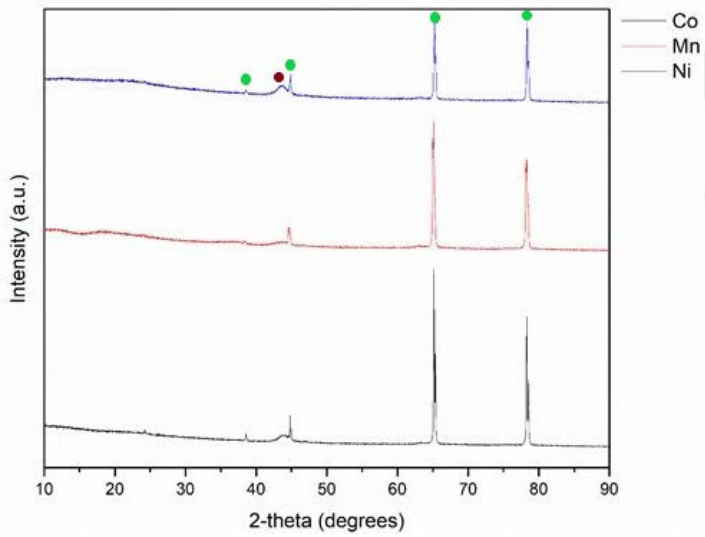

Figure 4.6 XRD characterization results from preliminary experiments

In figure 4.6, Co, Mn and Ni data indicated in the graph were named according to the proximity of the samples to the targets, which were the source of the elements. There were four distinct peaks and one bump on the XRD result of figure 4.6. The four peaks in the graph belong to the aluminium element in the aluminium foil, which

was used as the substrate. It may be seen that there was a result similar to an amorphous material peak around 44° in all three results in the graph. It was determined that the products obtained after the sputtering experiment did not have any crystalline structure but had an amorphous structure since there were no other peaks other than aluminium peaks and amorphous peaks.

After this preliminary experiment, it was decided to continue the work with 21 circular substrates with 18mm in diameter. These substrates were placed on the substrate holder. For a more transparent understanding, figure, 4.7 may be examined below.

Figure 4.7 21 Ni substrates lined up on the substrate tray

Sputtering experiments was carried out by cutting nickel foils with a diameter of 18mm and then arranging them on a triangle-shaped experiment base with 21 bases. In this experiment, the problem of spalling samples close to the targets was encountered due to the power applied to the generators and the increasedlocal temperature. This problem was solved by preparing weights on each sample and placing it. The reason for choosing nickel as the sample base was that the materials deposited on the Al-foil substrate in previous studies were amorphous. Since this

situation may reveal a heat treatment requirement before possible electrochemical characterization in the following stages, the use of aluminium foil has been abandoned in order to avoid a possible loss of time and repetition of the experiment. Instead, it was decided to use nickel foil, which was resistant to higher temperatures and is used as a current collector in cathode materials. Also, the problem discussed in chapter 2 that Fragnaud et al. [64] observed will also be avoided by using Ni substrates instead of Al.

4.3.2 First Set of Experiments

After the preliminary experiments, the first set of experiments were conducted on the RF Sputter Magnetron with three 2-inch targets on the 21 nickel foil substrates. The experimental summary parameters may be seen below in table 4.11.

Table 4.11 Sputter parameters of the first set of experiments

Exp. No	Target	Material	Gas Flow Rate (sscm)	Chamber P. (mTorr)	Sputter Power (Watt)	Time (h)
1	T1 T2 T3	A5 C4 M3	Ar:18	5	100 60 100	10
2	T1 T2 T3	A5 C4 M3	Ar:18	5	100 60 100	10
3	T1 T2 T3	A5 C4 M3	Ar:18	5	100 60 60	10

There were three experiments in the first set. Two of them were conducted on Ni-foil substrates, as may be seen on the above table, and the remaining one (experiment

number 2) was conducted on glass substrates to measure the thickness values since the thickness sensor inside of the magnetron sputter was out of service.

The details of EDS analysis and the deposition mass calculations of these three experiments may be examined in the appendices section.

The average film mass of the four experiments which were conducted on the Ni-foil may be seen in table 4.12

Table 4.12 Average film mass

Exp. No	Deposition Mass (mg)
1	2.28
3	2.06

The two experiments have relatively close mass. 3rd experiment's average deposition mass is lower than the 1st experiment. This was due to the reduction of the sputtering power of the second target. This decision will be discussed in this section.

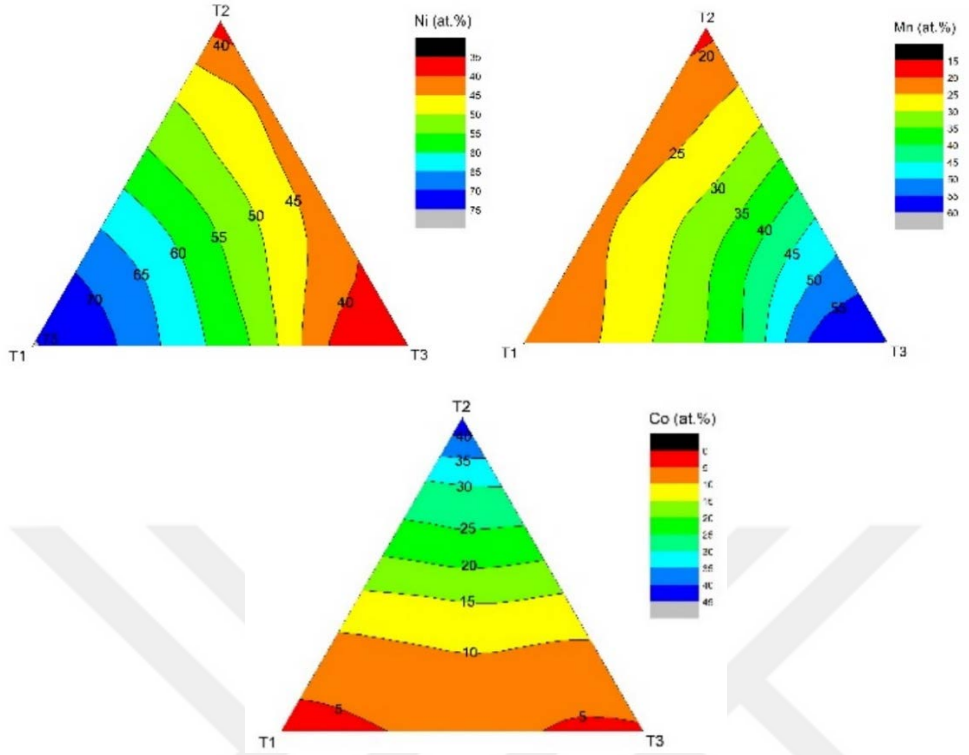

Figure 4.8 Elemental distribution map of experiment 1

It was observed that the manganese element ratio in the samples was higher than desired. There was also a 20% nickel element in the M3 target, which was used as a manganese source, and this element dramatically increased the nickel ratio in the samples. Due to this situation, the power of the M3 target in the T3 position was decided to be decreased to 60W to the same power as the C4 cobalt source element in the T2 position. Due to the presence of nickel and manganese elements in the A5 coded element in the T1 position, a power reduction of 40 watts would help the ratio of the manganese element to stay in the desired levels reduction of the nickel element will be prevented.

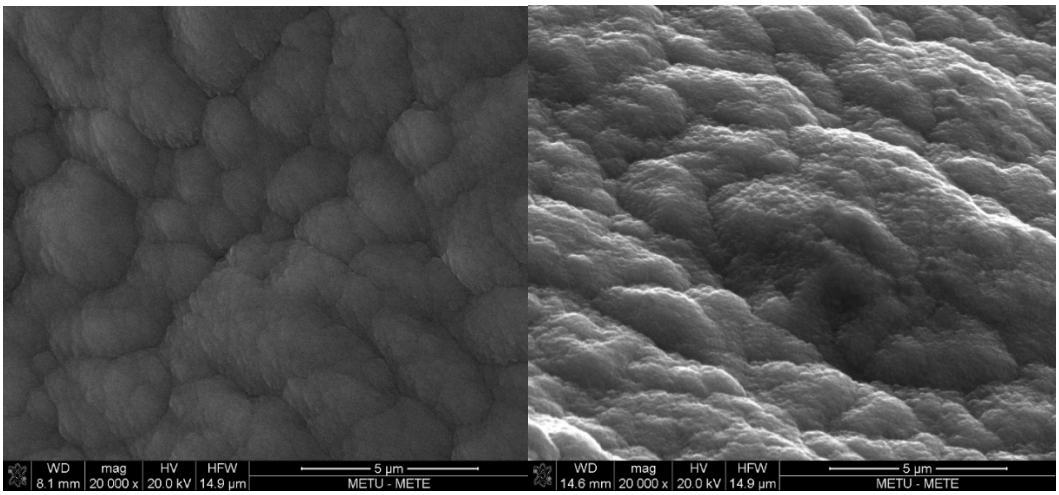

Figure 4.9 Sample 1 and sample 21’s SEM images

The high working distance in the SEM image of sample number 21 is due to the local high temperature spalling caused by the proximity of the sample to the M3 coded generator in the T3 position, which is a local 100W manganese source. This problem was solved in later experiments with a weight placed on each sample as well as another piece of weight placed on top of the tray. The SEM images in figure 4.8 suggest the samples' lack of morphology.

In experiment two, which was conducted on a glass substrate, the aim was to obtain the thickness value and compare the elemental distribution with the prior experiment with the same deposition parameters.

EDS maps may be seen in figure 4.10 and thickness maps may be seen in figure 4.11.

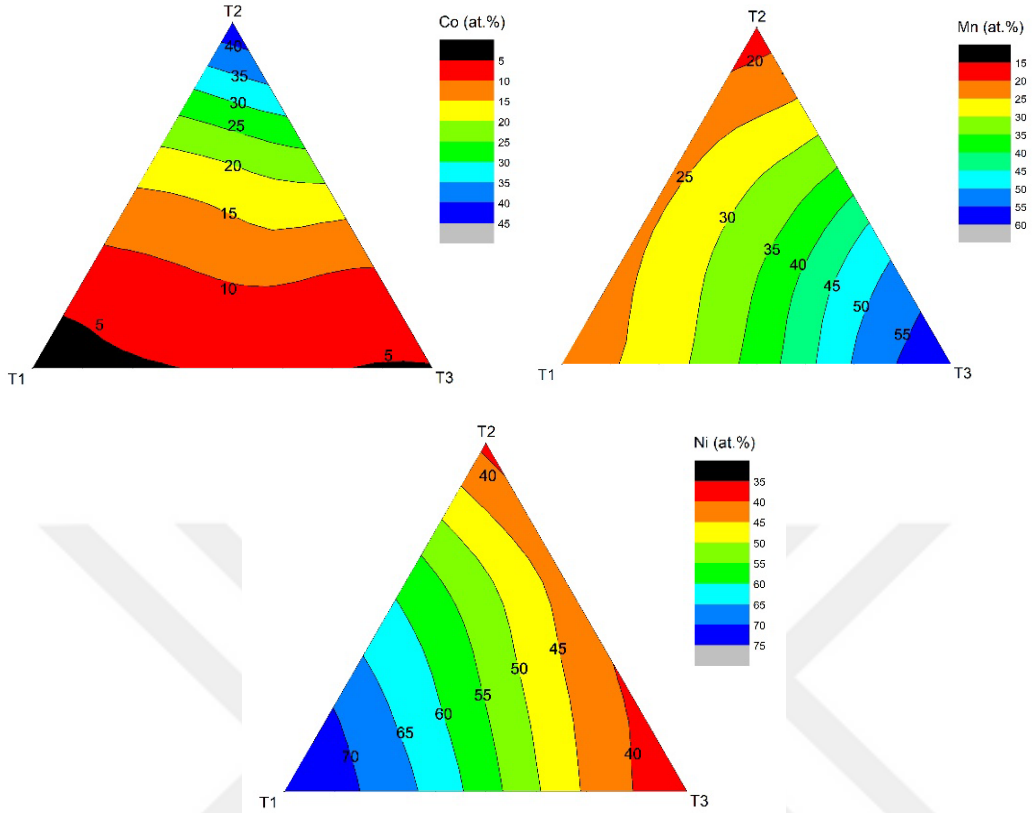

Figure 4.10 Elemental distribution map of experiment 2

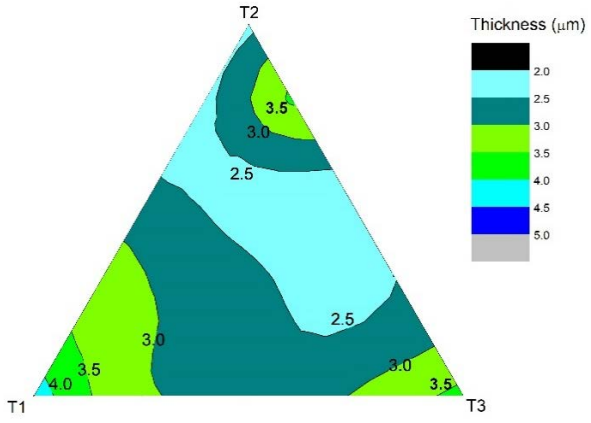

Figure 4.11 Thickness map of experiment 2

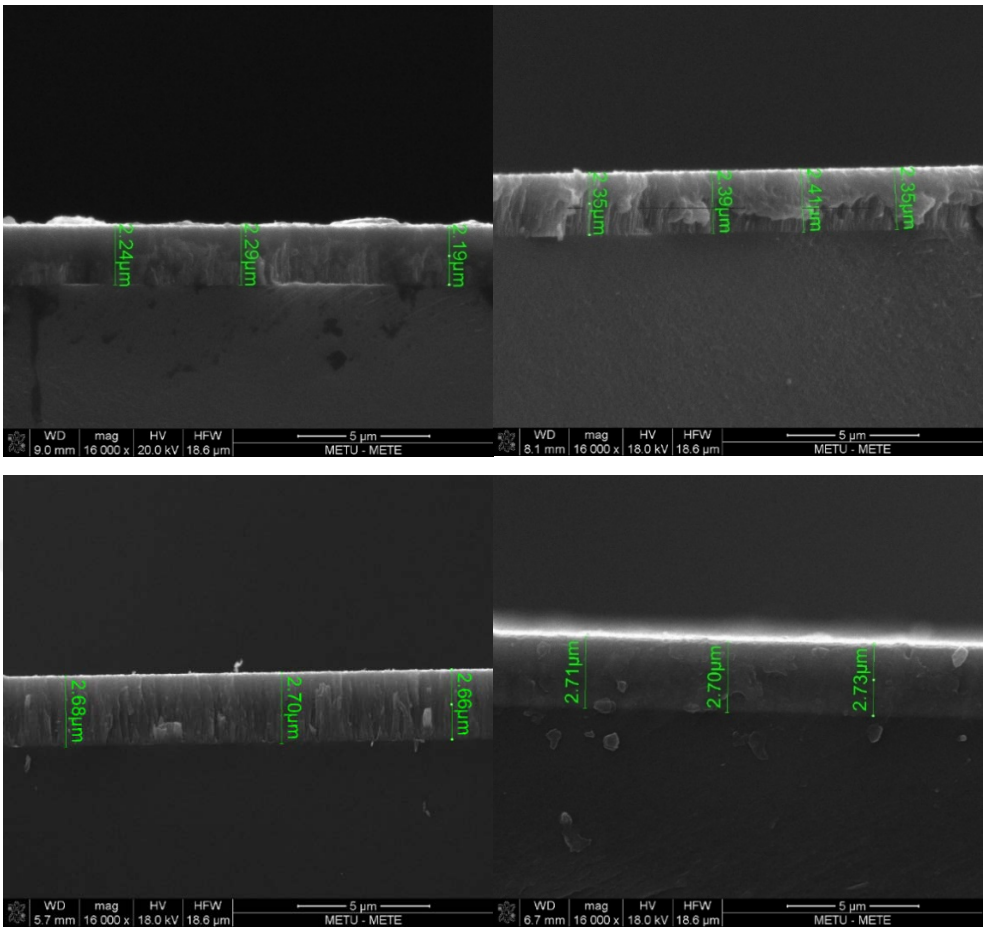

Figure 4.12 SEM photographs of coatings. Samples 2, 5 and 13, 19, respectively

When Figures 4.8 and 4.10 were interpreted together, the experiments with the same target powers gave long-lasting results. This is actual proof that the experiment is reproducible. This experiment used a glass substrate instead of the nickel foil substrate. The reason for using glass backing is to measure the coating thickness. After the sputtering experiment, the samples produced were broken, and the cross-sectional areas were prepared in accordance with the scanning electron microscope, and the thickness measurements were completed from more than one point for each sample. Examples of these images can be found in Figure 4.12.

The thickness distribution map in figure 4.11 was prepared with the average thickness values taken for each sample. The exact thickness values of this experiment may be examined in appendix c.

The manganese amount was found to be relatively more than desired so that the power of target 2, which was the primary manganese source in the system, was reduced from 100W to 60W, as shown in table 4.11.

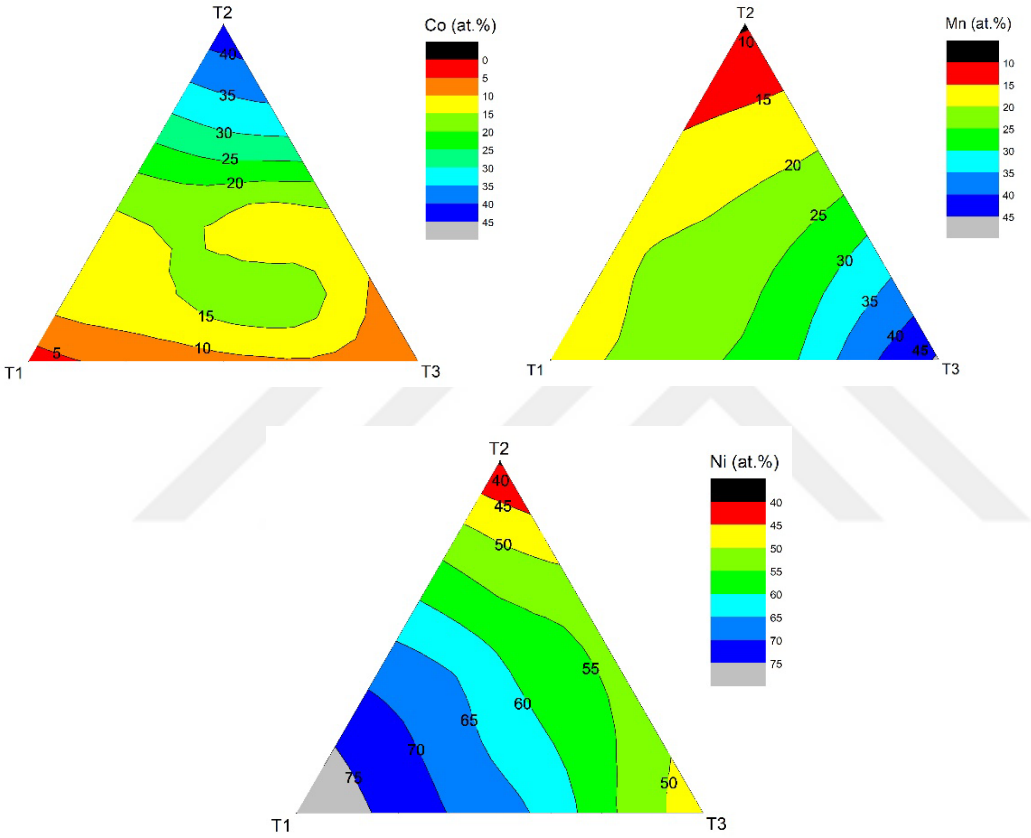

Figure 4.13 Elemental distribution map of experiment 3

After changing the power of the main manganese source target, the manganese ratio was reduced as desired. The elemental maps have changed compared to the first two experiments. Ni and Co percentages were increased throughout the map.

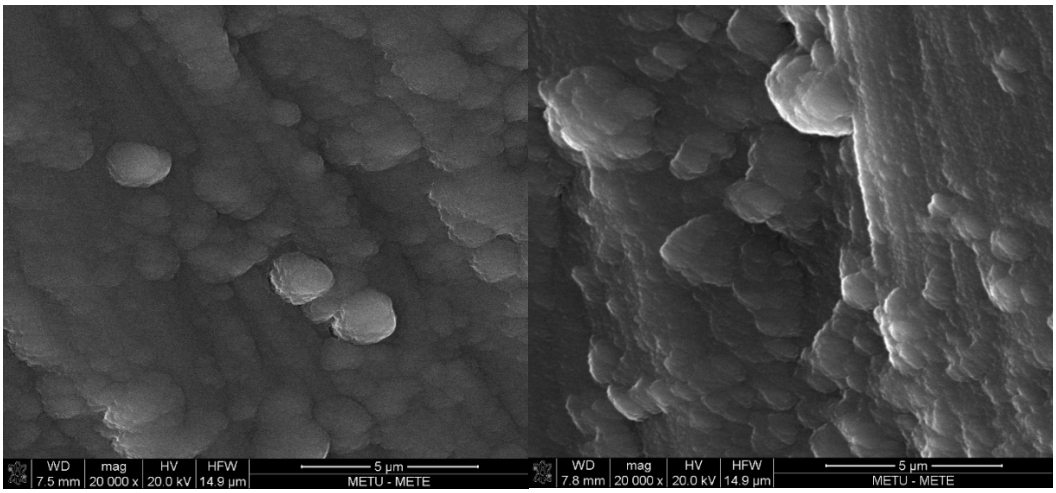

Figure 4.14 SEM images at of samples 1 and 21 of experiment 3

The images in figure 4.14 confirm the lack of morphology like the previous experiments.

After the sputter deposition experiments were optimized according to the elemental distribution, the substrate selection was completed, the experimental parameters were optimized, electrodes were produced for three different systems, the preliminary electrochemical characterizations were started.

In preliminary trials, a sample with a stoichiometry of 22.14% Co, 22.58%Mn and 55.29%Ni was selected on a nickel substrate. This sample was placed in the cell in the glove box immediately after the scattering-deposition experiment. Then, impedance (EIS), cyclic voltammetry (CV) and galvanostatic charge-discharge (GCD) characterizations were applied to this cell. In the first charge-discharge trial, it was observed that the material reached its sheer potential without showing sufficient capacity. Therefore, many cycles were performed with cyclic voltammetry with a wide voltage window, and the cathode material conditioning was attempted. The cycle was carried out in the range of 2.2 V to 4.9 V and at a rate of 90 mV/s. The behaviour of the first ten cycles is given in Figure 4.15. It was determined that

the behaviour did not change much in the following cycles. Then, the 200 cycle charge-discharge cycle was started. Here, the cut-off potentials are 2V and 4.8V. The charge-discharge current is about 0.4 mA/cm^2. Voltage profiles and cyclic discharge capacity values are given in Figures 4.16 and 4.17.

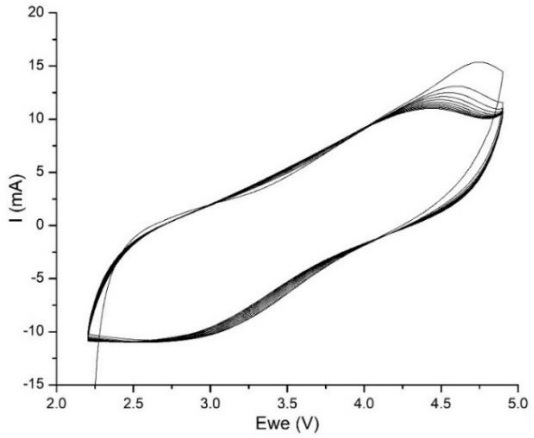

Figure 4.15 Galvanostatic charge discharge graph

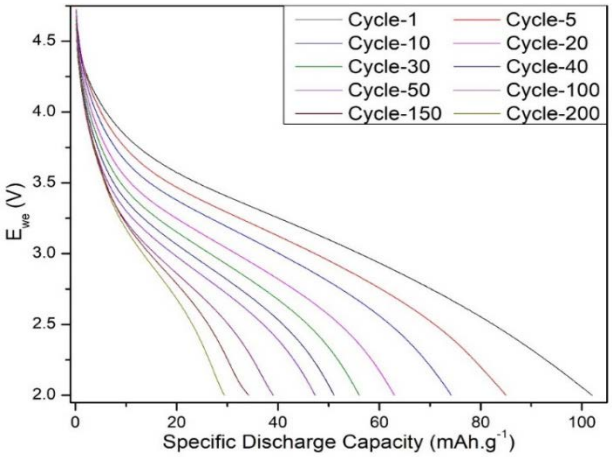

Figure 4.16 Charge-discharge voltage profiles

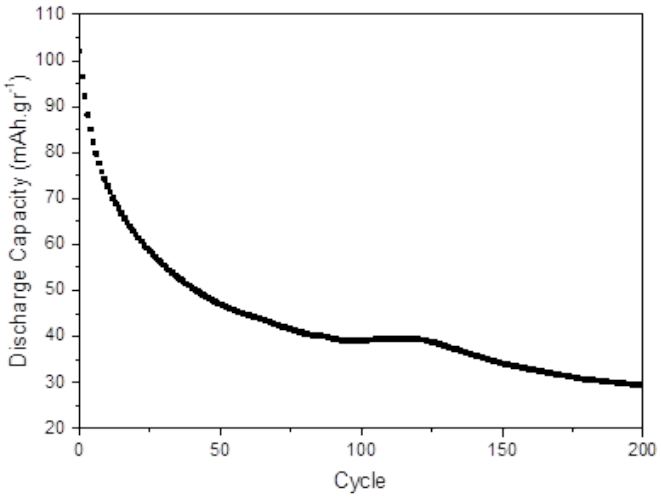

Figure 4.17 Cyclic discharge capacity

Looking at the GCD results from Figure 4.15, it was seen that the first discharge capacity is around 100 mAh/gr. However, decreasing capacity can be seen with increasing cycles. Considering the specific discharge capacity values, it was seen that the capacity decreased to around 40 mAh/g in the 100th cycle, and the capacity continued to decrease partially with the ongoing cycles. It is thought that the capacity values and behaviour according to the cycle may be related to the initial amorphous structure of the material. It can be said that especially lithium-ion diffusion is critical.

After these electrochemical results, it was thought that the capacitance could be improved by heat treatment of the electrodes obtained from the sputtering-deposition experiment. For this reason, it was decided to apply heat treatment at two different temperatures (750°C and 800°C).

To see the effect of these heat treatments on the crystal structure, first, XRD characterization was applied after the sputter-deposition experiments. Then heat treatment was applied to the samples at 15-minute intervals. This process was continued until the 60th minute, and the effects of time and temperature on crystallization were tried to be understood.

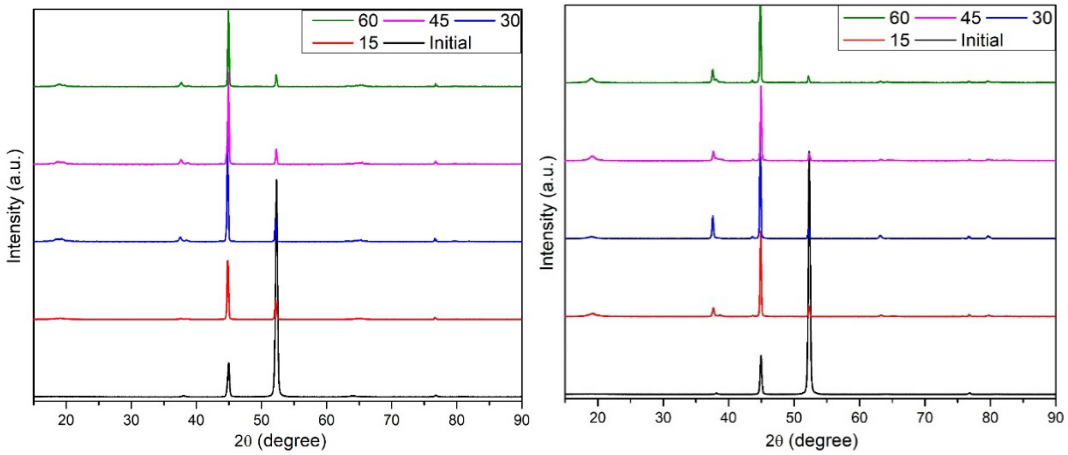

Figure 4.18 Heat treated XRD results. 750°C and 800°C, respectively

In the heat treatment optimization studies, two samples with the closest composition were selected from 21 electrodes produced by the sputtering-deposition method. Of these samples, the stoichiometry of 29.37% Co, 22.00%Mn and 48.63%Ni used for 750°C and 30.42% Co, 25.51%Mn and 44.06%Ni used for 800°C.

When the characterization results in figure 4.18 were interpreted, it was seen that new diffraction peaks appear as a result of crystallization as the heat treatment time increases for both temperatures. It has been observed that the structure goes from amorphous to crystalline. The results shown in black were the samples without heat treatment, and the peaks seen in these results belong to the crystalline metallic nickel in the nickel foil on which the sample was coated. It may be seen that as the time increases for both temperatures, new peaks begin to form, and these peaks become clear. When the theoretical diffraction peaks of the material expected to crystallize in the $R\bar{3}m$ space group were compared with the angular values of the measured peaks, harmony was observed. However, the intensities of the peaks were not in perfect harmony. This indicates that lithium may have been removed from the active material after heat treatment. One possibility is that the lithium may have migrated to the underlying nickel by diffusion. Especially at 800 °C, the solubility of lithium

in nickel increases. In addition, there was a visual deterioration in the samples after heat treatment. In any case, instead of post-heat treating the sputtered materials, a new set of experiments were made with the flow of O_2 gas inside the chamber to obtain better electrochemical results.

4.3.3 Second Set of Experiments

The second set of experiments was conducted under changing the atmosphere and chamber pressure parameters. The atmosphere parameters are changed from pure Ar with a flow rate of 20 sscm to Ar and O_2 mixture with 18 sscm and 6 sscm, respectively [63]. The pressure parameter is changed from 5 mTorr to 10 mTorr [70].

New parameters which were defined for the second set may be seen in below table 4.13.

Table 4.13 Parameters of sputter experiments

Exp. No	Target	Material	Gas Flow Rate (sscm)	Chamber P. (mTorr)	Sputter Power (Watt)	Time (h)
1	T1 T2 T3	A5 C4 A7	Ar:18 O_2:6	10	100 60 100	10
2	T1 T2 T3	A5 C5 A7	Ar:18 O_2:6	10	100 60 100	10
3	T1 T2 T3	A5 C6 A7	Ar:18 O_2:6	10	100 60 100	10
4	T1 T2 T3	A5 C6 A6	Ar:18 O_2:6	10	100 60 100	10
5	T1 T2 T3	A5 C5 A6	Ar:18 O_2:6	10	100 60 100	10
6	T1 T2 T3	A5 C4 A6	Ar:18 O_2:6	10	100 60 100	10

XRD characterization of the experiments was done for sample 14, which is almost in the middle of the sample triangle of each experiment. Results of the characterization may be seen in the below figure.

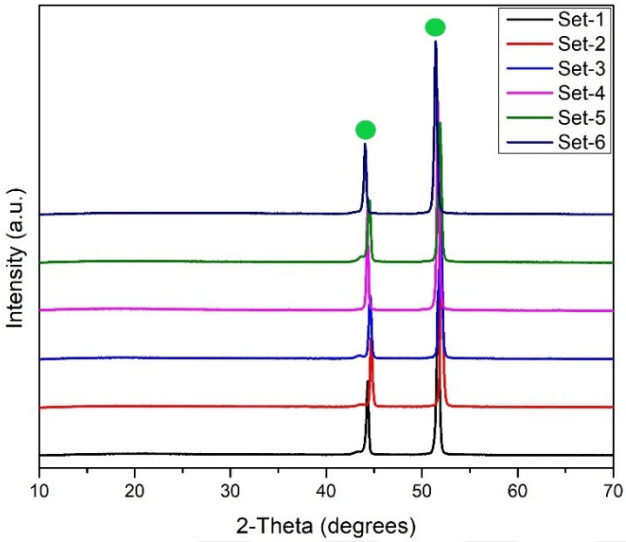

Figure 4.19 XRD characterization results of sample 14 of each experiment

The green dot represents the peaks of metallic nickel. This result means that the sputtered samples are amorphous like the prior set of experiments.

The elemental distribution, capacity, and energy maps of experiment 1 may be seen below.

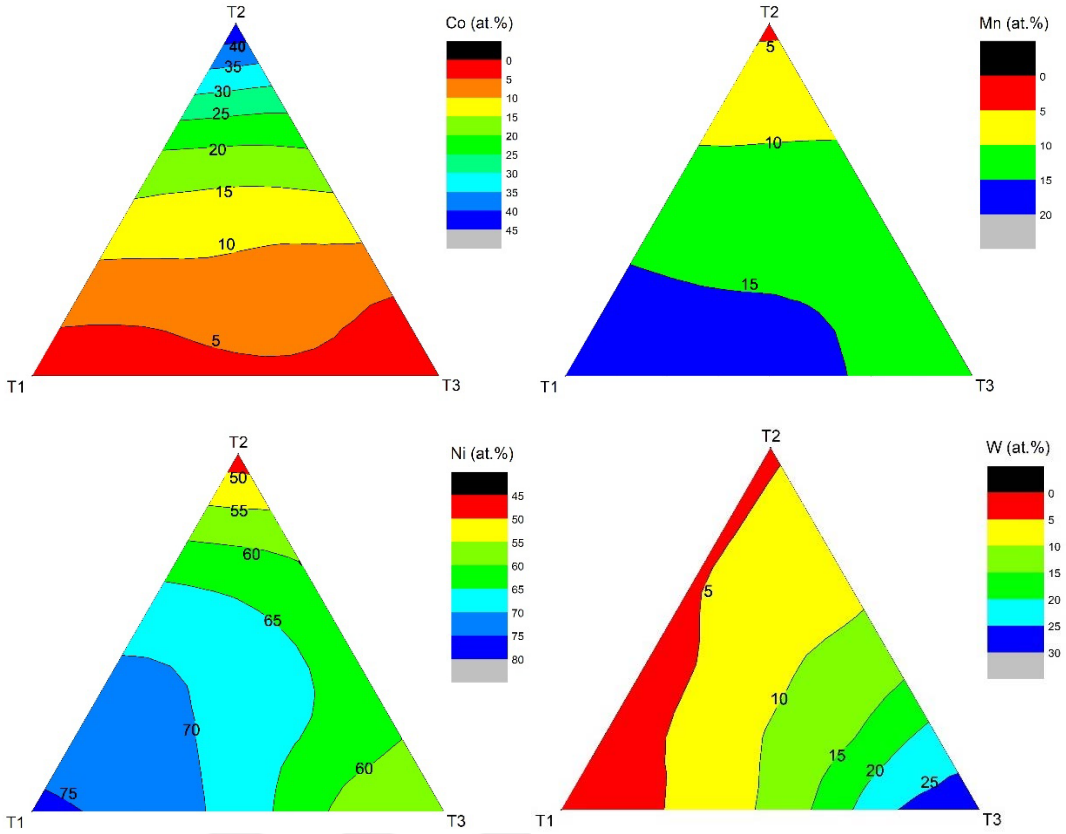

Figure 4.20 Elemental distribution map of experiment 1

The electrochemical characterizations of experiment 1 may be seen in the below figures.

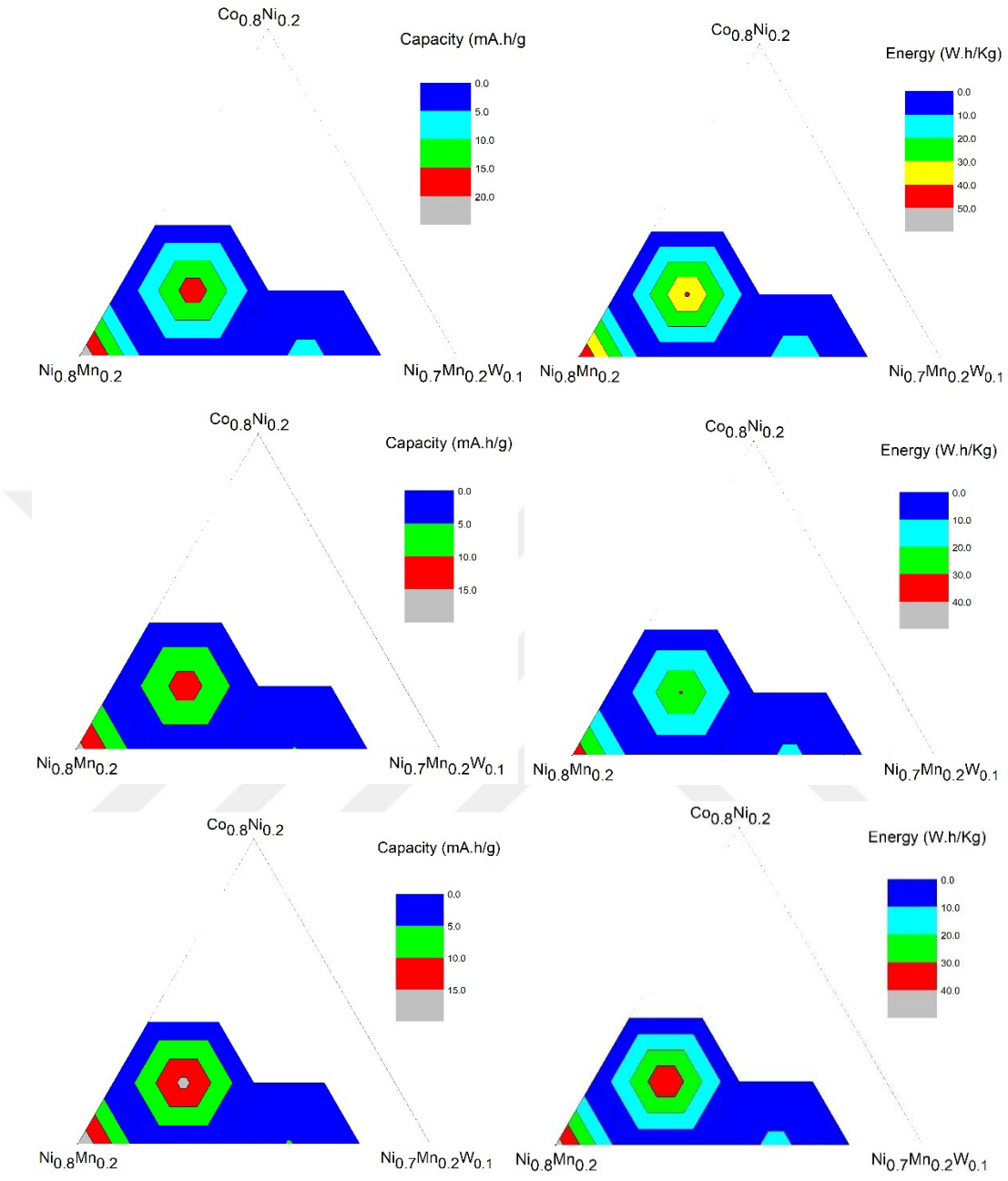

Figure 4.21 Discharge capacity and energy maps of cycle 1,2 and 3 of exp. 1

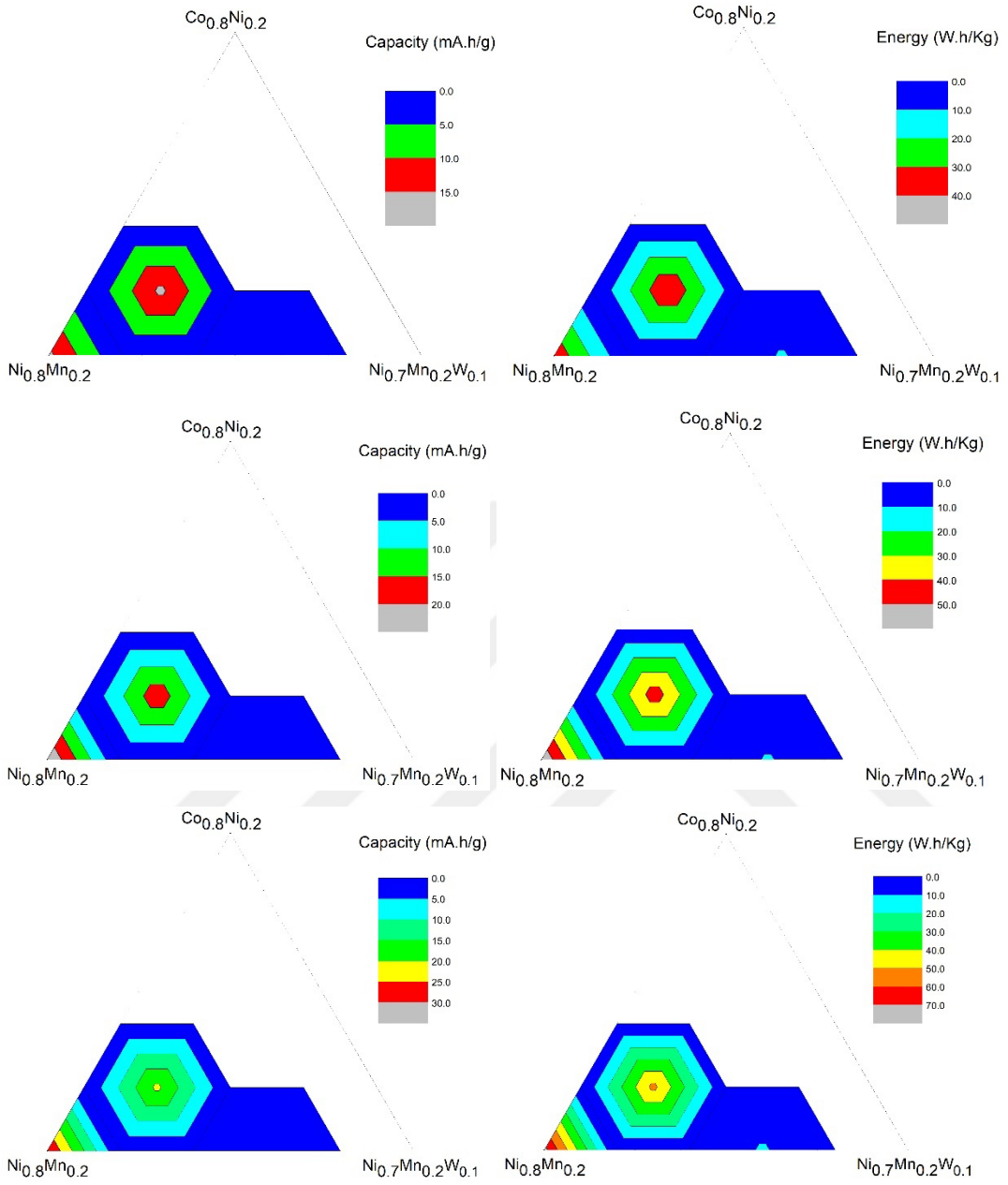

Figure 4.22 Discharge capacity and energy maps of cycle 4,5 and 6 of exp. 1

The results do not show promising values except for sample 6, which has the best result of 61.16 mA.h.g$^{-1,}$ which is a below-average result. Sample 6 also has the best

energy value among all the other samples. This may be because this set does not have any alloying elements except for W.

The elemental distribution, capacity, and energy maps of experiment 2 may be seen below.

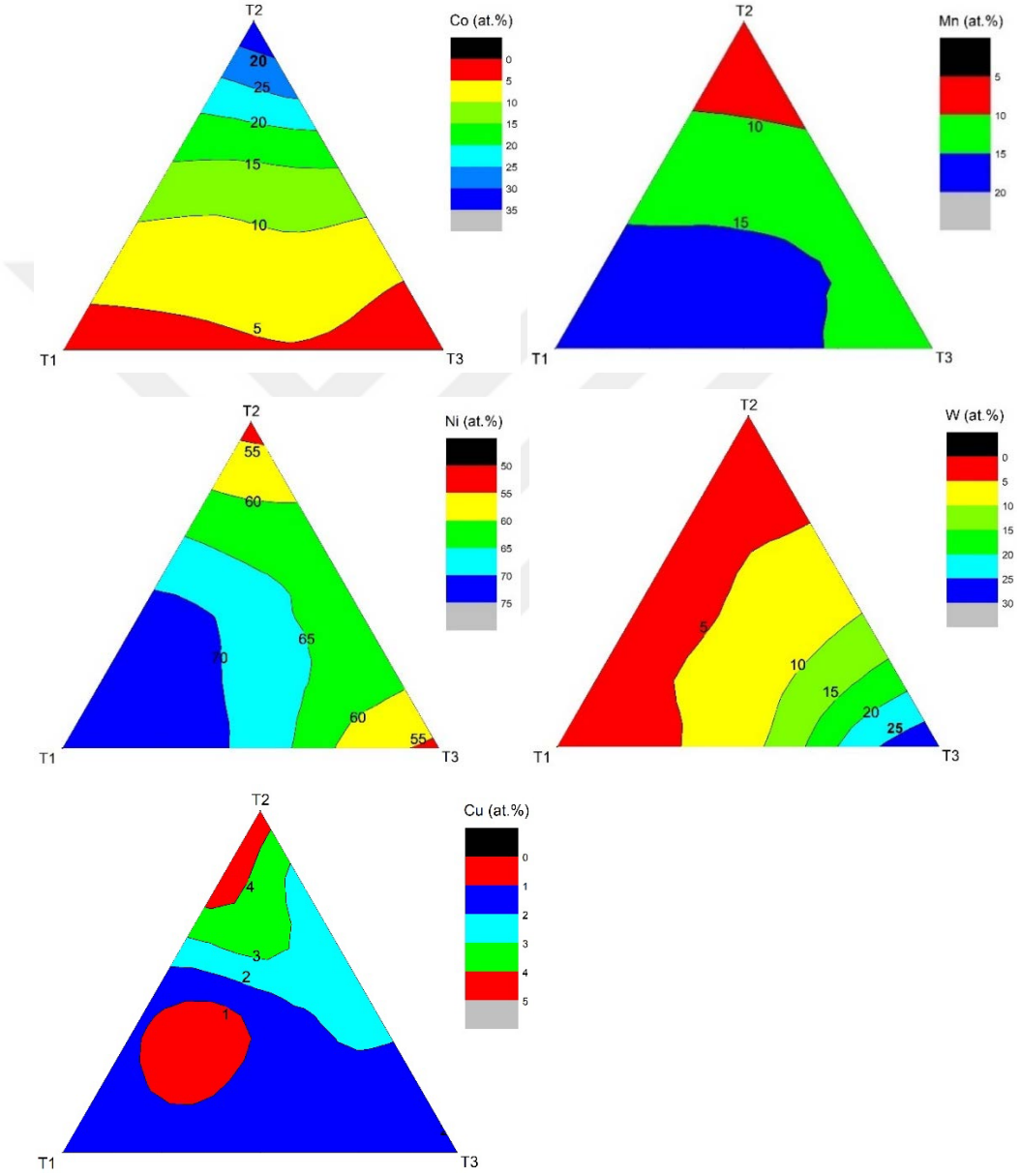

Figure 4.23 Elemental distribution map of experiment 2

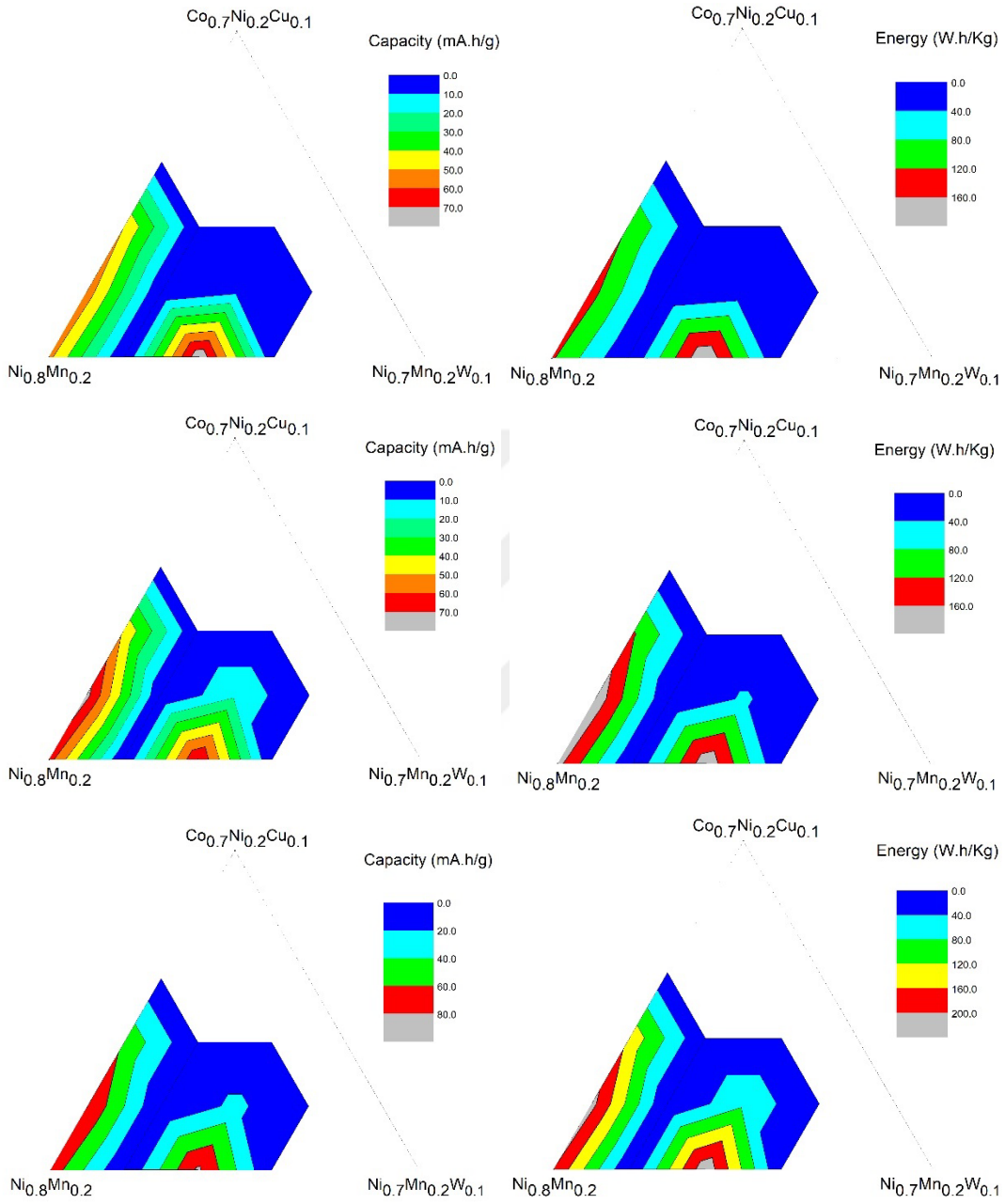

Figure 4.24 Discharge capacity and energy maps of cycle 1,2 and 3 of exp. 2

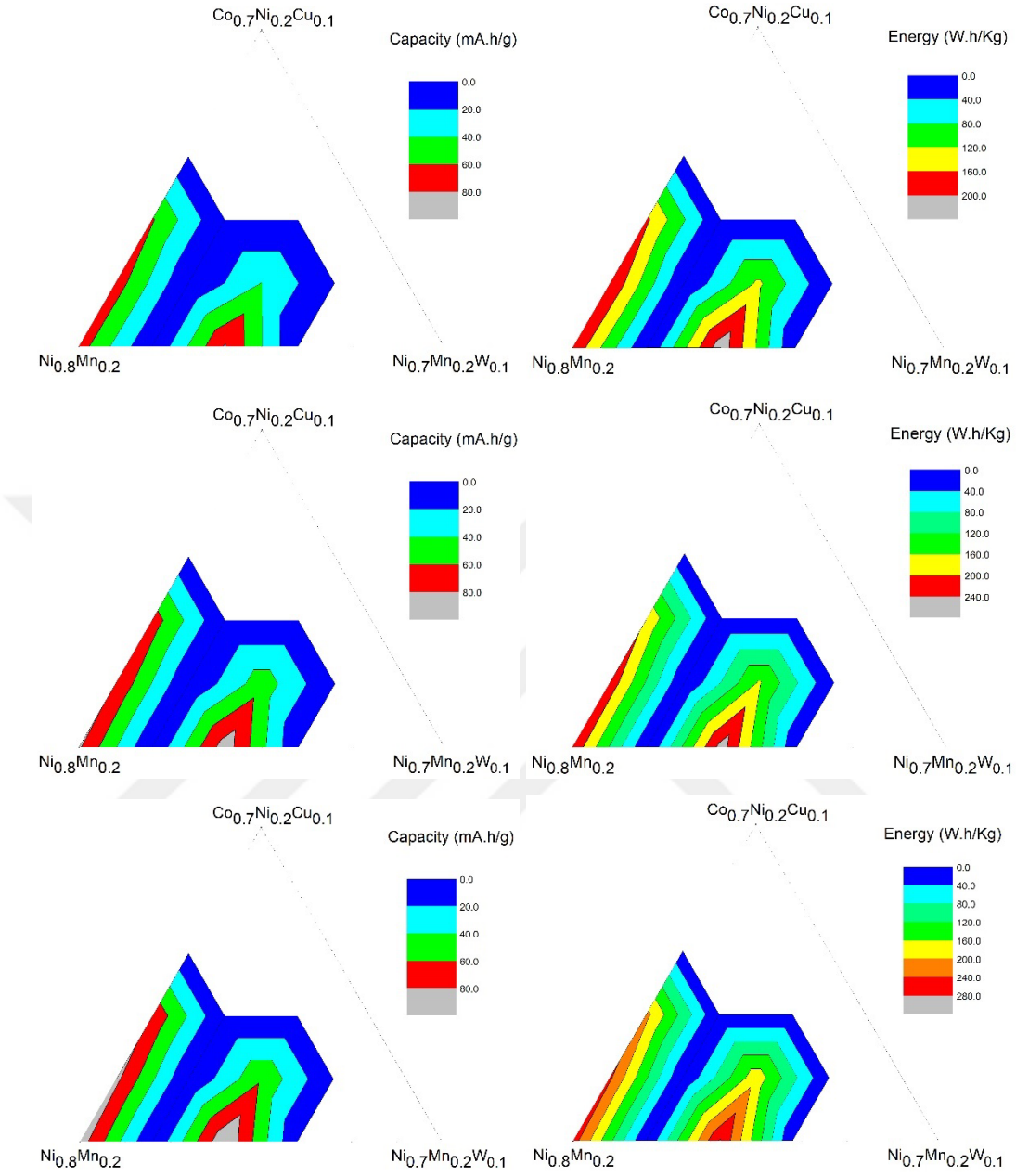

Figure 4.25 Discharge capacity and energy maps of cycle 4,5 and 6 of exp. 2

The results show that discharge capacity values are increasing slightly with the continued cycles. This may be due to the occupation of Li^{+} sites by Cu^{+2} ions, which

was also suggested by Yang et al. [51]. The best values are obtained at sample 18, which has more W content than the other samples.

The elemental distribution, capacity, and energy maps of experiment 3 may be seen below.

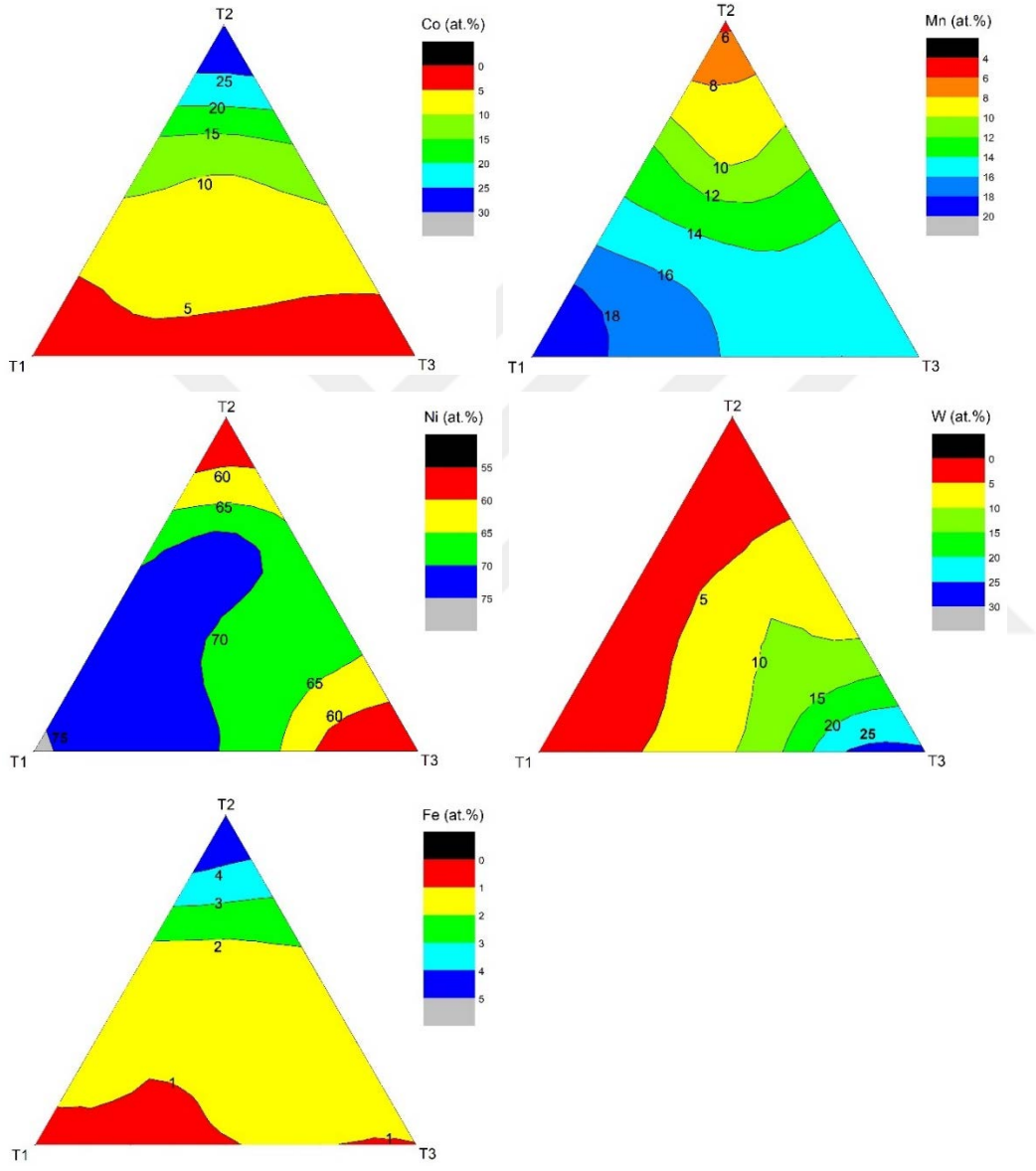

Figure 4.26 Elemental distribution map of experiment 3

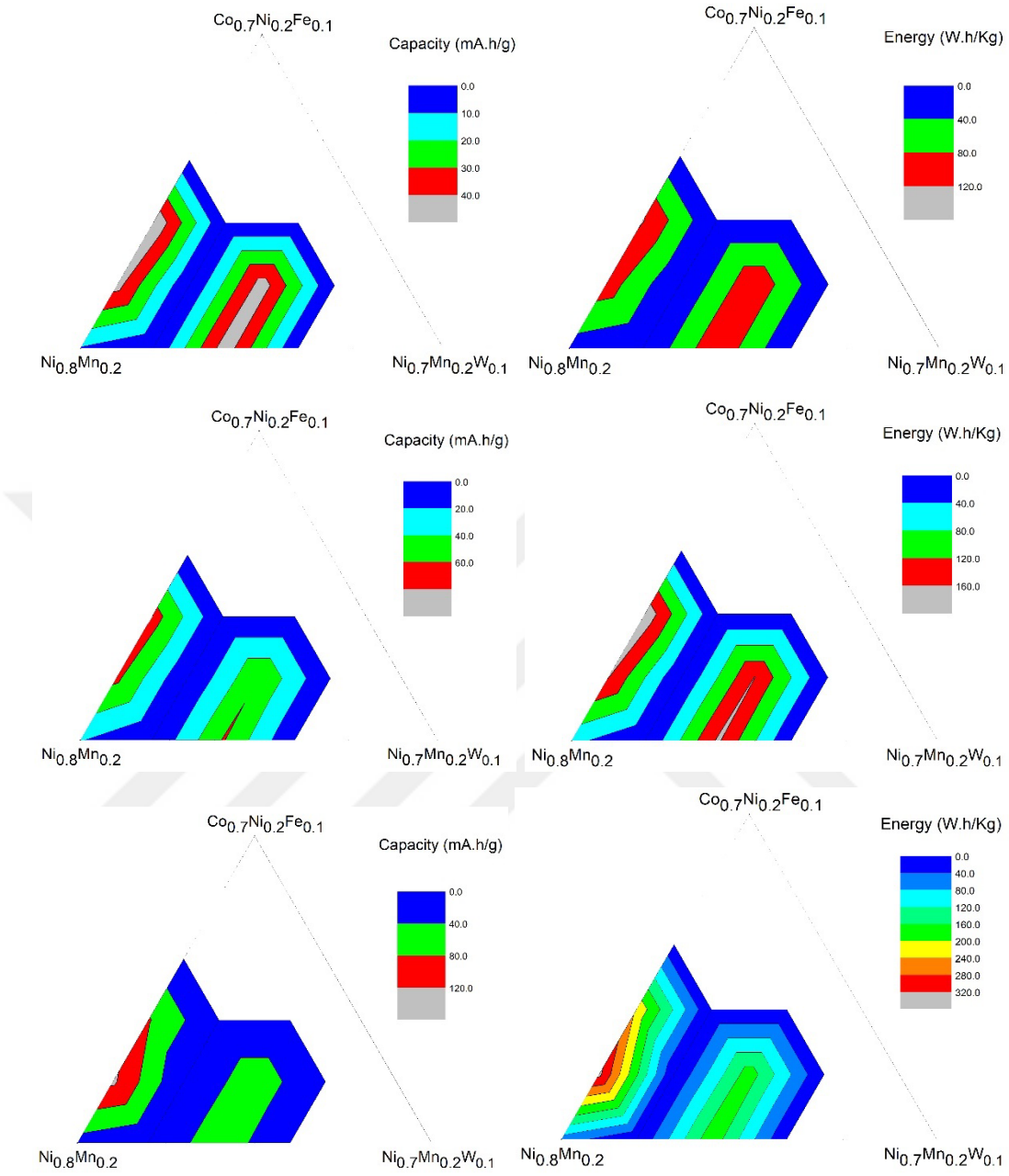

Figure 4.27 Discharge capacity and energy maps of cycle 1,2 and 3 of exp. 3

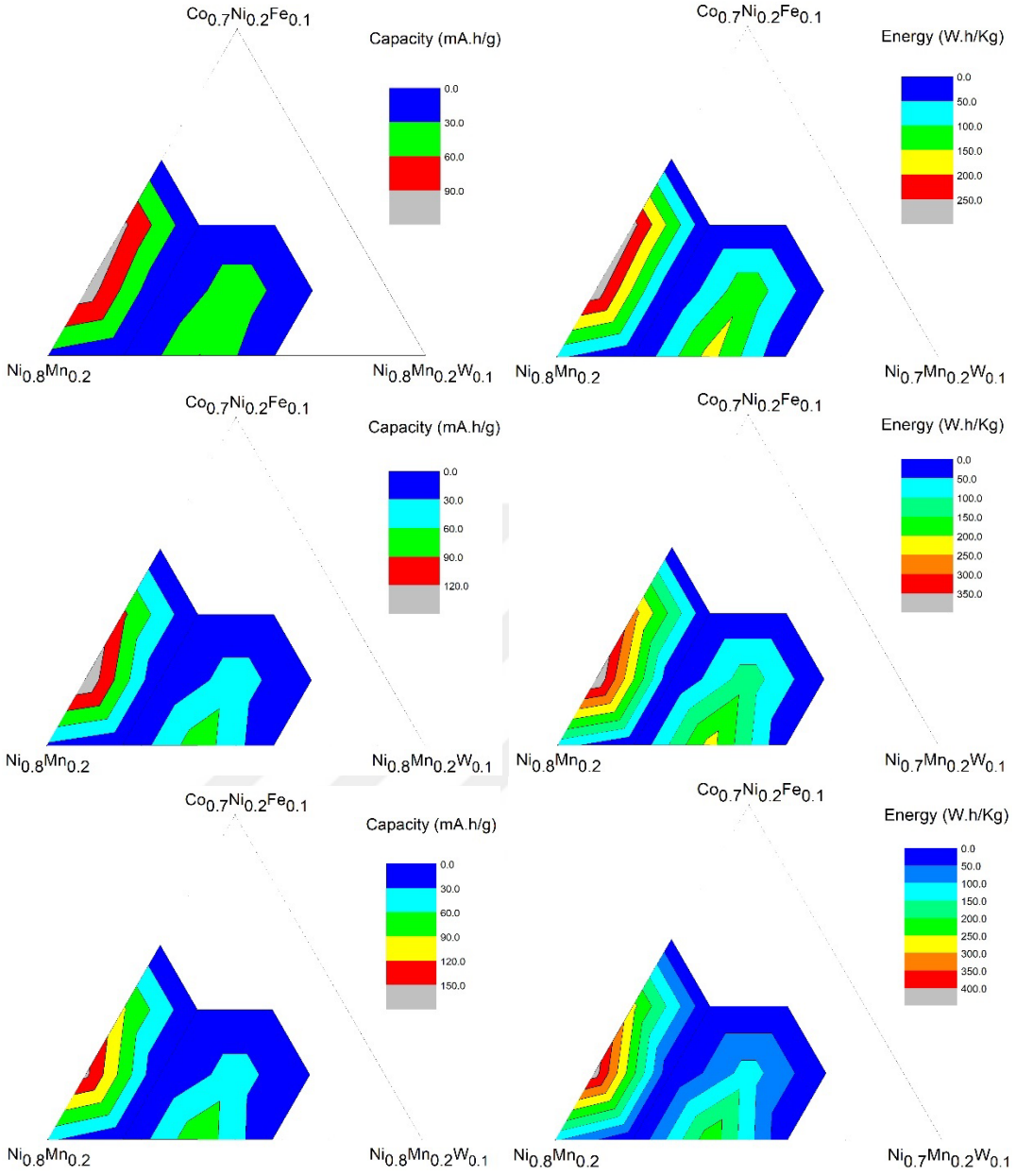

Figure 4.28 Discharge capacity and energy maps of cycle 4,5 and 6 of exp. 3

Samples 7 and 11 has the best performance among all the capacity results of experiment 3. This may be explained by having higher Ni content and having Co content more than 5%. Because sample 18, which has higher Ni content, has poorer performance than sample 7 and sample 11.

Sample 11 at cycle 6 shows the best discharge capacity and energy value among all samples in all six experiments with 157.40 $mAh.g^{-1}$ capacity value and 428.30 $Wh.kg^{-1}$ energy value. The distribution of Ni on the elemental distribution map is different from the other experiments, since 70% value is reached nearly on the top side of the graph, which may positively affect the capacity results. Also, W may have a positive effect on the discharge energy values.

The elemental distribution, capacity, and energy maps of experiment 4 may be seen below.

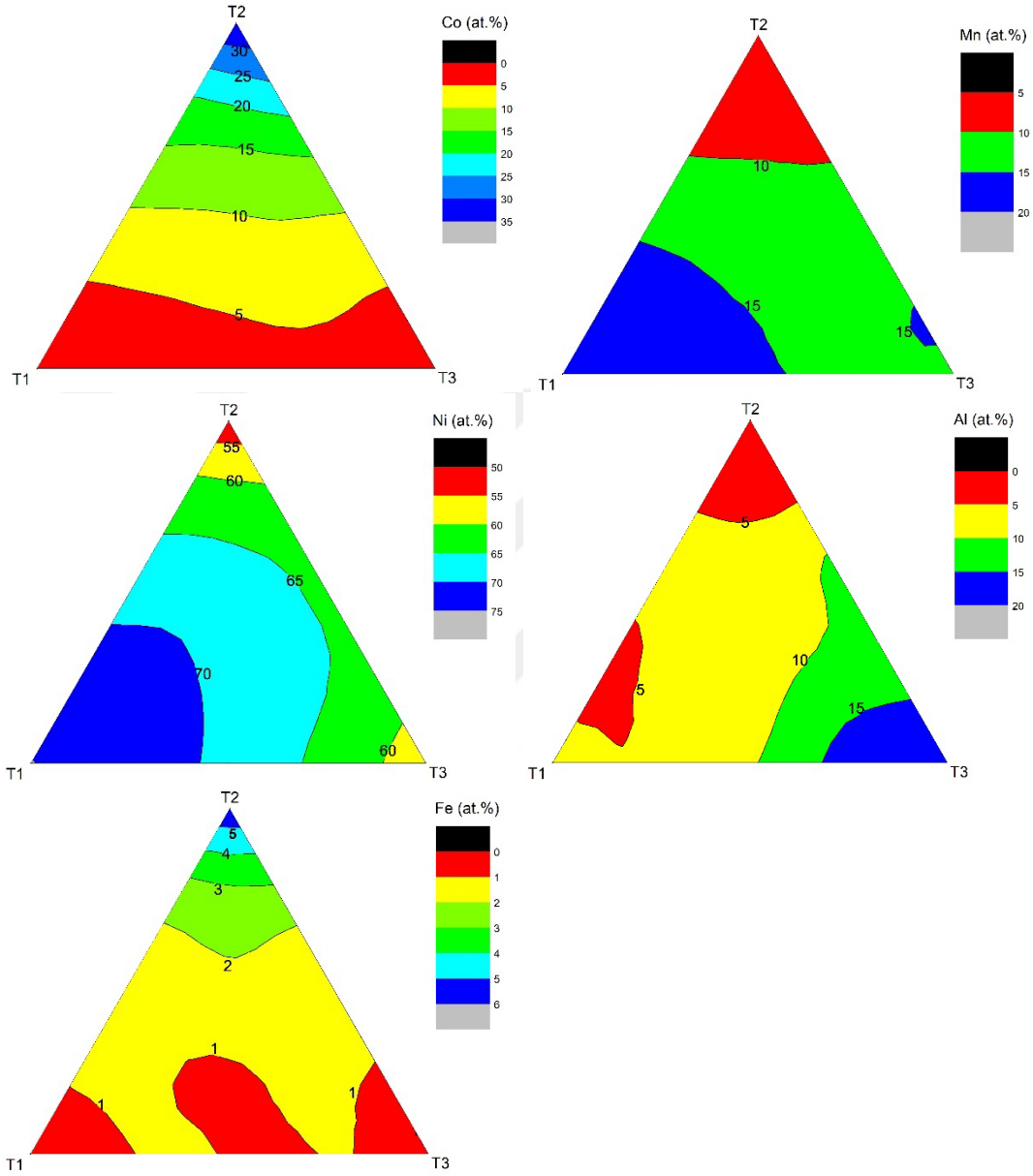

Figure 4.29 Elemental distribution map of experiment 4

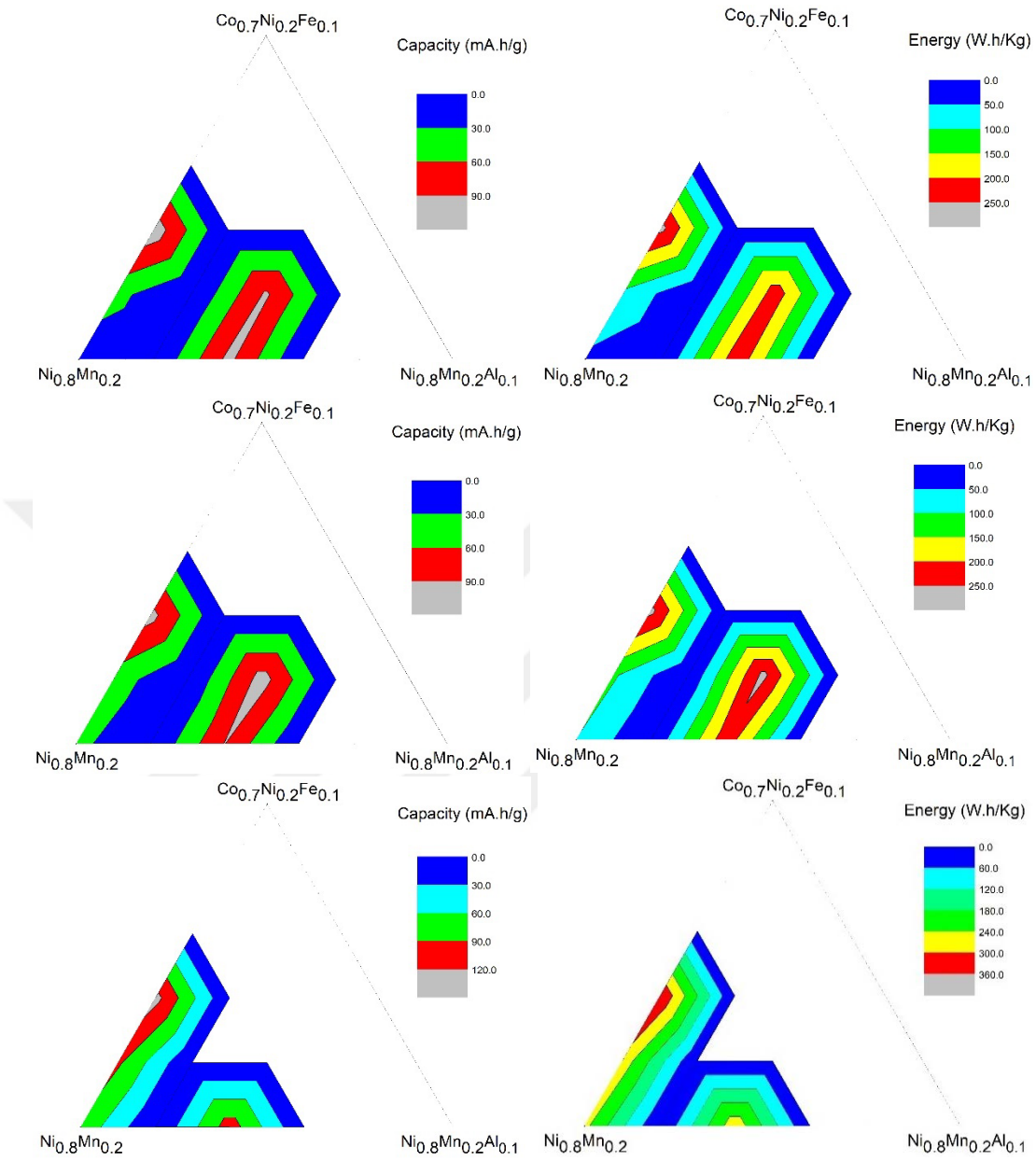

Figure 4.30 Discharge capacity and energy maps of cycle 1,2 and 3 of exp. 4

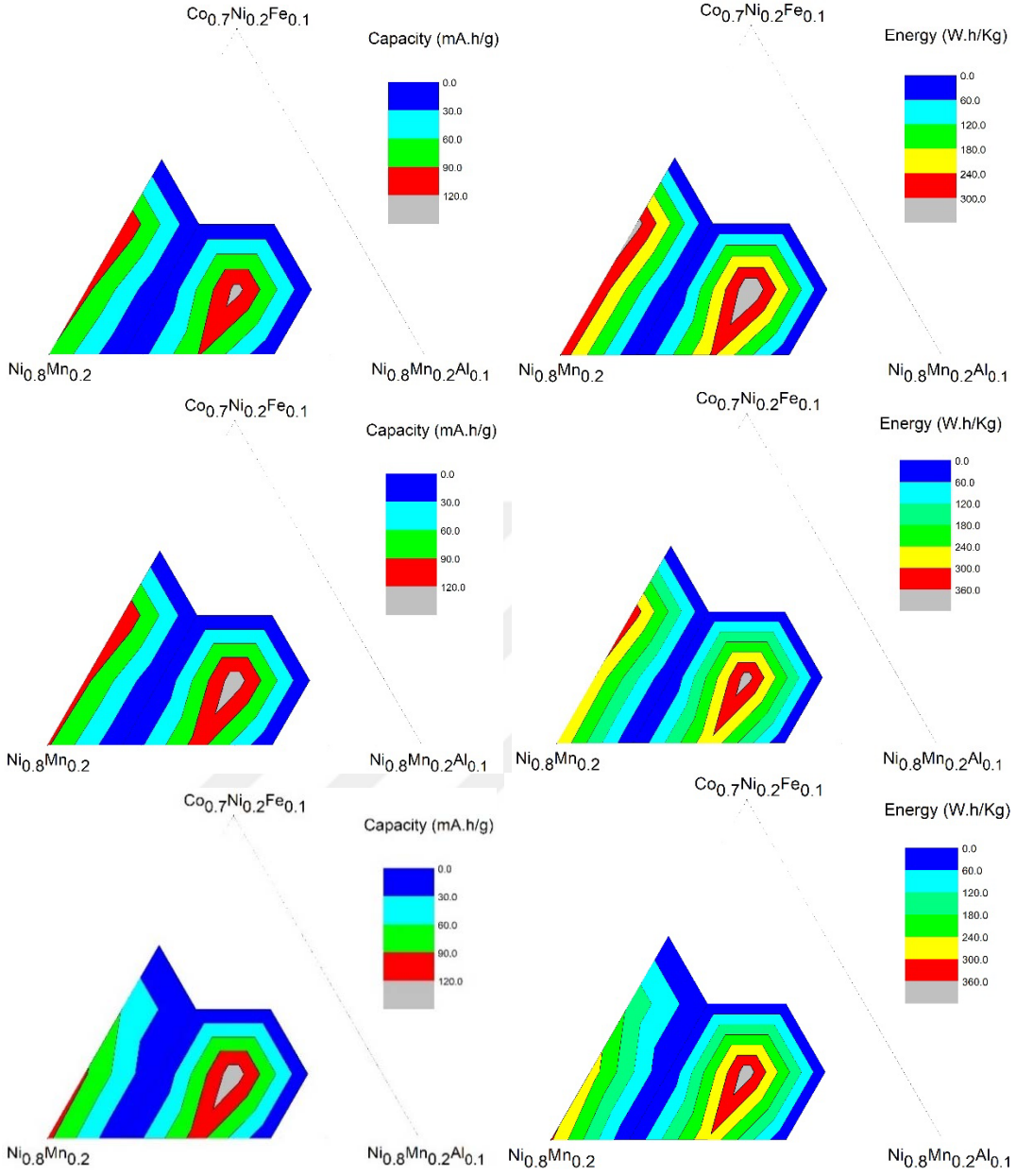

Figure 4.31 Discharge capacity and energy maps of cycle 4,5 and 6 of exp. 4

It may be said that the best results of discharge capacity and energy values are located on the concentration of 1-2% Fe regions. In these regions, as the Mn concentration increases, the energy and capacity values also increase.

The elemental distribution, capacity, and energy maps of experiment 5 may be seen below.

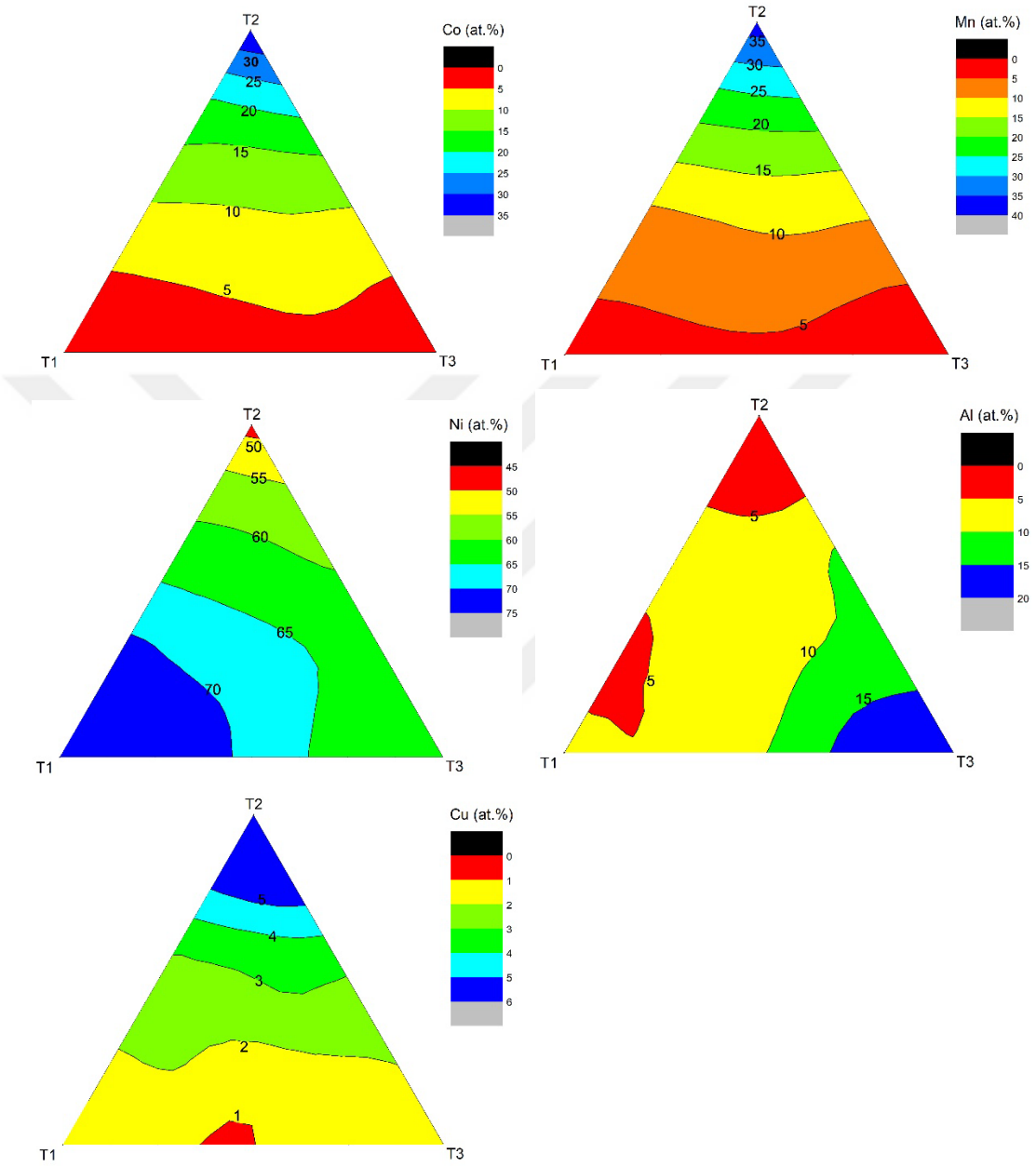

Figure 4.32 Elemental distribution map of experiment 5

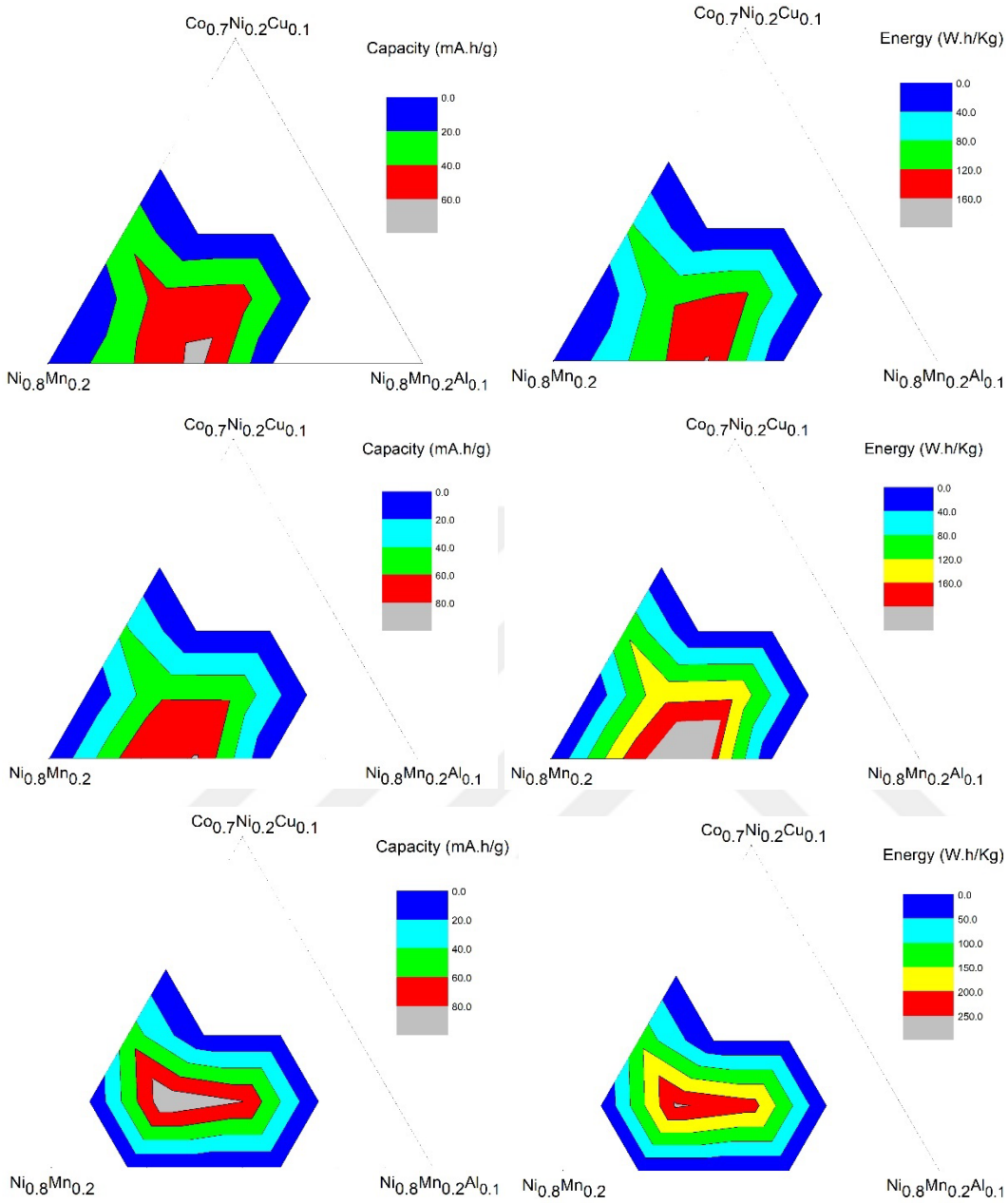

Figure 4.33 Discharge capacity and energy maps of cycle 1,2 and 3 of exp. 5

Sample 18 has failed after the second cycle. Also, sample 17's results cannot be read on the third cycle. These two errors produced different result maps compared to other experiments.

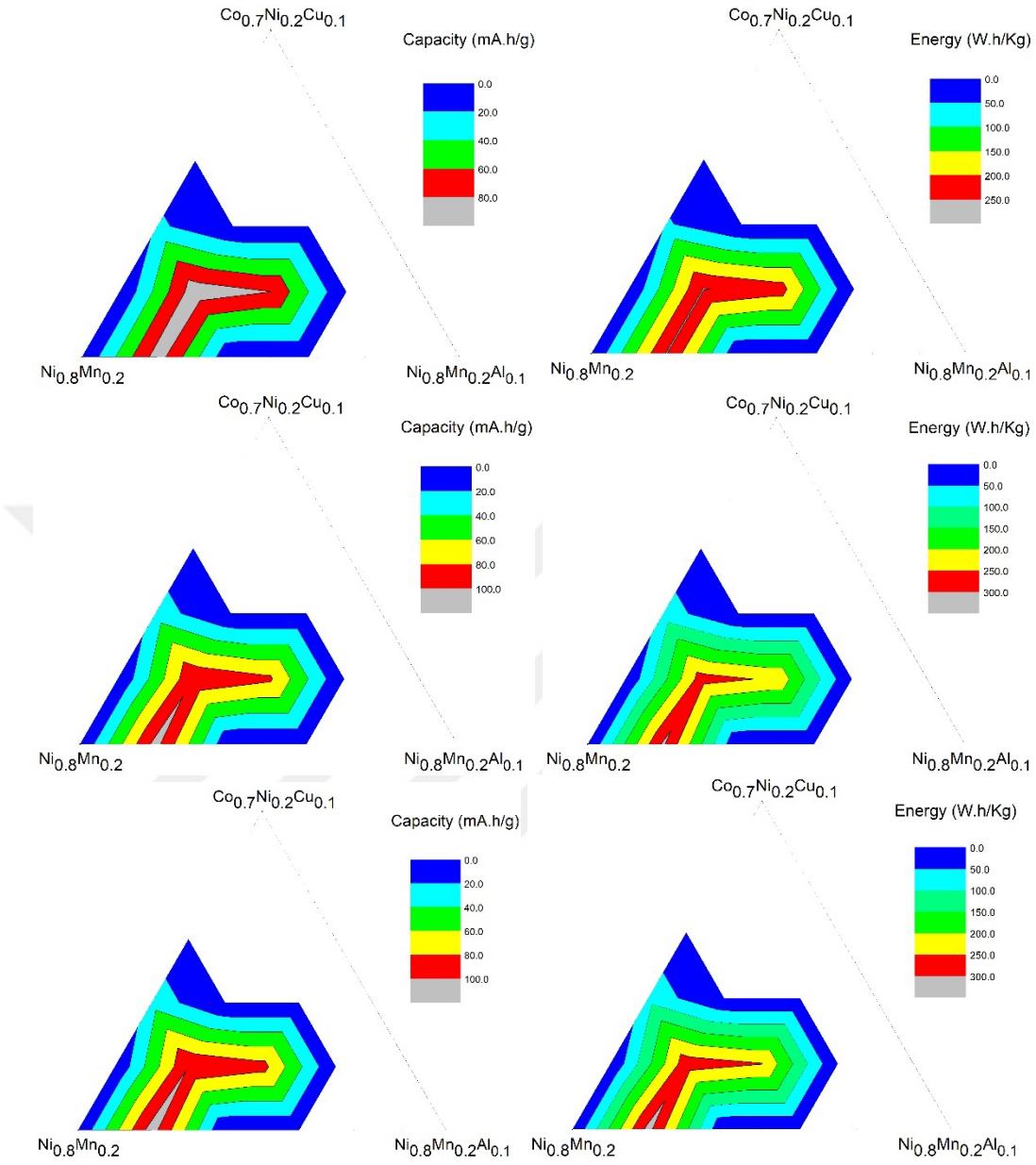

Figure 4.34 Discharge capacity and energy maps of cycle 4,5 and 6 of exp. 5

Discharge energy values are increasing as the cycle number increases. The highest discharge capacity and energy values are at the lowest Cu concentration areas as the Cu concentration increases, the values decrease.

The elemental distribution, capacity, and energy maps of experiment 6 may be seen below.

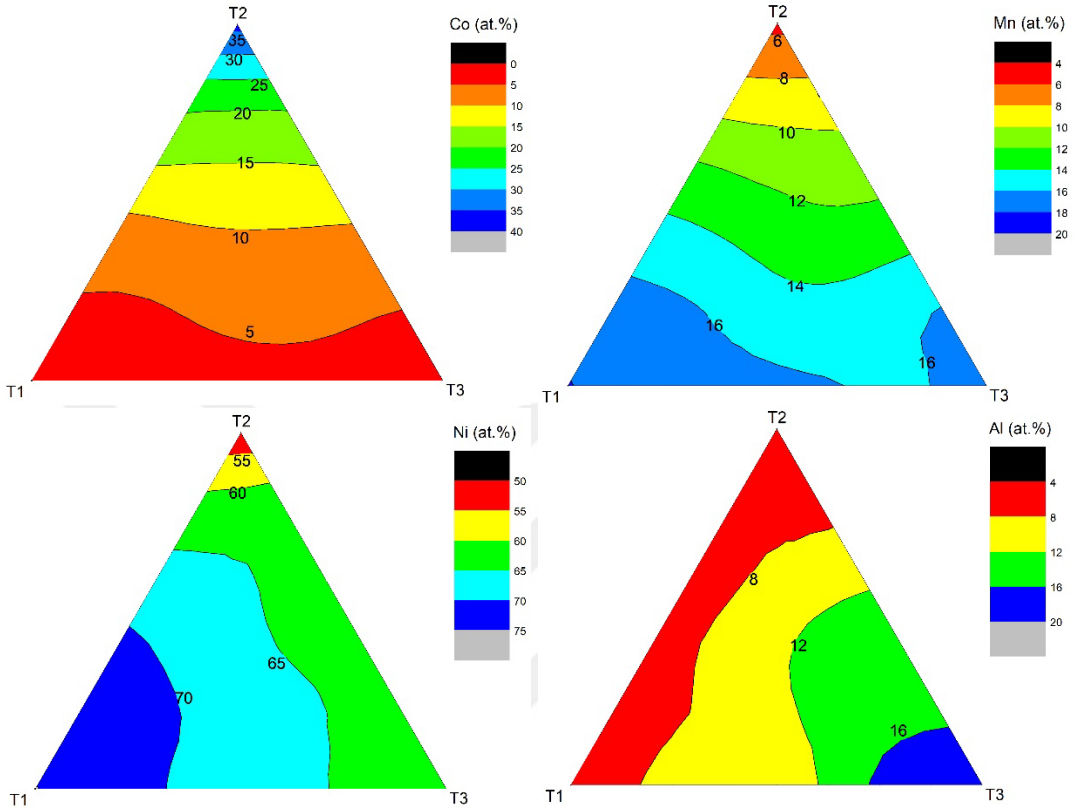

Figure 4.35 Elemental distribution map of experiment 6

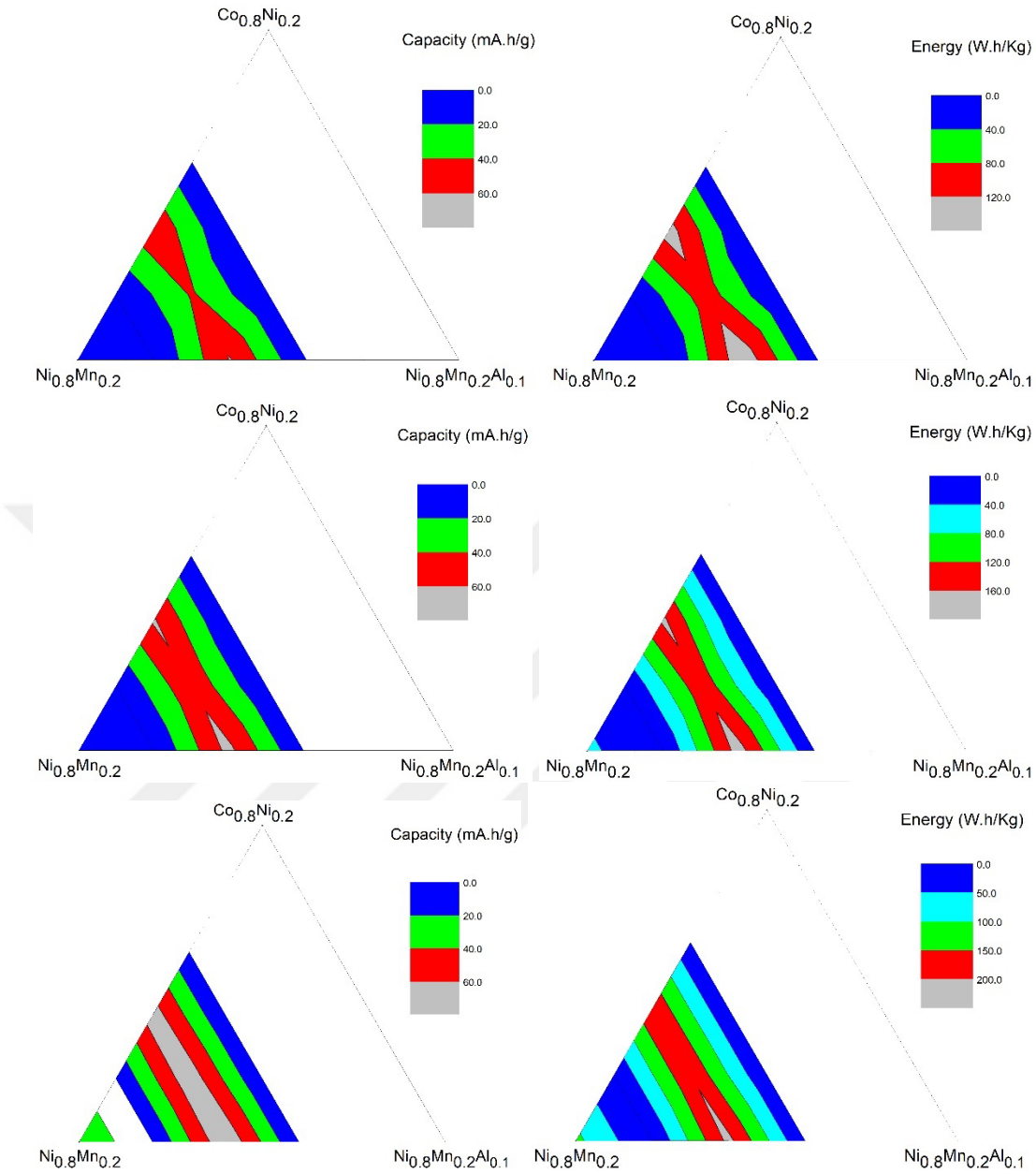

Figure 4.36 Discharge capacity and energy maps of cycle 1,2 and 3 of exp. 6

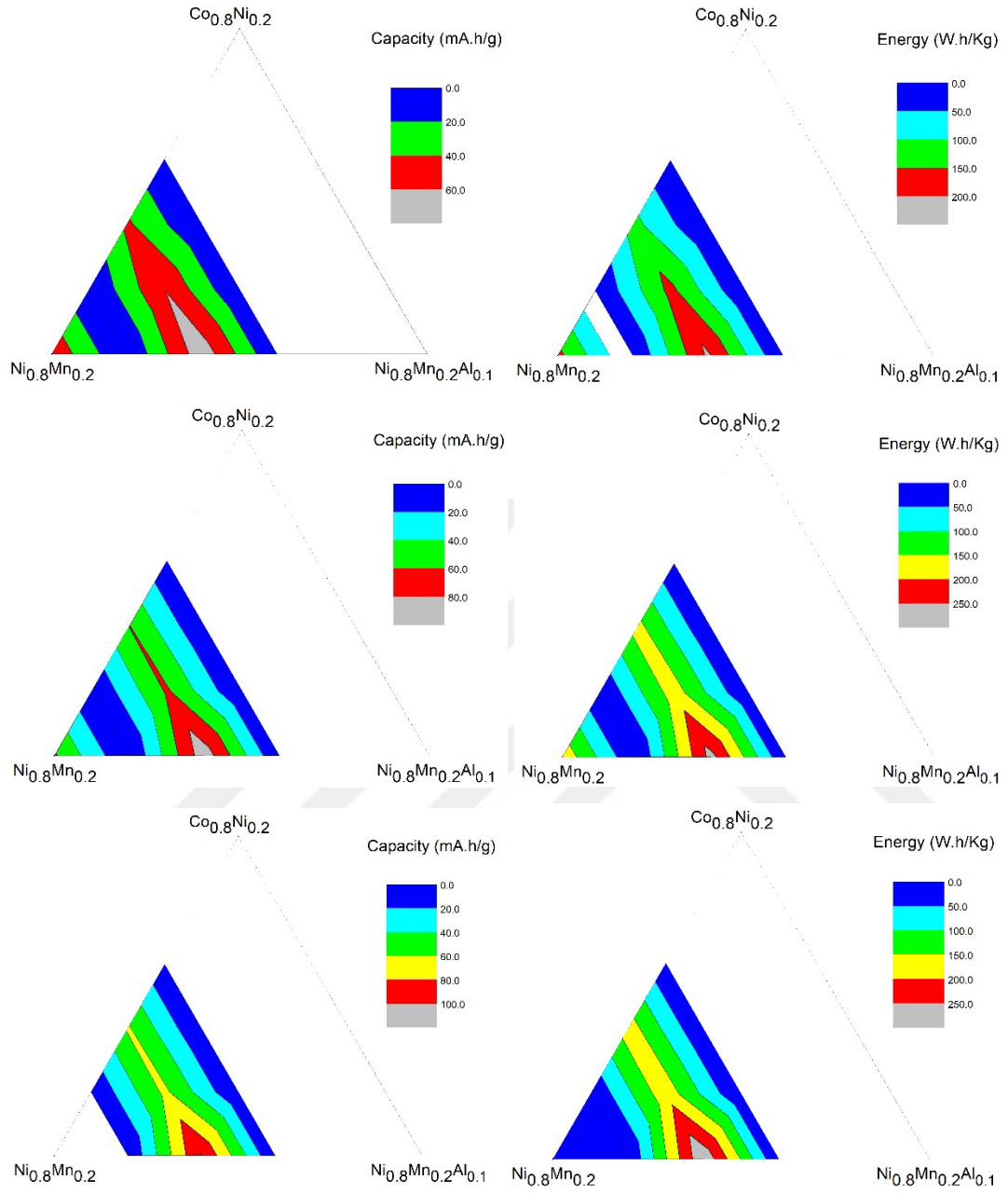

Figure 4.37 Discharge capacity and energy maps of cycle 4,5 and 6 of exp. 6

When the results of sample 16 and sample 18 are examined, it may be said that as the Al content increases, discharge capacity and the discharge energy values increases. Because the main elemental difference between sample 16 and sample 18

is the increased Al content in sample 18. This result may be seen on experiment six's discharge capacity and discharge energy maps. It may also be noted that sample 16 may suffer non-uniform deposition, resulting in a slight shape change of the substrate due to the increased local temperature during the sputter deposition.

Each electrochemical characterization was also conducted for sample number 3 of each experiment. This sample was the closest to the cobalt source (Target number 2). Therefore, the characterization of these samples should be made separately.

The exp-2 has the best discharge capacity and discharge energy values among all the other experiments. The best values were recorded on the sixth cycle of exp-2, and a continuous improvement during the cycling may also be observed. It should be noted that exp-2 has the lowest mass values among all the samples. Experiments 3 and 4 have improved discharge capacity values and discharge energy values. Experiments 1, 5, and 6 have a very low discharge capacity and low discharge energy values.

Table 4.14 Electrochemical characterization results of sample 3 of all six experiments

Exp No	Current (mA)	Cycle No	Capacity (mA.h/g)	Energy (W.h/Kg)
1	20	1	43.32	107.35
		2	33.29	85.51
		3	33.69	89.22
	40	4	29.21	78.58
		5	32.80	89.21
		6	34.28	93.73
2	20	1	87.53	209.06
		2	82.27	215.67
		3	93.12	248.96

Table 4.14. (continued)

Exp No	Current (mA)	Cycle No	Capacity (mA.h/g)	Energy (W.h/Kg)
2	40	4	87.53	235.13
		5	109.29	296.41
		6	109.82	306.53
3	20	1	46.69	113.55
		2	75.29	206.62
		3	75.09	208.74
	40	4	54.28	148.85
		5	56.49	152.12
		6	53.24	146.28
4	20	1	62.18	158.05
		2	83.66	226.18
		3	93.17	257.47
	40	4	82.94	229.76
		5	80.97	230.04
		6	92.69	262.79
5	20	1	34.20	82.97
		2	42.99	113.35
		3	48.99	131.84
	40	4	44.05	120.26
		5	43.91	121.11
		6	42.65	118.00
6	20	1	39.70	100.85
		2	40.90	109.22
		3	41.23	109.88
	40	4	24.09	63.68
		5	23.15	60.92
		6	22.71	59.64

Exp-1 and exp-6 should be evaluated together since the fundamental difference between these samples is that exp-1 has W whereas exp-6 has Al inside. The EDS results are 27.93% Co, 7.83% Mn, 57.17%Ni, 7.07% W for exp-1 and 21.32% Co,

8.89%Mn, 63.55%Ni, 6.24%Al for exp-6. Exp-6 has a lower capacity than exp-1, which does not support the EDS results due to the high nickel content of exp-6. However, exp-6 has a mass of 30% more than exp-1, which may explain the low-capacity result. Exp-1 has higher capacity retention than exp-6, which may be explained by the high amount of cobalt in the sample of exp-1.

Experiments 1,2,3, which have tungsten, as an alloying element, has more discharge energy density than experiments 4,5,6 which has Al as an alloying element supported by Kim et al. [49].

When the results of exp-3 and exp-4 are compared, it may be seen that exp-4 has better values. EDS results cannot explain this because they are very similar, except that exp-4 has W and Fe, whereas exp-4 has Al and Fe as alloying elements. Also, the sample of exp-4 is heavier (1.55 mg) than exp-3 (1.3 mg). It may be said that Al has improved the electrochemical performance, supported by the works of Wang et al. and Zhang et al. [46], [47].

There are two promising results. These are sample eleven of experiment three and sample thirteen of experiment four. Sample eleven has the best result of 157.40 $mAh.g^{-1}$ and 428 $Wh.Kg^{-1}$ and sample thirteen has the best result of 139.64 $mAh.g^{-1}$ and 397.09 $Wh.Kg^{-1}$. The elemental compositions of these samples may be seen on Table 4.15 and Table 4.16.

Table 4.15 Elemental distribution of sample 11

Exp - Sample no	Co (%at)	Mn (%at)	Ni (%at)	W (%at)	Fe (%at)
3 – 11	3.75	18.48	73.73	2.83	1.22

Table 4.16 Elemental distribution of sample 13

Exp - Sample no	Co (%at)	Mn (%at)	Ni (%at)	Al (%at)	Fe (%at)
4 – 13	5.3	14.98	68.71	10.36	0.65

CHAPTER 5

SUMMARY AND CONCLUSION

5.1 Conclusion

- Lithium transition metal oxide powders, which have different stoichiometries, were produced by Pechini sol-gel method, calcined, and then characterized.
- Metal and deformable PTFE molds were used to produce pellets out of powders. These pellets were first used in the sintering tests to determine the best sintering procedure for each material.
- After optimising the sintering processes, 2-inch sputter targets were produced for seven different stoichiometries.
- These sputter targets were used in the preliminary deposition experiments conducted by the magnetron sputtering device.
- With these preliminary experiments, sputter targets were used to conduct deposition experiments.
- The electrochemical characterization results of the six experiments were examined to understand the effects of the deposition and the elemental distribution.
- The electrochemical characterization results of sample number three of each experiment were examined to understand the effect of high Co content.

5.2 Recommendations for Future Work

- The amount of lithium inside the targets may be increased to improve the deposited cathodes' electrochemical results.
- The amount of nickel inside the targets may be increased to improve the produced materials' capacity results.
- Instead of producing a high Co content target, another high Ni content target with Co addition may be used in the sputter experiments to increase the capacities of the samples.
- Cathodes after sputter deposition may be annealed at a specific temperature to crystallise the samples.
- Extended cycling tests may be done on the materials to understand the cyclic performance of the cathode materials.
- Electrochemical tests may be conducted on various temperatures to understand the effect of temperature on the materials.

REFERENCES

[1] M. Winter and R. J. Brodd, “What are batteries, fuel cells, and supercapacitors?,” *Chem. Rev.*, vol. 104, no. 10, pp. 4245–4269, 2004, doi: 10.1021/cr020730k.

[2] M. Armand, “Nature Lithium Battery,” *Nature*, vol. 414, no. November, pp. 359–367, 2001, [Online]. Available: http://www.ncbi.nlm.nih.gov/pubmed/11713543.

[3] K. Nagaura, T. & Tozawa, “No Title,” *Prog. Batter. Sol. Cells*, vol. 9, p. 209, 1990.

[4] M. S. Islam and C. A. J. Fisher, “Lithium and sodium battery cathode materials: Computational insights into voltage, diffusion and nanostructural properties,” *Chem. Soc. Rev.*, vol. 43, no. 1, pp. 185–204, 2014, doi: 10.1039/c3cs60199d.

[5] W. Li, E. M. Erickson, and A. Manthiram, “High-nickel layered oxide cathodes for lithium-based automotive batteries,” *Nat. Energy*, vol. 5, no. 1, pp. 26–34, 2020, doi: 10.1038/s41560-019-0513-0.

[6] J. B. Goodenough, “Cathode materials: A personal perspective,” *J. Power Sources*, vol. 174, no. 2, pp. 996–1000, 2007, doi: 10.1016/j.jpowsour.2007.06.217.

[7] C. Delmas *et al.*, “An overview of the Li(Ni,M)O2 systems: syntheses, structures and properties,” *Electrochim. Acta*, vol. 45, no. 1–2, pp. 243–253, Sep. 1999, doi: 10.1016/S0013-4686(99)00208-X.

[8] M. Broussely, P. Biensan, and B. Simon, “Lithium insertion into host materials: the key to success for Li ion batteries,” *Electrochim. Acta*, vol. 45,

no. 1, pp. 3–22, 1999, doi: 10.1016/S0013-4686(99)00189-9.

[9] N. Nitta, F. Wu, J. T. Lee, and G. Yushin, “Li-ion battery materials: Present and future,” *Mater. Today*, vol. 18, no. 5, pp. 252–264, 2015, doi: 10.1016/j.mattod.2014.10.040.

[10] A. Manthiram, “A reflection on lithium-ion battery cathode chemistry,” *Nat. Commun.*, vol. 11, no. 1, pp. 1–9, 2020, doi: 10.1038/s41467-020-15355-0.

[11] K. Mizushima, P. C. Jones, P. J. Wiseman, and J. B. Goodenough, “LixCoO2 (0<x<-1): A new cathode material for batteries of high energy density,” *Mater. Res. Bull.*, vol. 15, no. 6, pp. 783–789, Jun. 1980, doi: 10.1016/0025-5408(80)90012-4.

[12] M. M. Thackeray, W. I. F. David, and J. B. Goodenough, “Structural characterization of the lithiated iron oxides LixFe3O4 and LixFe2O3 (0<x<2),” *Mater. Res. Bull.*, vol. 17, no. 6, pp. 785–793, Jun. 1982, doi: 10.1016/0025-5408(82)90029-0.

[13] A. Manthiram and J. B. Goodenough, “Lithium insertion into Fe2(MO4)3 frameworks: Comparison of M = W with M = Mo,” *J. Solid State Chem.*, vol. 71, no. 2, pp. 349–360, Dec. 1987, doi: 10.1016/0022-4596(87)90242-8.

[14] A. Kraytsberg, Y. Ein-Eli, A. Kraytsberg, and Y. Ein-Eli, “Higher, stronger, better ... A review of 5 volt cathode materials for advanced lithium-ion batteries,” *Adv. Energy Mater.*, vol. 2, no. 8, pp. 922–939, 2012, doi: 10.1002/aenm.201200068.

[15] A. Du Pasquier, I. Plitz, S. Menocal, and G. Amatucci, “A comparative study of Li-ion battery, supercapacitor and nonaqueous asymmetric hybrid devices for automotive applications,” *J. Power Sources*, vol. 115, no. 1, pp. 171–178, 2003, doi: 10.1016/S0378-7753(02)00718-8.

[16] C. M. Julien and J. Prakash, *New trends in intercalation compounds for*

energy storage and conversion : proceedings of the international symposium / editors, K. Zaghib, C.M. Julien, J. Prakash. Electrochemical Society, 2003.

[17] Y. S. Jung, A. S. Cavanagh, A. C. Dillon, M. D. Groner, S. M. George, and S.-H. Lee, "Enhanced Stability of LiCoO[sub 2] Cathodes in Lithium-Ion Batteries Using Surface Modification by Atomic Layer Deposition," *J. Electrochem. Soc.*, vol. 157, no. 1, p. A75, 2010, doi: 10.1149/1.3258274.

[18] A. Yano, M. Shikano, A. Ueda, H. Sakaebe, and Z. Ogumi, " LiCoO 2 Degradation Behavior in the High-Voltage Phase Transition Region and Improved Reversibility with Surface Coating ," *J. Electrochem. Soc.*, vol. 164, no. 1, pp. A6116–A6122, 2017, doi: 10.1149/2.0181701jes.

[19] J. R. Dahn, E. W. Fuller, M. Obrovac, and U. von Sacken, "Thermal stability of LixCoO2, LixNiO2 and λ-MnO2 and consequences for the safety of Li-ion cells," *Solid State Ionics*, vol. 69, no. 3–4, pp. 265–270, 1994, doi: 10.1016/0167-2738(94)90415-4.

[20] D. Aurbach *et al.*, "Review on electrode-electrolyte solution interactions, related to cathode materials for Li-ion batteries," *J. Power Sources*, vol. 165, no. 2, pp. 491–499, 2007, doi: 10.1016/j.jpowsour.2006.10.025.

[21] L. D. Dyer, B. S. Borie, and G. P. Smith, "Alkali Metal-Nickel Oxides of the Type MNiO2," *J. Am. Chem. Soc.*, vol. 76, no. 6, pp. 1499–1503, 1954, doi: 10.1021/ja01635a012.

[22] J. Välikangas, P. Laine, M. Hietaniemi, T. Hu, P. Tynjälä, and U. Lassi, "Precipitation and calcination of high-capacity linio2 cathode material for lithium-ion batteries," *Appl. Sci.*, vol. 10, no. 24, pp. 1–11, 2020, doi: 10.3390/app10248988.

[23] A. Rougier, P. Gravereau, and C. Delmas, "Optimization of the Composition of the Li1 − z Ni1 + z O 2 Electrode Materials: Structural, Magnetic, and

Electrochemical Studies," *J. Electrochem. Soc.*, vol. 143, no. 4, pp. 1168–1175, 1996, doi: 10.1149/1.1836614.

[24] C. H. Chen, J. Liu, M. E. Stoll, G. Henriksen, D. R. Vissers, and K. Amine, "Aluminum-doped lithium nickel cobalt oxide electrodes for high-power lithium-ion batteries," *J. Power Sources*, vol. 128, no. 2, pp. 278–285, Apr. 2004, doi: 10.1016/J.JPOWSOUR.2003.10.009.

[25] A. R. Armstrong and P. G. Bruce, "Synthesis of layered LiMnO2 as an electrode for rechargeable lithium batteries," *Nature*, vol. 381, no. 6582. pp. 499–500, 1996, doi: 10.1038/381499a0.

[26] M. Gu *et al.*, "Formation of the spinel phase in the layered composite cathode used in Li-Ion batteries," *ACS Nano*, vol. 7, no. 1, pp. 760–767, 2013, doi: 10.1021/nn305065u.

[27] L. Yunjian *et al.*, "Electrochemical performance and capacity fading reason of LiMn2O4/graphite batteries stored at room temperature," *J. Power Sources*, vol. 189, no. 1, pp. 721–725, Apr. 2009, doi: 10.1016/J.JPOWSOUR.2008.08.044.

[28] T. Doi *et al.*, "Electrochemical AFM study of LiMn2O4 thin film electrodes exposed to elevated temperatures," *J. Power Sources*, vol. 180, no. 1, pp. 539–545, May 2008, doi: 10.1016/J.JPOWSOUR.2008.02.054.

[29] N. Yabuuchi and T. Ohzuku, "Novel lithium insertion material of LiCo1/3Ni1/3Mn1/3O2 for advanced lithium-ion batteries," *J. Power Sources*, vol. 119–121, pp. 171–174, Jun. 2003, doi: 10.1016/S0378-7753(03)00173-3.

[30] B. Pişkin and M. K. Aydinol, "Development and characterization of layered Li(NixMnyCo1−x−y)O2 cathode materials for lithium ion batteries," *Int. J. Hydrogen Energy*, vol. 41, no. 23, pp. 9852–9859, Jun. 2016, doi:

10.1016/J.IJHYDENE.2016.03.127.

[31] F. Lin *et al.*, “Surface reconstruction and chemical evolution of stoichiometric layered cathode materials for lithium-ion batteries,” *Nat. Commun.*, vol. 5, p. 3529, 2014, doi: 10.1038/ncomms4529.

[32] K. Ben-Kamel, N. Amdouni, A. Mauger, and C. M. Julien, “Study of the local structure of LiNi 0.33+δMn 0.33+δCo 0.33-2δO 2 (0.025 ≤ δ ≤ 0.075) oxides,” *J. Alloys Compd.*, vol. 528, pp. 91–98, 2012, doi: 10.1016/j.jallcom.2012.03.018.

[33] S. Jouanneau, K. W. Eberman, L. J. Krause, and J. R. Dahn, “Synthesis, Characterization, and Electrochemical Behavior of Improved Li[Ni[sub x]Co[sub 1−2x]Mn[sub x]]O[sub 2] (0.1≤x≤0.5),” *J. Electrochem. Soc.*, vol. 150, no. 12, p. A1637, 2003, doi: 10.1149/1.1622956.

[34] K. M. Shaju and P. G. Bruce, “Macroporous Li(Ni1/3Co1/3Mn1/3)O2: A high-rate positive electrode for rechargeable lithium batteries,” *J. Power Sources*, vol. 174, no. 2, pp. 1201–1205, 2007, doi: 10.1016/j.jpowsour.2007.06.091.

[35] K. S. Lee, S. T. Myung, J. Prakash, H. Yashiro, and Y. K. Sun, “Optimization of microwave synthesis of Li[Ni0.4Co0.2Mn0.4]O2 as a positive electrode material for lithium batteries,” *Electrochim. Acta*, vol. 53, no. 7, pp. 3065–3074, 2008, doi: 10.1016/j.electacta.2007.11.042.

[36] Z. Liu, A. Yu, and J. Y. Lee, “Synthesis and characterization of LiNi1-x-yCoxMnyO2 as the cathode materials of secondary lithium batteries,” *J. Power Sources*, vol. 81–82, pp. 416–419, 1999, doi: 10.1016/S0378-7753(99)00221-9.

[37] J. Zheng, W. H. Kan, and A. Manthiram, “Role of Mn content on the electrochemical properties of Nickel-Rich layered LiNi0.8-

xCo0.1Mn0.1+xO2 (0.0 ≤ x ≤ 0.08) cathodes for lithium-ion batteries," *ACS Appl. Mater. Interfaces*, vol. 7, no. 12, pp. 6926–6934, 2015, doi: 10.1021/acsami.5b00788.

[38] S. Liu, L. Xiong, and C. He, "Long cycle life lithium ion battery with lithium nickel cobalt manganese oxide (NCM) cathode," *J. Power Sources*, vol. 261, pp. 285–291, 2014, doi: 10.1016/j.jpowsour.2014.03.083.

[39] R. Jung, M. Metzger, F. Maglia, C. Stinner, and H. A. Gasteiger, "Chemical versus electrochemical electrolyte oxidation on NMC111, NMC622, NMC811, LNMO, and conductive carbon," *J. Phys. Chem. Lett.*, vol. 8, no. 19, pp. 4820–4825, 2017, doi: 10.1021/acs.jpclett.7b01927.

[40] E. M. Erickson *et al.*, "Review—Recent Advances and Remaining Challenges for Lithium Ion Battery Cathodes," *J. Electrochem. Soc.*, vol. 164, no. 1, pp. A6341–A6348, 2017, doi: 10.1149/2.0461701jes.

[41] K. W. Nam *et al.*, "Combining in situ synchrotron X-Ray diffraction and absorption techniques with transmission electron microscopy to study the origin of thermal instability in overcharged cathode materials for lithium-ion batteries," *Adv. Funct. Mater.*, vol. 23, no. 8, pp. 1047–1063, 2013, doi: 10.1002/adfm.201200693.

[42] J. K. Ngala, N. A. Chernova, M. Ma, M. Mamak, P. Y. Zavalij, and M. S. Whittingham, "The synthesis, characterization and electrochemical behavior of the layered LiNi0.4Mn0.4Co0.2O2 compound," *J. Mater. Chem.*, vol. 14, no. 2, pp. 214–220, 2004, doi: 10.1039/b309834f.

[43] M. Yoshio, H. Noguchi, J. ichi Itoh, M. Okada, and T. Mouri, "Preparation and properties of LiCoyMnxNi1-x-yO2 as a cathode for lithium ion batteries," *J. Power Sources*, vol. 90, no. 2, pp. 176–181, 2000, doi: 10.1016/S0378-7753(00)00407-9.

[44] Y. K. Lin and C. H. Lu, “Preparation and electrochemical properties of layer-structured LiNi1/3Co1/3Mn1/3-yAlyO2,” *J. Power Sources*, vol. 189, no. 1, pp. 353–358, 2009, doi: 10.1016/j.jpowsour.2008.08.072.

[45] J. Wilcox, S. Patoux, and M. Doeff, “Structure and Electrochemistry of LiNi[sub 1⁄3]Co[sub 1⁄3−y]M[sub y]Mn[sub 1⁄3]O[sub 2] (M=Ti, Al, Fe) Positive Electrode Materials,” *J. Electrochem. Soc.*, vol. 156, no. 3, p. A192, 2009, doi: 10.1149/1.3056109.

[46] C. C. Wang, Y. C. Lin, and P. H. Chou, “Mitigation of layer to spinel conversion of a lithium-rich layered oxide cathode by substitution of Al in a lithium ion battery,” *RSC Adv.*, vol. 5, no. 84, pp. 68919–68928, 2015, doi: 10.1039/c5ra11665a.

[47] Y. P. Zhang, E. Q. Liang, J. X. Wang, B. J. Yu, C. Y. Wang, and M. W. Li, “Effect of aluminum doping on the stability of lithium-rich layered oxide Li[Li0.23Ni0.15Mn0.52Al0.10]O2 as cathode material,” *Int. J. Electrochem. Sci.*, vol. 12, no. 10, pp. 9051–9060, 2017, doi: 10.20964/2017.10.62.

[48] S. Rajakumar, R. Thirunakaran, A. Sivashanmugam, J. Yamaki, and S. Gopukumar, “Electrochemical Behavior of LiM[sub 0.25]Ni[sub 0.25]Mn[sub 1.5]O[sub 4] as 5 V Cathode Materials for Lithium Rechargeable Batteries,” *J. Electrochem. Soc.*, vol. 156, no. 3, p. A246, 2009, doi: 10.1149/1.3071364.

[49] U. H. Kim *et al.*, “Pushing the limit of layered transition metal oxide cathodes for high-energy density rechargeable Li ion batteries,” *Energy Environ. Sci.*, vol. 11, no. 5, pp. 1271–1279, 2018, doi: 10.1039/c8ee00227d.

[50] A. Jihad, A. A. N. Pratama, C. S. Yudha, M. Rahmawati, H. Widiyandari, and A. Purwanto, “Effect of Zn, Cu and Mg doping on the structural characteristic of LiNi0.6Mn0.2Co0.2O2 (NMC622),” *PervasiveHealth*

Pervasive Comput. Technol. Healthc., vol. 2, pp. 0–6, 2020, doi: 10.1145/3429789.3429857.

[51] L. Yang *et al.*, “Effect of Cu Doping on the Structural and Electrochemical Performance of LiNi1/3Co1/3Mn1/3O2 Cathode Materials,” *J. Electron. Mater.*, vol. 47, no. 7, pp. 3996–4002, 2018, doi: 10.1007/s11664-018-6284-8.

[52] C. Vinodbabu, G. T. Rao, N. B. Reddy, and G. V. Zyryanov, “A review on magnetron sputter coatings,” *AIP Conf. Proc.*, vol. 2280, no. October, 2020, doi: 10.1063/5.0018142.

[53] S. Shahidi, B. Moazzenchi, and M. Ghoranneviss, “A review-application of physical vapor deposition (PVD) and related methods in the textile industry,” *EPJ Appl. Phys.*, vol. 71, no. 3, pp. 1–13, 2015, doi: 10.1051/epjap/2015140439.

[54] B. Uzakbaiuly, A. Mukanova, Y. Zhang, and Z. Bakenov, “Physical Vapor Deposition of Cathode Materials for All Solid-State Li Ion Batteries: A Review,” *Front. Energy Res.*, vol. 9, no. May, pp. 1–16, 2021, doi: 10.3389/fenrg.2021.625123.

[55] D. K. Maurya, A. Sardarinejad, and K. Alameh, “Recent developments in R.F. magnetron sputtered thin films for pH sensing applications-an overview,” *Coatings*, vol. 4, no. 4, pp. 756–771, 2014, doi: 10.3390/coatings4040756.

[56] P. J. Kelly and R. D. Arnell, “Magnetron sputtering: a review of recent developments and applications,” *Vacuum*, vol. 56, no. 3, pp. 159–172, Mar. 2000, doi: 10.1016/S0042-207X(99)00189-X.

[57] R. Surmenev *et al.*, “Radio Frequency Magnetron Sputter Deposition as a Tool for Surface Modification of Medical Implants,” *Mod. Technol. Creat.*

Thin-film Syst. Coatings, 2017, doi: 10.5772/66396.

[58] X. Q. Tan, J. Y. Liu, J. R. Niu, J. Y. Liu, and J. Y. Tian, “Recent progress in magnetron sputtering technology used on fabrics,” *Materials (Basel).*, vol. 11, no. 10, 2018, doi: 10.3390/ma11101953.

[59] M. Nur-E-Alam, M. Vasiliev, V. Kotov, and K. Alameh, “Recent developments in magneto-optic garnet-type thin-film materials synthesis,” *Procedia Eng.*, vol. 76, pp. 61–73, 2014, doi: 10.1016/j.proeng.2013.09.248.

[60] P. F. Carcia, R. S. McLean, M. H. Reilly, and G. Nunes, “Transparent ZnO thin-film transistor fabricated by rf magnetron sputtering,” *Appl. Phys. Lett.*, vol. 82, no. 7, pp. 1117–1119, 2003, doi: 10.1063/1.1553997.

[61] J. F. Whitacre, W. C. West, and B. V. Ratnakumar, “The influence of target history and deposition geometry on RF magnetron sputtered LiCoO2 thin films,” *J. Power Sources*, vol. 103, no. 1, pp. 134–139, 2001, doi: 10.1016/S0378-7753(01)00849-7.

[62] G. R. G. et al. J. B. Bates, N. J. Dudney, “Fabrication and characterization of amorphous lithium electrolyte thin films and rechargeable thin-film batteries,” *J. Power Sources*, vol. 43, no. 1–3, pp. 103–110, 1993.

[63] B. Wang, J. B. Bates, F. X. Hart, B. C. Sales, R. A. Zuhr, and J. D. Robertson, “Characterization of Thin-Film Rechargeable Lithium Batteries with Lithium Cobalt Oxide Cathodes,” *J. Electrochem. Soc.*, vol. 143, no. 10, pp. 3203–3213, 1996, doi: 10.1149/1.1837188.

[64] P. Fragnaud, T. Brousse, and D. M. Schleich, “Characterization of sprayed and sputter deposited LiCoO2 thin films for rechargeable microbatteries,” *J. Power Sources*, vol. 63, no. 2, pp. 187–191, 1996, doi: 10.1016/S0378-7753(96)02464-0.

[65] Z. Qi and H. Wang, “Advanced Thin Film Cathodes for Lithium Ion

Batteries," *Research*, vol. 2020, pp. 1–24, 2020, doi: 10.34133/2020/2969510.

[66] M. Létiche, M. Hallot, M. Huvé, T. Brousse, P. Roussel, and C. Lethien, "Tuning the Cation Ordering with the Deposition Pressure in Sputtered LiMn1.5Ni0.5O4 Thin Film Deposited on Functional Current Collectors for Li-Ion Microbattery Applications," *Chem. Mater.*, vol. 29, no. 14, pp. 6044–6057, 2017, doi: 10.1021/acs.chemmater.7b01921.

[67] N. Kuwata, J. Kawamura, K. Toribami, T. Hattori, and N. Sata, "Thin-film lithium-ion battery with amorphous solid electrolyte fabricated by pulsed laser deposition," *Electrochem. commun.*, vol. 6, no. 4, pp. 417–421, Apr. 2004, doi: 10.1016/J.ELECOM.2004.02.010.

[68] J. Trask *et al.*, "Optimization of 10-Mm, sputtered, LiCoO2 cathodes to enable higher energy density solid state batteries," *J. Power Sources*, vol. 350, pp. 56–64, 2017, doi: 10.1016/j.jpowsour.2017.03.017.

[69] G. Wei, T. E. Haas, and R. B. Goldner, "Thin films of lithium cobalt oxide," *Solid State Ionics*, vol. 58, no. 1–2, pp. 115–122, Nov. 1992, doi: 10.1016/0167-2738(92)90018-K.

[70] C. Priestland and S. D. Hersee, "The effects of pressure on the deposition rate in rf sputtering processes," *Vacuum*, vol. 22, no. 3, pp. 103–106, Mar. 1972, doi: 10.1016/0042-207X(72)90468-X.

[71] L. Dimesso, "Handbook of Sol-Gel Science and Technology," *Handb. Sol-Gel Sci. Technol.*, 2017, doi: 10.1007/978-3-319-19454-7.

[72] H. Lee, M. Hong, S. Bae, H. Lee, E. Park, and K. Kim, "A novel approach to preparing nano-size Co3O4-coated Ni powder by the Pechini method for MCFC cathodes," *J. Mater. Chem.*, vol. 13, no. 10, pp. 2626–2632, 2003, doi: 10.1039/b303980c.

[73] J. E. Unosson, C. Persson, and H. Engqvist, “An evaluation of methods to determine the porosity of calcium phosphate cements,” *J. Biomed. Mater. Res. - Part B Appl. Biomater.*, vol. 103, no. 1, pp. 62–71, 2015, doi: 10.1002/jbm.b.33173.

[74] D. Sari, Z. C. Torunoglu, Y. E. Kalay, and T. Ozturk, “Preparation of La0.8Sr0.2CoO3-δ sputtering targets using a deformable compaction die,” *Ceram. Int.*, vol. 43, no. 17, pp. 15185–15188, 2017, doi: 10.1016/j.ceramint.2017.08.050.

APPENDICES

A. EDS Results of First Set Experiments

Exp. No	Sample No	Co (%at)	Mn (%at)	Ni (%at)
1	1	44.77	18.35	36.88
	2	29.37	22	48.63
	3	30.42	25.51	44.06
	4	22.14	22.58	55.29
	5	24.32	26.6	49.08
	6	22.73	34.4	42.88
	7	12.9	23.75	63.35
	8	13.28	29	57.72
	9	14.69	35.36	49.95
	10	12.95	45.2	41.86
	11	6.45	22.59	70.96
	12	8.12	26.68	65.19
	13	9.03	34.67	56.29
	14	8.16	45.59	46.26
	15	7.99	52.92	39.09
	16	3.5	21.37	75.13
	17	4.21	24.42	71.37
	18	5.92	32.23	61.85
	19	6.59	38.34	55.08
	20	4.07	58.02	37.91
	21	4.61	59.73	35.66
2	1	44.18	17.25	38.57
	2	29.28	21.73	48.99
	3	34.36	24.22	41.42
	4	17.89	23.61	58.49
	5	20.19	29	50.81
	6	23.3	33.85	42.85
	7	11.49	24.08	64.43

Exp. No	Sample No	Co (%at)	Mn (%at)	Ni (%at)
2	8	12.09	29.63	58.28
	9	15.6	36.02	48.38
	10	13.17	46.67	40.16
	11	5.31	23.12	71.57
	12	7.92	28.26	63.82
	13	9.02	35.45	55.54
	14	8.32	46.05	45.63
	15	7.63	53.59	38.78
	16	3.32	22.35	74.32
	17	4.32	25.87	69.81
	18	5	32.63	62.37
	19	6.33	41.75	51.92
	20	4.98	53.24	41.78
	21	4.87	58.91	36.21
3	1	51.4	9.42	39.18
	2	35.31	13.16	51.53
	3	38.34	15	46.66
	4	23.72	16.14	60.14
	5	26.8	18.36	54.85
	6	25.91	20.46	53.64
	7	12.65	19.26	68.09
	8	14.52	20.13	65.35
	9	19.54	23.38	57.09
	10	17.18	28.97	53.86
	11	6.28	18.64	75.08
	12	9.14	21.22	69.64
	13	12.62	24.09	63.28
	14	12.07	29.93	58
	15	12.17	36.79	51.03
	16	3.39	18.88	77.73
	17	4.69	20.4	74.91
	18	6.56	24.57	68.87
	19	7.38	27.68	64.94
	20	7.49	38.61	53.91
	21	7.71	45.69	46.6

B. Mass Calculations of First Set Experiments

Exp. No	Sample No	Ni Foil (g)	Coated (g)	Film Mass (g)	Film Mass (mg)
1	1	0.03473	0.03678	0.00205	2.05
	2	0.03467	0.03655	0.00188	1.88
	3	0.03442	0.03648	0.00206	2.06
	4	0.03468	0.03637	0.00169	1.69
	5	0.03531	0.03684	0.00153	1.53
	6	0.03487	0.03671	0.00184	1.84
	7	0.03501	0.03708	0.00207	2.07
	8	0.03517	0.03712	0.00195	1.95
	9	0.03457	0.03618	0.00161	1.61
	10	0.03512	0.03672	0.0016	1.6
	11	0.03515	0.03797	0.00282	2.82
	12	0.03533	0.03749	0.00216	2.16
	13	0.03497	0.03729	0.00232	2.32
	14	0.03523	0.03723	0.002	2
	15	0.03476	0.03707	0.00231	2.31
	16	0.03502	0.03919	0.00417	4.17
	17	0.03497	0.03822	0.00325	3.25
	18	0.03483	0.03784	0.00301	3.01
	19	0.03531	0.03749	0.00218	2.18
	20	0.03498	0.03738	0.0024	2.4
	21	0.03482	0.03782	0.003	3

Exp. No	Sample No	Ni Foil (g)	Coated (g)	Film Mass (g)	Film Mass (mg)
3	1	0.03446	0.03643	0.00197	1.97
	2	0.03454	0.03633	0.00179	1.79
	3	0.03452	0.03623	0.00171	1.71
	4	0.03475	0.03631	0.00156	1.56
	5	0.03493	0.03659	0.00166	1.66
	6	0.0351	0.03646	0.00136	1.36
	7	0.03499	0.03724	0.00225	2.25
	8	0.03497	0.03677	0.0018	1.8
	9	0.03498	0.0365	0.00152	1.52
	10	0.03553	0.03695	0.00142	1.42
	11	0.03517	0.03807	0.0029	2.9
	12	0.03502	0.03739	0.00237	2.37
	13	0.03506	0.03699	0.00193	1.93
	14	0.03512	0.03682	0.0017	1.7
	15	0.03521	0.03678	0.00157	1.57
	16	0.03525	0.03943	0.00418	4.18
	17	0.03528	0.03832	0.00304	3.04
	18	0.03515	0.03752	0.00237	2.37
	19	0.03476	0.03706	0.0023	2.3
	20	0.03482	0.03683	0.00201	2.01
	21	0.03508	0.03688	0.0018	1.8

C. Thickness Measurements of First Set

Sample no	Thickness (µm)
1	2.26
2	2.29
3	3.87
4	2.48
5	2.35
6	2.3
7	3.09
8	2.61
9	2.44
10	2.46
11	3.39
12	3.01
13	2.7
14	2.39
15	2.68
16	4.32
17	3.1
18	2.91
19	2.7
20	3.24
21	3.66

D. EDS Results of Second Set of Experiments

Exp No	Sample No	Co (%at)	Mn (%at)	Ni (%at)	W (%at)
1	1	44.61	4.16	46.9	4.33
	2	30.45	7.27	57.78	4.5
	3	27.93	7.83	57.17	7.07
	4	17.52	10.96	66.76	4.77
	5	17.13	11.01	64.9	6.96
	6	18.32	10.97	61.76	8.95
	7	12.45	13.4	70.48	3.67
	8	12.46	12.28	69.49	5.77
	9	10.4	12.57	66.02	11.01
	10	10.97	12.86	62.91	13.26
	11	6.17	17.23	72.47	4.13
	12	5.86	15.99	72.64	5.5
	13	6.69	15.66	66.64	11.01
	14	6.58	14.53	64.67	14.22
	15	3.75	13.93	60	22.32
	16	2.46	19.32	76.09	2.13
	17	2.81	18.67	74.28	4.24
	18	3.97	17.44	70.75	7.83
	19	4.43	16.07	64.74	14.75
	20	3.86	13.71	56.52	25.9
	21	2.79	14.04	56.66	26.51

Exp No	Sample No	Co (%at)	Mn (%at)	Ni (%at)	W (%at)	Cu (%at)
2	1	33.77	6.06	53.1	2.49	4.58
	2	23.21	9.02	59.68	3.39	4.7
	3	27.49	8.08	58.47	3.65	2.3
	4	16.09	11.53	66.73	3.16	2.49
	5	15.64	11.88	63.74	4.99	3.75
	6	16.62	10.96	64.36	5.84	2.2
	7	10.3	14.91	71.6	2	1.19
	8	9.52	14.94	70.72	4.47	0.35
	9	11.3	14.65	64.53	7.66	1.86
	10	9.76	13.95	63.98	9.99	2.32
	11	5.98	16.5	72.64	3.08	1.8
	12	6.2	16.06	72.1	5.19	0.44
	13	6.79	15.61	67.9	8.06	1.63
	14	6.9	15	64.33	11.95	1.82
	15	4.53	14.9	61.06	18	1.51
	16	2.56	19.18	74.75	2.18	1.34
	17	3.36	18.43	73.05	3.42	1.74
	18	3.91	16.59	71.2	5.96	1.89
	19	4.9	16.04	65.73	11.7	1.63
	20	3.57	14.14	56.23	24.62	1.45
	21	1.95	13.87	54.1	28.52	1.56

Exp No	Sample No	Co (%at)	Mn (%at)	Ni (%at)	W (%at)	Fe (%at)
3	1	30.08	5.45	56.94	2.55	4.98
	2	23.02	8.26	60.08	4.67	3.97
	3	23.58	8.83	61.13	3.04	3.42
	4	12.31	13.14	69.22	3.62	1.72
	5	10.5	8.86	74.89	4.05	1.71
	6	13.33	11.6	65.67	7.39	2.01
	7	8.88	14.47	71.27	3.65	1.73
	8	8.74	13.87	71.13	4.8	1.46
	9	8.27	12.95	66.41	10.99	1.38
	10	9.02	14.12	68.21	7.4	1.25
	11	3.75	18.48	73.73	2.83	1.22
	12	6.01	16.82	71.99	4.25	0.93
	13	5.55	15.44	68.82	9.1	1.09
	14	5.2	14.66	66.17	12.55	1.42
	15	5.1	15.45	61.94	16.48	1.04
	16	2.1	19.03	75.68	2.54	0.65
	17	4.22	17.91	72.98	3.99	0.9
	18	3.52	16.71	71.3	7.53	0.94
	19	3.94	15.08	67.89	12.07	1.03
	20	2.89	13.77	55.46	26.9	0.98
	21	2.56	14.62	56.47	25.34	1.02

Exp No	Sample No	Co (%at)	Mn (%at)	Ni (%at)	Al (%at)	Fe (%at)
4	1	34.62	5.46	51.14	2.9	5.88
	2	20.06	7.1	62.13	7.81	2.9
	3	23.67	7.64	60.88	4.65	3.16
	4	14.06	10.76	66.08	7.56	1.54
	5	13.57	10.72	65.58	7.85	2.29
	6	14.44	10.28	64.38	9.44	1.46
	7	8.26	14.99	70.01	5.41	1.33
	8	8.62	13.98	69.83	6.33	1.24
	9	9.68	11.46	65.3	11.93	1.62
	10	8.46	13.35	64.57	12.18	1.45
	11	3.93	16.95	72.57	5.52	1.02
	12	4.74	15.84	72.03	6.29	1.11
	13	5.3	14.98	68.71	10.36	0.65
	14	6.17	14.04	66.13	12.34	1.32
	15	4.02	15.17	61.78	18.34	0.7
	16	2.34	17.67	75.21	4.4	0.38
	17	3.54	16.52	72.75	6.3	0.89
	18	3.77	15.53	70.4	9.11	1.19
	19	3.64	14.89	67.17	13.49	0.81
	20	3.38	14.83	61.82	18.88	1.09
	21	1.61	14.82	57.59	25.38	0.6

Exp No	Sample No	Co (%at)	Mn (%at)	Ni (%at)	Al (%at)	Cu (%at)
5	1	38.06	5.84	47.93	3.52	4.65
	2	24.61	8.44	58.11	3.39	5.45
	3	26.49	8.45	55.92	3.21	5.93
	4	15.94	10.99	62.04	8.08	2.96
	5	17.29	11.51	61.52	6.31	3.37
	6	16.45	9.93	58.95	11.1	3.57
	7	8.17	15	69.93	4.23	2.67
	8	9.88	13.47	66.44	7.83	2.38
	9	11.34	13.17	64.47	7.99	3.04
	10	9.75	13.6	63.29	11.15	2.2
	11	5.52	16.72	71.83	4.56	1.36
	12	6.2	14.88	70.67	6.15	2.1
	13	6.54	15.83	68.82	7.83	0.98
	14	5.71	15.25	64.34	12.95	1.75
	15	4.53	15.3	63.87	14.3	2
	16	2.21	18.1	71.58	6.51	1.6
	17	3.01	16.92	73.75	4.81	1.51
	18	4.09	16.47	70.97	7.69	0.78
	19	4.31	16.03	66.58	11.73	1.36
	20	3.13	15.71	60.61	19.27	1.26
	21	2.57	15.87	61.25	19.1	1.21

Exp No	Sample No	Co (%at)	Mn (%at)	Ni (%at)	Al (%at)
6	1	37.2	5.4	50.96	6.45
	2	21.59	8.84	61.5	8.07
	3	21.32	8.89	63.55	6.24
	4	15.17	12.37	66.57	5.88
	5	14.88	11.39	65.25	8.48
	6	15.08	11.08	62.74	11.1
	7	7.3	14.88	71.5	6.77
	8	9.13	13.91	67.53	9.42
	9	9.34	12.66	64.66	13.34
	10	8.75	13.39	63.92	13.94
	11	4.51	16.89	72.61	6
	12	4.57	16.38	71.26	7.79
	13	6.24	14.7	67.66	11.41
	14	6.09	15.03	65.1	13.78
	15	4.86	16.45	63.69	14.99
	16	1.69	18.18	75.18	4.95
	17	2.78	16.42	72.2	8.6
	18	3.08	16.64	68.23	12.05
	19	3.63	16.26	69.09	11.02
	20	3.32	15.58	61.88	19.22
	21	2.47	16.46	62.38	18.69

E. Mass Calculations of First Set Experiments

Columns ‘Ni foil’ and ‘Coated’ should be multiplied by 10^{-4} to reach real g. values.

Exp. No	Sample No	Ni Foil (g)	Coated (g)	Film Mass (g)	Film Mass (mg)
1	1	349	368	0.0019	1.9
	2	351	368	0.0017	1.7
	3	349	364	0.0015	1.5
	4	349	367	0.0018	1.8
	5	348	369	0.0021	2.1
	6	342	361	0.0019	1.9
	7	343	363	0.002	2
	8	341	362	0.0021	2.1
	9	344	362	0.0018	1.8
	10	343	362	0.0019	1.9
	11	341	366	0.0025	2.5
	12	347	373	0.0026	2.6
	13	354	372	0.0018	1.8
	14	351	370	0.0019	1.9
	15	353	381	0.0028	2.8
	16	352	384	0.0032	3.2
	17	352	372	0.002	2
	18	347	369	0.0022	2.2
	19	349	372	0.0023	2.3
	20	354	384	0.003	3
	21	352	393	0.0041	4.1
2	1	341	359	0.0018	1.8
	2	352	366	0.0014	1.4
	3	350	367	0.0017	1.7
	4	345	363	0.0018	1.8
	5	343	359	0.0016	1.6
	6	349	364	0.0015	1.5
	7	352	364	0.0012	1.2
	8	355	371	0.0016	1.6
	9	345	358	0.0013	1.3

Exp. No	Sample No	Ni Foil (g)	Coated (g)	Film Mass (g)	Film Mass (mg)
2	10	344	359	0.0015	1.5
	11	342	364	0.0022	2.2
	12	349	369	0.002	2
	13	346	364	0.0018	1.8
	14	342	360	0.0018	1.8
	15	352	373	0.0021	2.1
	16	351	374	0.0023	2.3
	17	345	362	0.0017	1.7
	18	347	366	0.0019	1.9
	19	351	371	0.002	2
	20	356	380	0.0024	2.4
	21	347	382	0.0035	3.5
3	1	349	365	0.0016	1.6
	2	346	360	0.0014	1.4
	3	347	358	0.0011	1.1
	4	347	364	0.0017	1.7
	5	341	360	0.0019	1.9
	6	344	359	0.0015	1.5
	7	345	367	0.0022	2.2
	8	350	366	0.0016	1.6
	9	343	357	0.0014	1.4
	10	344	355	0.0011	1.1
	11	342	363	0.0021	2.1
	12	351	369	0.0018	1.8
	13	347	363	0.0016	1.6
	14	344	359	0.0015	1.5
	15	342	359	0.0017	1.7
	16	349	376	0.0027	2.7
	17	353	371	0.0018	1.8
	18	354	370	0.0016	1.6
	19	351	369	0.0018	1.8
	20	352	375	0.0023	2.3
	21	354	379	0.0025	2.5

Exp. No	Sample No	Ni Foil (g)	Coated (g)	Film Mass (g)	Film Mass (mg)
4	1	348	356	0.0008	0.8
	2	351	355	0.0004	0.4
	3	355	357	0.0002	0.2
	4	353	360	0.0007	0.7
	5	352	362	0.001	1
	6	348	362	0.0014	1.4
	7	350	363	0.0013	1.3
	8	352	364	0.0012	1.2
	9	354	365	0.0011	1.1
	10	352	365	0.0013	1.3
	11	352	372	0.002	2
	12	353	369	0.0016	1.6
	13	353	365	0.0012	1.2
	14	351	364	0.0013	1.3
	15	344	367	0.0023	2.3
	16	351	374	0.0023	2.3
	17	352	369	0.0017	1.7
	18	354	368	0.0014	1.4
	19	354	369	0.0015	1.5
	20	353	370	0.0017	1.7
	21	352	379	0.0027	2.7
5	1	357	366	0.0009	0.9
	2	355	365	0.001	1
	3	357	366	0.0009	0.9
	4	360	363	0.0003	0.3
	5	356	365	0.0009	0.9
	6	359	364	0.0005	0.5
	7	357	368	0.0011	1.1
	8	361	366	0.0005	0.5
	9	359	365	0.0006	0.6

Exp. No	Sample No	Ni Foil (g)	Coated (g)	Film Mass (g)	Film Mass (mg)
5	10	356	366	0.001	1
	11	355	369	0.0014	1.4
	12	353	369	0.0016	1.6
	13	356	369	0.0013	1.3
	14	354	368	0.0014	1.4
	15	358	367	0.0009	0.9
	16	352	374	0.0022	2.2
	17	349	367	0.0018	1.8
	18	349	364	0.0015	1.5
	19	351	365	0.0014	1.4
	20	348	367	0.0019	1.9
	21	352	372	0.002	2
6	1	355	365	0.001	1
	2	354	367	0.0013	1.3
	3	356	366	0.001	1
	4	358	365	0.0007	0.7
	5	354	367	0.0013	1.3
	6	356	367	0.0011	1.1
	7	356	369	0.0013	1.3
	8	353	367	0.0014	1.4
	9	356	368	0.0012	1.2
	10	357	368	0.0011	1.1
	11	353	372	0.0019	1.9
	12	352	370	0.0018	1.8
	13	358	372	0.0014	1.4
	14	353	370	0.0017	1.7
	15	354	373	0.0019	1.9
	16	354	379	0.0025	2.5
	17	358	375	0.0017	1.7
	18	355	372	0.0017	1.7
	19	357	373	0.0016	1.6
	20	356	373	0.0017	1.7
	21	358	380	0.0022	2.2

F. Electrochemical Characterization Results

Set No	Sample No	Current (mA)	Cycle No	Capacity (mAh/g)	Energy (Wh/Kg)
1	3	20	1	43.32	107.35
			2	33.29	85.51
			3	33.69	89.22
		40	4	29.21	78.58
			5	32.8	89.21
			6	34.28	93.73
	6	20	1	61.16	152.08
			2	50.88	134.2
			3	56.72	153.92
		40	4	50.76	139.34
			5	52.86	146.24
			6	51.07	141.46
	12	20	1	18.43	41.46
			2	12.99	30.71
			3	16.45	39.7
		40	4	16.11	39.59
			5	18.33	45.42
			6	21.18	52.98
	16	20	1	24.26	51.04
			2	16.9	37.35
			3	19.43	44.71
		40	4	16.12	37.4
			5	24.91	58.94
			6	30.55	73.62
	19	20	1	6.62	15.13
			2	5.16	12.18
			3	5.29	12.72
		40	4	4.4	10.86
			5	4.43	10.92
			6	4.47	11.05

Set No	Sample No	Current (mA)	Cycle No	Capacity (mAh/g)	Energy (Wh/Kg)
2	3	20	1	87.53	209.06
			2	82.27	215.67
			3	93.12	248.96
		40	4	87.53	235.13
			5	109.29	296.41
			6	109.82	306.53
	7	20	1	49.94	116.93
			2	48.61	126.44
			3	56.33	149.34
		40	4	62.36	167.51
			5	70.85	192.95
			6	76.43	212.85
	11	20	1	56.2	136.74
			2	73.65	187.87
			3	80.23	213.77
		40	4	71.36	199.58
			5	78.65	227.93
			6	85.23	249.07
	13	20	1	7.75	17.29
			2	17.95	45.27
			3	24.56	70.81
		40	4	40.44	127.98
			5	51.26	165.33
			6	57.02	185.37
	16	20	1	53.17	125.34
			2	64.36	172.59
			3	72.45	198.57
		40	4	70.15	194.04
			5	82.98	233.72
			6	90.21	259.75
	18	20	1	78.31	193.97
			2	70.44	188.19
			3	83.69	228.84
		40	4	81.65	225.48
			5	90.95	258.73
			6	97.32	283.16

Set No	Sample No	Current (mA)	Cycle No	Capacity (mAh/g)	Energy (Wh/Kg)
3	3	20	1	46.69	113.55
			2	75.29	206.62
			3	75.09	208.74
		40	4	54.28	148.85
			5	56.49	152.12
			6	53.24	146.28
	7	20	1	49.48	122.47
			2	71.11	189.88
			3	83.81	233.2
		40	4	95.33	264.76
			5	96.45	269.18
			6	94.52	264.97
	11	20	1	43.51	101.14
			2	64.63	161.48
			3	127.34	331.2
		40	4	108.29	284.43
			5	148.01	398.55
			6	157.4	428.3
	13	20	1	45.09	111.17
			2	58.9	161.18
			3	65.48	181.78
		40	4	49.41	137.49
			5	45.78	127.97
			6	44.15	123.76
	16	20	1	9.16	21.32
			2	21.19	51.7
			3	22.79	60.84
		40	4	21.16	58.93
			5	24.17	71.03
			6	34.91	106.19
	18	20	1	45.7	112.59
			2	61.68	166.5
			3	67.53	187.65
		40	4	60.26	169.81
			5	78.64	219.93
			6	83	234.2

Set No	Sample No	Current (mA)	Cycle No	Capacity (mAh/g)	Energy (Wh/Kg)
4	3	20	1	62.18	158.05
			2	83.66	226.18
			3	93.17	257.47
		40	4	82.94	229.76
			5	80.97	230.04
			6	92.69	262.79
	7	20	1	107.75	265.41
			2	100.11	265.02
			3	130.92	360.78
		40	4	115.64	324
			5	118.14	336.69
			6	58.9	168.42
	11	20	1	37.99	87.86
			2	45.07	107.1
			3	95.28	278.41
		40	4	96.87	282.51
			5	97.99	286.23
			6	93.67	273.14
	13	20	1	94.7	228.18
			2	102.8	264.19
			3	0	0
		40	4	130.38	358.43
			5	138.39	389.31
			6	139.64	397.09
	16	20	1	17.52	40.12
			2	38.68	98.91
			3	82.19	256.48
		40	4	88.22	276.83
			5	93.89	295.13
			6	97.22	307.76
	18	20	1	97.89	235.23
			2	90.86	232.33
			3	105.59	280.24
		40	4	91.72	250.34
			5	103.48	287.74
			6	103.95	290.9

Set No	Sample No	Current (mA)	Cycle No	Capacity (mAh/g)	Energy (Wh/Kg)
5	3	20	1	34.2	82.97
			2	42.99	113.35
			3	48.99	131.84
		40	4	44.05	120.26
			5	43.91	121.11
			6	42.65	118
	7	20	1	36.62	86.3
			2	44.42	115.17
			3	51.04	135.06
		40	4	24.04	55.49
			5	30.16	74.81
			6	32.25	82.06
	12	20	1	47.76	111.59
			2	58.3	151.94
			3	95.9	256.31
		40	4	92.34	252.44
			5	97.47	271.04
			6	99.44	278.89
	13	20	1	51.38	124.61
			2	58.03	155.32
			3	80.68	222.87
		40	4	80.03	224.17
			5	84.35	240.94
			6	87.68	252.18
	17	20	1	35.52	82.32
			2	63.13	163.84
			3	0	0
		40	4	89.87	252.53
			5	106.99	307.74
			6	109.19	316.75
	18	20	1	65.74	162.54
			2	81.33	219.18
			3	0.23	0.45
		40	4	0	0
			5	0	0
			6	0	0

Set No	Sample No	Current (mA)	Cycle No	Capacity (mAh/g)	Energy (Wh/Kg)
6	3	20	1	39.7	100.85
			2	40.9	109.22
			3	41.23	109.88
		40	4	24.09	63.68
			5	23.15	60.92
			6	22.71	59.64
	7	20	1	55.99	136.6
			2	62.4	167.92
			3	70.65	194.22
		40	4	43.59	117.45
			5	60.58	169.65
			6	62.52	176.93
	12	20	1	42.42	100.28
			2	56.35	148.43
			3	73.1	196.06
		40	4	59.57	163.66
			5	62.81	174.94
			6	64.3	180.99
	16	20	1	15.91	36.76
			2	19.82	49.53
			3	38.99	112.45
		40	4	55.76	164.46
			5	62.66	185.5
			6	19.07	50.23
	18	20	1	61.28	148.73
			2	65.71	177.02
			3	76.8	213.47
		40	4	72.53	208
			5	91.8	267.2
			6	101.15	292.3